ABSTRACT

PARKS, NICHOLAS BROOKS. Black Start Control of a Solid State Transformer for Emergency Distribution Power Restoration. (Under the direction of Subhashish Bhattacharya.)

In this thesis, the control of a solid state transformer is evaluated for the purpose of emergency power restoration of a microgrid. The solid state transformer consists of three stages capable of bidirectional power flow. The three stages consists of a local load three leg H-bridge inverter with a 120/240 V AC output, a dual active bridge (DAB) DC-DC converter built with two H-bridges separated by an isolation transformer and a grid connected H-bridge with an LCL output filter. A battery bank connected to a renewable energy resource can be connected to the DAB low voltage DC bus to reduce the power drawn from the grid, and become a power source during emergency power restoration.

With an increasing number of power electronics converters being integrated into the utility grid for different purposes such as FACTS based STATCOM for transmission systems to PV inverters connected to battery banks, a more intelligent and flexible grid is emerging. Failures in the utility grid, while rare, do occur and depending on the type of failure restoration times can take hours or even days. With distributed storage devices and power electronics devices such as the solid state transformer, an islanded grid commonly known as a microgrid can be formed and allow load to be reconnected thereby greatly reducing the outage time. When the grid has been restored, the microgrid can reconnect to the utility. Restoring power in this fashion by using locally available power generation sources is commonly known as a Black Start.

The system level operation of the solid state transformer is defined in this thesis. Additionally, analysis of each stage of the solid state transformer is done to evaluate the control needed during the Black Start procedure.

Black Start Control of a Solid State Transformer for Emergency Distribution Power Restoration

by
Nicholas Brooks Parks

A thesis submitted to the Graduate Faculty of
North Carolina State University
in partial fulfillment of the
requirements for the Degree of
Master of Science

Electrical Engineering

Raleigh, North Carolina

2012

APPROVED BY:

Mesut E. Baran	Srdjan Lukic

Subhashish Bhattacharya
Chair of Advisory Committee

DEDICATION

This work is dedicated to my family who have blessed me with their support and love.

BIOGRAPHY

Nicholas Parks was born in Raleigh, North Carolina, United States of America and attended grade school and high school in Chatham County, North Carolina. He received the Bachelor of Science degree in Electrical Engineering from North Carolina State University in 2009. Upon completion of his bachelors degree he joined the graduate school at NCSU working towards his Master of Science degree in Electrical Engineering with an emphasis on power systems and power electronics under the direction of Subhashish Bhattacharya with the NSF FREEDM Systems Center. While in graduate school he was a teaching assistant and research assistant, he also developed the undergraduate power electronics laboratory at NCSU during his graduate career.

ACKNOWLEDGEMENTS

I am grateful to all the people who have made it possible for me to complete this work and who have given me guidance and support. Specifically, it would not be possible for me to complete this work without the financial support provided by my advisor Dr. Subhashish Bhattacharya and my committee member Dr. Mesut Baran. I would like to thank all my committee members, Dr. Bhattacharya, Dr. Baran, and Dr. Lukic for their support and guidance. I am thankful for the work of my committee members at North Carolina State University and at the FREEDM Systems Center through which I have learned so much about power electronics and power systems engineering that I will take with me in life.

First I would like to acknowledge my friends Justin Smith and Jon McDonald we have all been through a lot together. Also I am thankful for all my friends in the FREEDM Systems Center who have helped to discuss with me not only about my work but also to take my mind off of it.

TABLE OF CONTENTS

LIST OF TABLES

LIST OF FIGURES

Chapter 1

Introduction

1.1 Background of Power Restoration

While the utility grid is designed to be reliable, standards developed by the North American Electric Reliability Corporation (NERC) are in place in the event of a system failure [3]. Typically the restoration procedure after an outage follows either a top-down or bottom-up scheme. In the top-down restoration procedure, tie lines outside of the failure area are energized which are used to energize the transmission lines through tie-breakers. Load can be picked up, and auxiliary power can be restored to generators allowing the distribution system to return. The bottom-up method of system restoration is used in the event that no outside tie line is available to energize the lines. In this situation individual generation units which have an on-site auxiliary power source or the ability to self-start can be used as nodes for restoration. This type of restoration is often termed as a black start and typical black start generating units include hydroelectric or diesel generators and gas turbines [4]. The Federal Energy Regulatory Commission (FERC) defines black start as "The ability to go from a shutdown condition to an operating condition delivering electric power without assistance from the electric system." [2]. The top-down restoration procedure is shown in Figure 1.1, the bottom-up restoration procedure is shown in Figure 1.2, and Figure 1.3 shows the nodes which have been restored during the bottom-up restoration procedure being reconnected together.

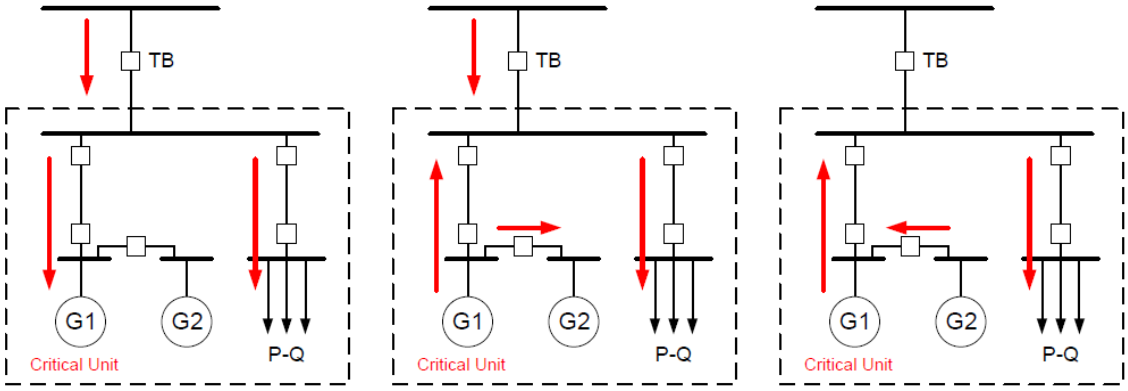

Figure 1.1: Top down restoration procedure

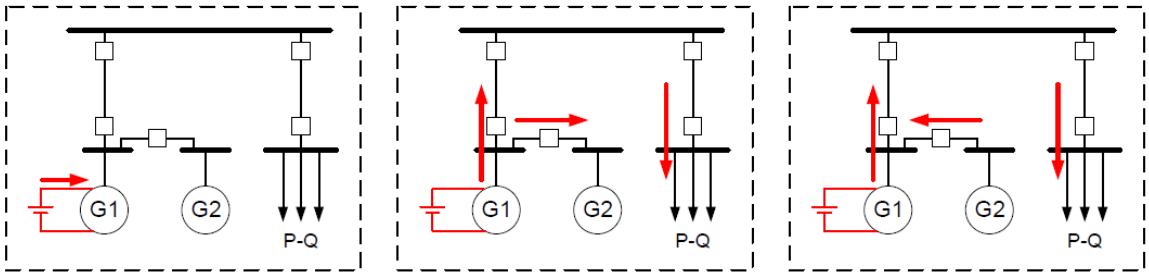

Figure 1.2: Bottom up restoration procedure

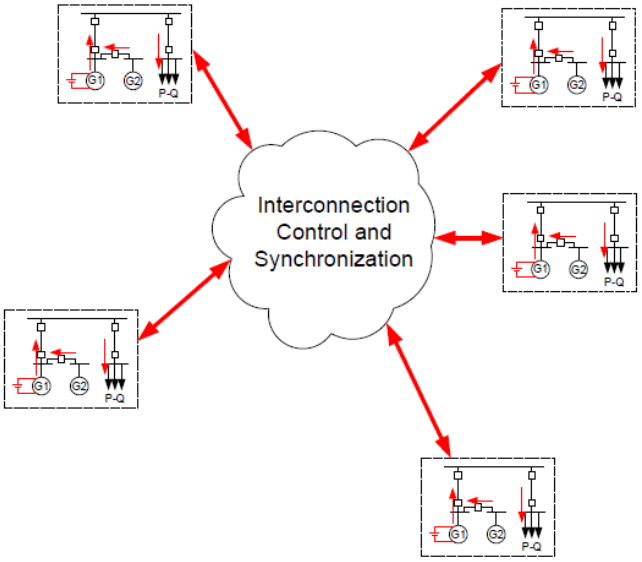

Figure 1.3: Bottom up restoration - reconnecting restored nodes

Although traditionally black start units are used to supply the auxiliary power necessary to start larger generation units, a similar idea can be used with renewable energy resources. Using renewable energy resources for power restoration can benefit not only the residential area, but also small businesses by reducing outage times. Commercial power consumers with large power consumption can also benefit when generation and storage systems have enough capacity.

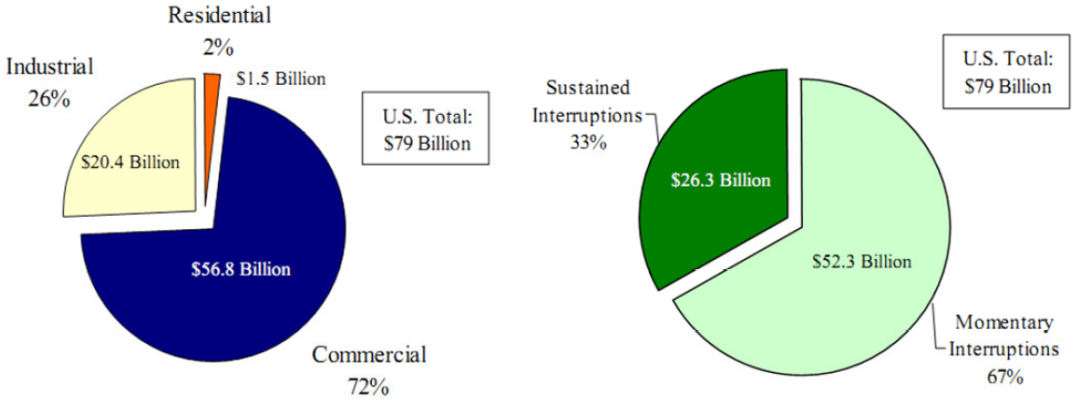

Figure 1.4: Annual cost of power interruptions in the U.S. - Customer classes (left) and type of interruption (right) (Momentary:<5 minutes, Sustained:>5 minutes) [1]

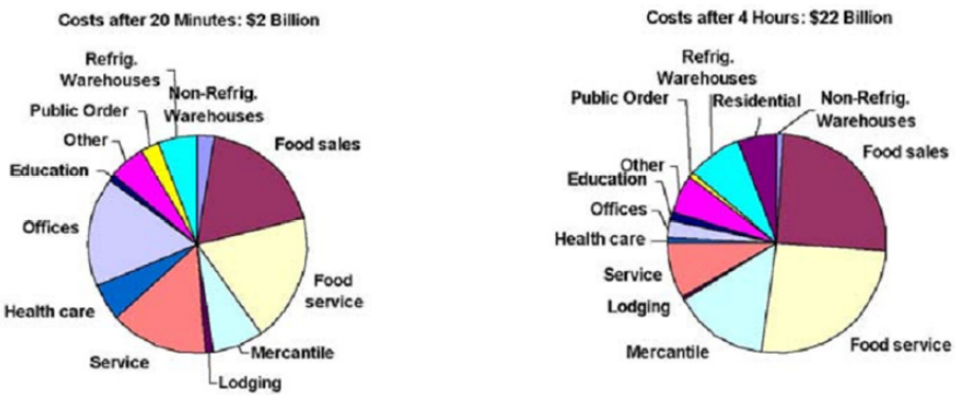

Figure 1.5: Power outage costs in the commercial sector after 20 minutes and 4 hours [2]

Figure 1.4 from a 2004 Berkeley National Laboratory study shows the annual cost of power outages in the U.S. based on the type of electricity customer class shown by the left hand pie chart while the cost based on the type of interruption is shown on the right hand pie chart. It is clear that the commercial sector accounts for the largest cost annually, as noted in [1] while the per outage per customer cost is much higher in the industrial sector than the commercial sector, the population of the industrial sector is much smaller than the commercial sector. The right hand pie chart shows that momentary interruptions account for the majority of the cost at around $54 billion annually. The momentary and sustained interruption costs are an area that can be reduced using a black start procedure with renewable energy sources with energy storage, they are specifically suited for the momentary interruptions with the assumption that the distributed energy sources have small storage capability and when paralleled can be used to ride through the momentary interruption to the electricity service and with enough storage longer interruptions can also be reduced. Figure 1.5 shows the total outage costs after 20 minutes and 4 hours respectively for different commercial areas.

1.2 Distributed Renewable Energy Resources

Renewable generation resources such as wind, solar, and geothermal are increasingly being connected to the grid through power electronic interfaces. Advances in power electronics and the development of fast switching semiconductors along with increased efficiency and decreased cost of producing renewable energy products has helped to increase interest in renewable energy. Other advantages of renewable energy resources is that it is possible to create many small generation sites. Distributed generation using renewable resources has some advantages when compared to the normal centrally generated power systems (coal or nuclear plants) including

increased reliability, reduced peak power requirements, and reduced vulnerability to natural disasters and terrorism [2].

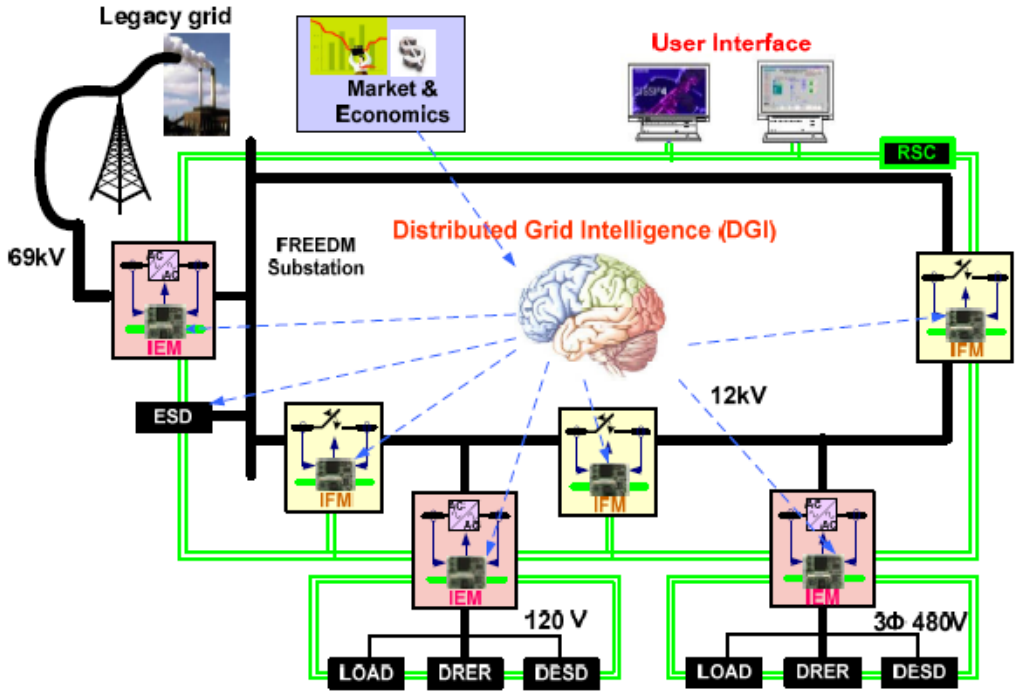

Figure 1.6: FREEDM Systems Center smart grid with distributed generation

An outline of the electric utility grid connected to the NCSU FREEDM Systems Center smart grid utilizing distributed renewable energy resources is shown in Figure 1.6. The FREEDM smart grid utilizes distributed intelligence along with distributed energy resources and distributed energy storage devices to operate in a more efficient and reliable way than the traditional electric utility grid.

1.3 Solid State Transformer

The traditional distribution transformer has performed its job of changing voltage levels for well over one hundred years allowing long distance power transmission to be practical and economical. Additionally distribution transformers are extremely efficient ranging from 97% to 99.5% on average depending on size and construction [5]. However, these distribution transformers are bulky, very heavy, cannot handle harmonics well and are very much a static element in the power system. A transformer built utilizing high power semiconductor technology could have

increased functionality, decreased size and weight, and act as a dynamic element in the power system through its control systems.

The concept of a solid state transformer is not new and has its origins around 1970 at GE where a high frequency link based AC/AC converter was designed [6][7]. This initial work was followed by the United States Navy in 1980 with an AC/AC buck converter and in 1995 by the Electric Power Research Institute (EPRI) with a similar solid state transformer concept [8][9].

With semiconductor technologies such as 6.5 kV Silicon IGBT, and 10 kV SiC MOSFET, high voltage solid state transformers are possible. Some important criteria for the solid state transformer is it should perform the traditional role of voltage conversion, include isolation between high voltage and low voltage, allow for bidirectional power flow, and include a DC bus where additional energy storage can be interfaced. Using lower voltage rated silicon semiconductor technology, a solid state transformer topology which can fulfill the previous criteria is shown in Figure 1.7. The solid state transformer is a multilevel cascaded converter design which is necessary when using low voltage IGBT to reduce the voltage stress across the switches.

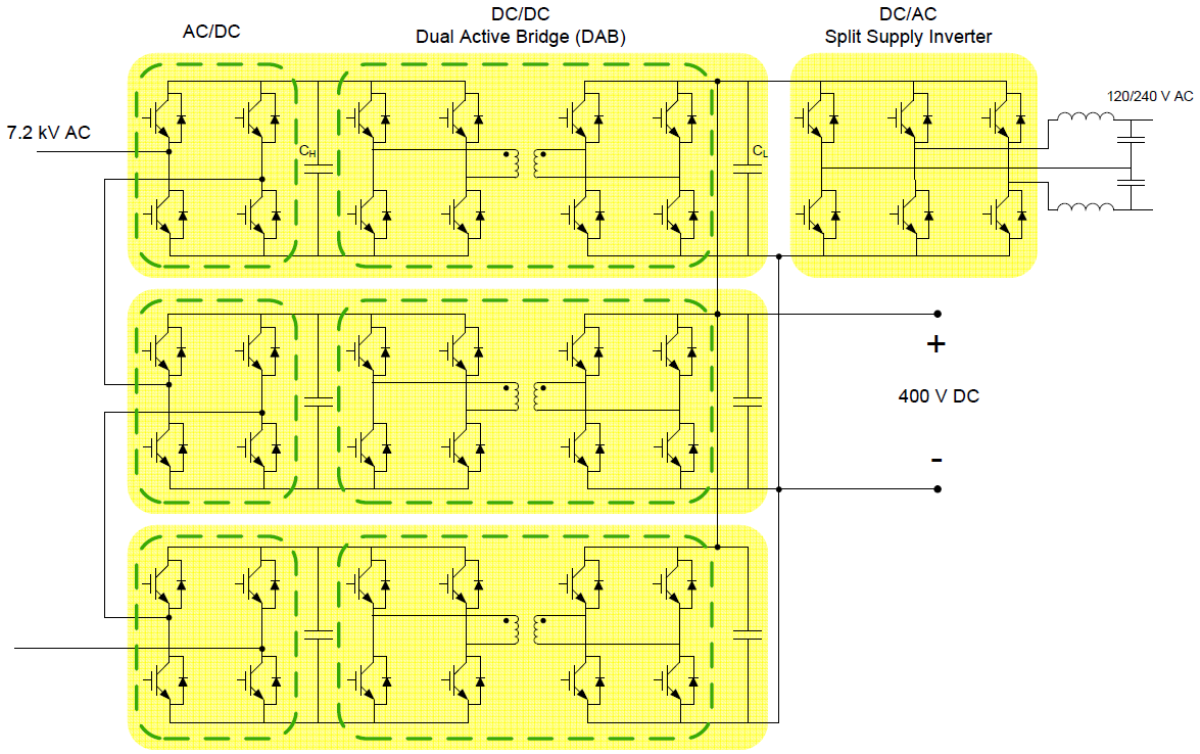

Figure 1.7: Multilevel Solid State Transformer

The solid state transformer nominal power is 20 kVA, input phase voltage of 7.2 kV. The single phase, multilevel solid state transformer has three stages - the first stage rectifies the grid voltage, the second stage is a DC/DC converter known as a dual active bridge that consists of two H-bridges isolated by a high frequency transformer and the last stage is a split supply inverter which supplies the local load with 120/240 V AC. In between each stage is a decoupling capacitor - a high voltage capacitor at 3.8 kV and a low voltage capacitor at 400 V. Detailed descriptions of different solid state transformer topologies for different semiconductor technologies can be found in [7].

The solid state transformer topology that is considered here is a two level converter shown in Figure 1.8. In Figure 1.8 we see the three different stages of the solid state transformer - AC/DC, DC/DC with an isolation transformer, and DC/AC, the terms rectifier or inverter will be avoided to describe any of the stages until later because the operation of the individual stages change depending on system conditions. The application for this thesis will focus on a solid state transformer interfacing a distribution grid phase voltage of 7.2 kV RMS to a 120/240 V load. A system level diagram is shown in Figure 1.9 with power flow shown by the dotted arrows.

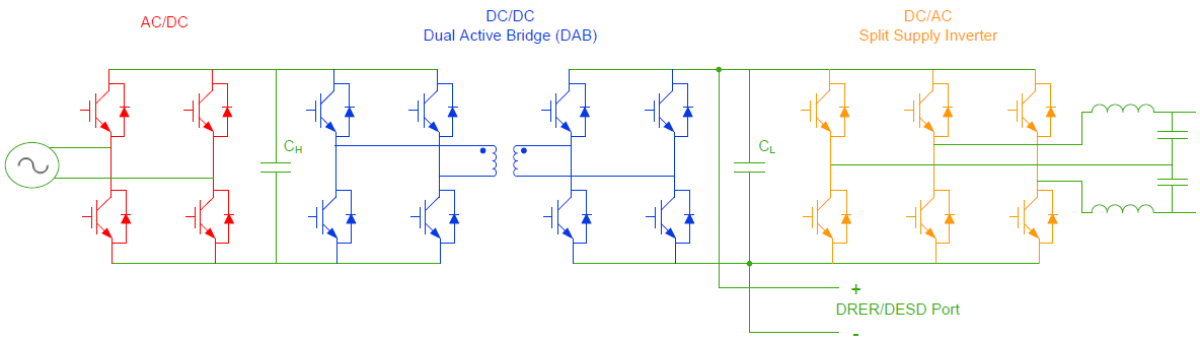

Figure 1.8: Two level solid state transformer

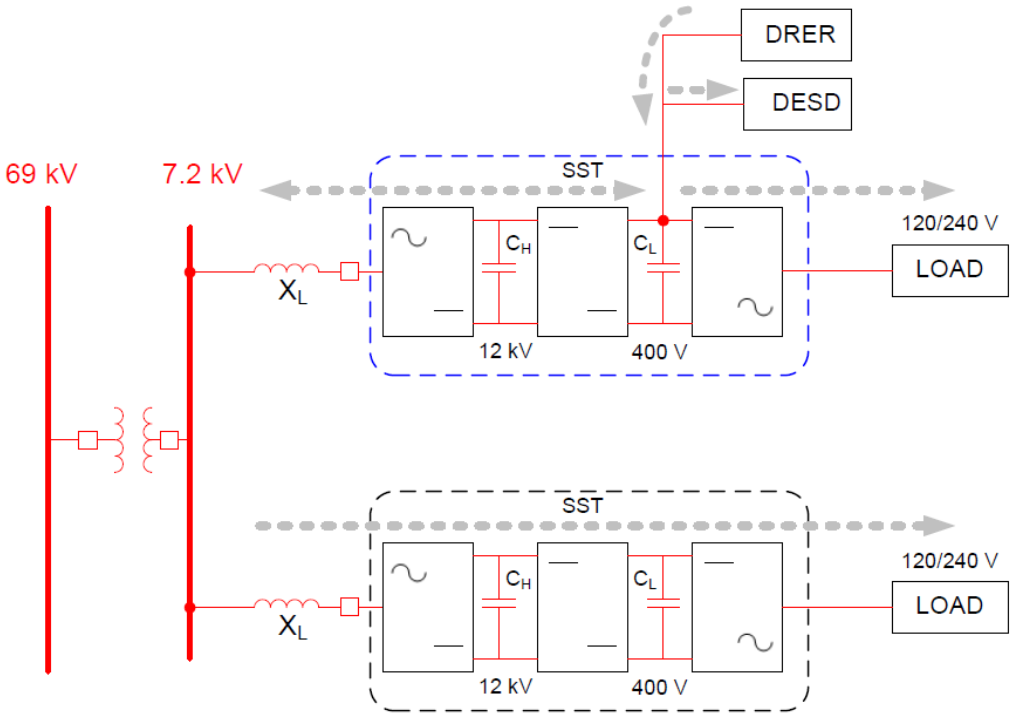

Figure 1.9: Solid state transformer system level showing power flow

In the system level diagram the subtransmission level voltage of 69 kV is stepped down to the distribution level of 7.2 kV at the point of common coupling (PCC) of two solid state transformers. The top solid state transformer has a distributed renewable energy resource (DRER) with a distribued energy storage device (DESD) connected at the low voltage side capacitor DC bus while the lower solid state transformer has only a load connected. The power flow is shown by the dotted arrows, for the solid state transformer with only a load, power will flow from the grid to load. For the solid state transformer with a DRER and DESD connection, power flow will depend on the state of charge of the DESD, generation by the DRER, and the load conditions.

It can now be clearly seen in Figure 1.9 that in the event of a power system failure resulting in the loss of the 69 kV grid voltage that a power source is still available from the renewable energy resource (such as a photovoltaic panel array or wind turbine) and storage device (such as a battery bank). During the grid loss, power can be restored to the loads by using the renewable energy resource which we will term as a black start of the microgrid while the solid state transformer with the renewable energy resource is called a black start resource.

1.4 Black Start of Solid State Transformer

With enough energy storage capability, the black start resource solid state transformer can re-establish the distribution grid and provide power to the loads. Figure 1.10 shows the operation of the solid state transformer under black start conditions. The operation of the black start solid state transformer changes depending on if it is operating as a black start resource or if it is grid connected. Looking at Figure 1.10, the local load stage will operate exactly the same as in grid connected mode which is as a split phase inverter with a 400 V dc input voltage source. Stage 2 will continue to operate as a DC/DC converter, however it will control the high voltage DC bus and stage 1 will act as an inverter in parallel with all other black start solid state transformer outputs.

It can be seen by comparing Figure 1.9 and Figure 1.10 that the solid state transformer without an energy source does not change operation between grid connected and islanded modes, therefore the stages are labelled as rectifier, DC/DC, and inverter. However, it should be noted that during islanded mode the voltage levels change, therefore control algorithms can be reused but control gains may need to be adjusted. In Figure 1.10 there is only one black start resource, the top solid state transformer, however other black start resource solid state transformers with DRER/DESD could be connected to create a stiffer grid and have a greater load capacity.

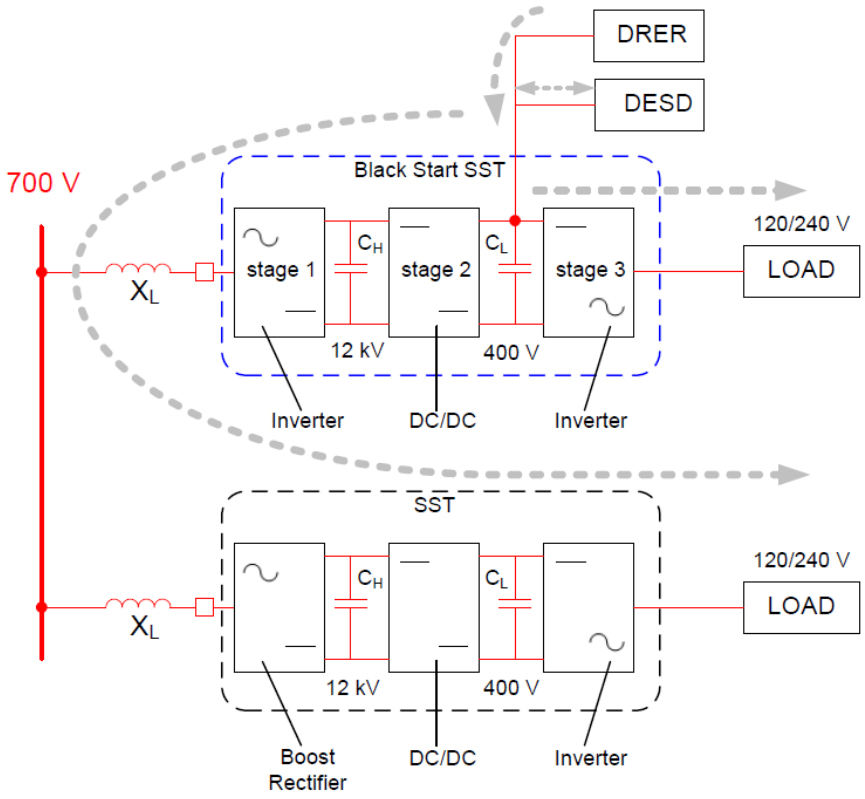

Figure 1.10: Black start with solid state transformer

The black start procedure begins when the utility grid connection and the distribution voltage is lost. When the grid connection is lost the solid state transformer must isolate itself from the grid and disconnect its load. From this point the black start solid state transformer will start to restore the local distribution network forming a microgrid. The procedure that the black start solid state transformer will follow is listed as follows.

1. Low voltage DC bus is restored to nominal voltage by DRER/DESD.
2. Local load (120/240 V) power is restored by stage 3 operating as an inverter.
3. High voltage DC bus is restored to nominal voltage by stage 2 DC/DC converter.
4. Stage 1 inverter output filter capacitor is charged to nominal microgrid voltage.
5. Black start solid state transformers are reconnected in parallel.
6. Non-black start solid state transformers restore load.

In Figure 1.10 the restoration voltage is 700 V, this voltage level is based on the fact that the solid state transformers should reconnect in small nodes similar to Figure 1.3 essentially forming microgrids which could individually reconnect to the utility grid once it is restored. Ideally, the solid state transformer will connect to only a few of its neighboring solid state transformers, therefore supplying its own load along with its neighbors is possible with a small battery and distributed renewable energy source such as a PV array. Depending on the amount of solid state transformers that are connected and the amount of load, the microgrid voltage may need to be increased to reduce copper losses.

It is obvious that if the capacity of the DRER/DESD is not capable of supplying all the loads being restored than some type of load shedding will have to take place. For this work it is assumed that the storage capacity of the battery is enough to supply the restored load along with its own local load.

While intentional islanding standards are being considered by the IEEE, grid connected distributed resources are considered in the IEEE 1547 standard - Standard for Interconnecting Distributed Resources with Electric Power Systems [10]. The standard defines how distributed resources such as fuel cells, wind turbines, photovoltaic panels, and microturbines should be connected to any power system and the amount of disturbance they are allowed to introduce. These standards would need to be considered when the grid is restored and when the solid state transformers are reconnecting in grid connected mode. The limits in place for frequency, voltage, and phase deviations during interconnection of the solid state transformer to a power system is shown in table 1.1.

Table 1.1: IEEE 1547 Standards

DER Synchronization Limits			
Power Rating	Δf Hz	ΔV Volts	$\Delta\phi$ degrees
0-500 kVA	0.3	10	20
500-1500 kVA	0.2	5	15
1500-10000 kVA	0.1	3	10

To summarize the operation of the solid state transformer, the switch level diagram is shown in Figure 1.11.

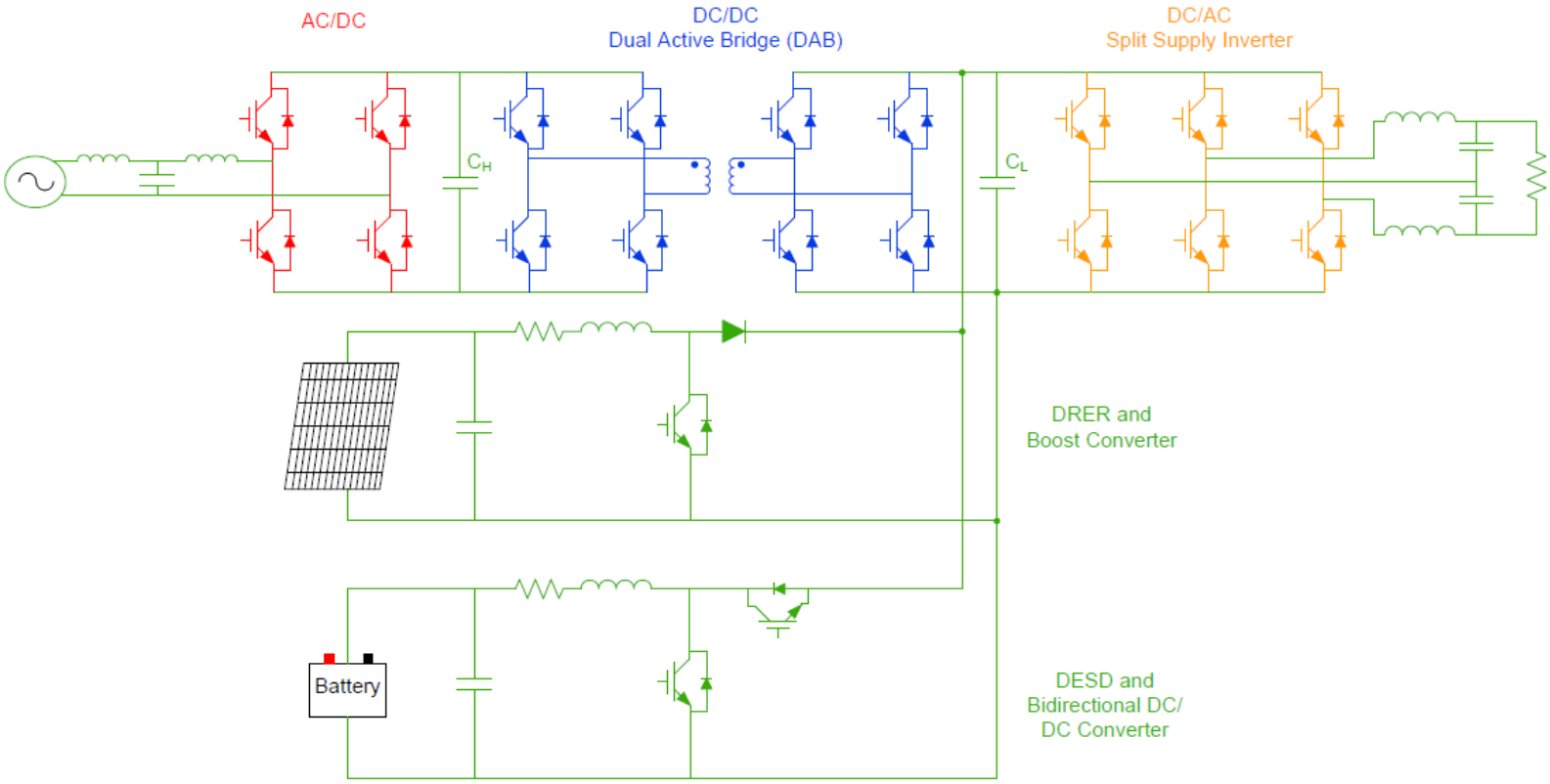

Figure 1.11: Solid state transformer with DRER (battery) and DESD (PV panel)

1.5 Goals and Outline

The goal of this work is to develop a model for the solid state transformer including control design for the different stages for normal and black start operation. The focus will be on the black start operation and the control that is necessary for each stage to properly restore the local microgrid and restore load power. It is shown in this work that the solid state transformer is a viable option for integrating renewable energy resources and using these resources for power restoration.

In chapter 1 the background for the thesis has been given including the black start concept. Chapter 2 discusses the modeling of each subsystem including the three stages of the solid state transformer, the PV boost converter, and the battery bidirectional converter. Chapter 3 introduces the control design for each subsystem and simulation results. Chapter 4 verifies the system level simulation and parallel operation of the black start solid state transformers supplying load. Chapter 5 discusses the conclusion and future work.

Chapter 2

Converter Modeling and Design

2.1 Switch Modeling Concepts

The process of developing a model of a switching power converter usually consists of finding a set of differential equations through Kirchoff's voltage law (KVL) and Kirchoff's current law (KCL) which describe the converter operation. To simplify the analysis of the models, the semiconductor switches such as IGBT - insulated gate bipolar transistor, and power MOSFET - metal oxide semiconductor field effect transistor can be modeled as ideal single-pole single-throw switches (SPST). Figure 2.1 shows how the two switch leg can be simplified for analysis.

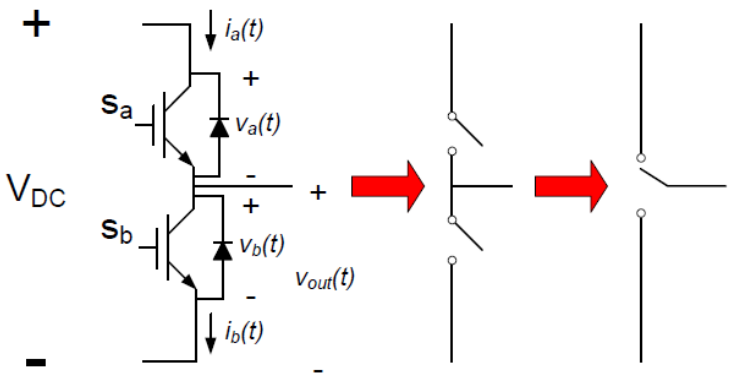

Figure 2.1: Simplified switch leg model

First the switching leg can be transformed into two SPST switches as previously discussed. Considering that both switches cannot be on at the same time which would short circuit the source, we can find the following switching functions:

$$S_n = \begin{cases} 1, & \text{Switch n closed, } v_n(t) = 0 \\ 0, & \text{Switch n open, } i_n(t) = 0 \end{cases} \tag{2.1}$$

$$v_{out}(t) = \begin{cases} V_{dc}, & S_a = 1,\ S_b = 0 \\ 0, & S_a = 0,\ S_b = 1 \end{cases} \tag{2.2}$$

$$S_a + S_b = 1 \quad \therefore \quad S_a = \overline{S_b} \tag{2.3}$$

Finally, we can model the two switch leg as a single pole double throw (SPDT) switch as shown in the final simplification.

2.2 Pulse Width Modulation

Determining the turn on and turn off time of the converter switches is often done with a pulse width modulation scheme. In the pulse width modulation schemes a high frequency carrier signal is compared with a modulating signal which determines the turn on and off times of the switches, this allows the converter to realize an average low frequency desired output waveform. The main goal is to obtain the desired output waveform, the secondary goal is to minimize switching losses and harmonics generated by the modulation process. For inverter applications often the goal is to create a 60 Hz sinusoidal waveform at the output, this is required for the solid state transformer black start inverter and local load inverter. The harmonic spectrum of the inverter output voltage waveform will depend on the type of modulation used and the carrier waveform shape. The converter pulse width modulation switching frequency will depend on the carrier signal while the modulating signal determines the output voltage and fundamental frequency.

The most common modulation schemes are bipolar and unipolar [11]. The bipolar modulation scheme switches between $+V_{dc}$ and $-V_{dc}$, with $+V_{dc}$ at the output when the modulating signal is greater than the carrier signal and $-V_{dc}$ when the modulating signal is smaller than the carrier signal. Bipolar modulation is shown in Figure 2.2.

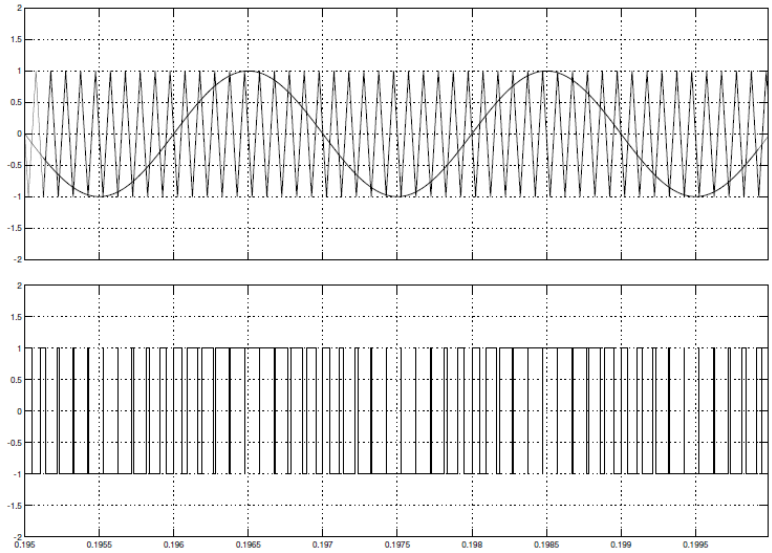

Figure 2.2: Bipolar PWM

In unipolar modulation the converter phase leg switches between an output of $+V_{dc}$ and 0 by using two different modulating signals, one for each leg of the inverter, which are the same magnitude but with 180° phase difference. The line to line output voltage then varies between $+V_{dc}$ to 0 and $-V_{dc}$ to 0. The unipolar modulation scheme will produce a better output waveform with less ripple than the bipolar modulation scheme. Unipolar modulation is shown in Figure 2.3.

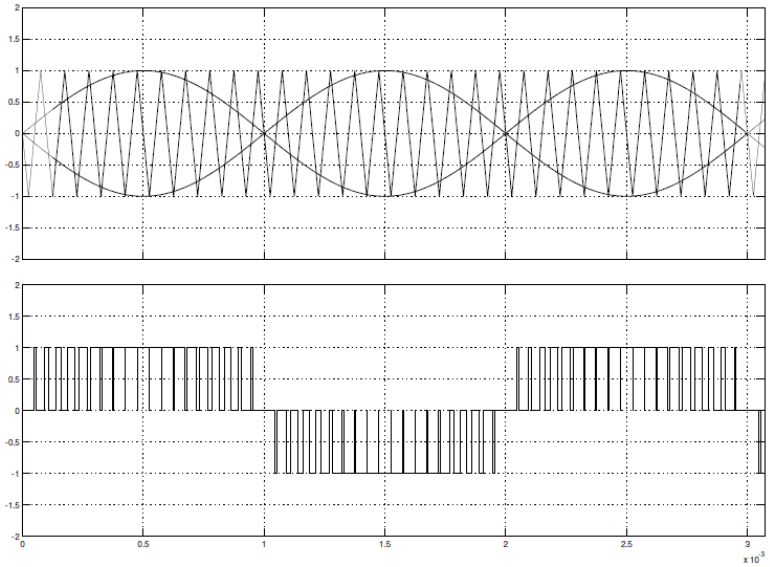

Figure 2.3: Unipolar PWM

Because of its superior harmonic performance, the unipolar modulation scheme is chosen. The harmonic levels injected by distributed resources such as those connected to the solid state transformer are regulated by IEEE 1547 in terms of TDD (Total Demand Distortion) percent, therefore using a unipolar modulation scheme is an easy way to reduce the harmonic levels.

The choice of carrier waveform can be either a triangle (double edge) waveform or a sawtooth (single edge) waveform. The carrier waveform used is a triangular carrier, the carrier waveform has a large effect on the harmonic distribution of the output waveform and must be chosen carefully depending on the application. Single edge carriers do not cancel the odd sideband harmonics around odd multiples of the carrier frequency in the output waveform. However, the double edge carrier waveform sideband harmonics around odd multiples of the carrier frequency are canceled, therefore the obvious choice is to use the triangle carrier [12].

2.3 Local Load Inverter Modeling

The local load inverter supplies the load that is directly connected to the solid state transformer with 120 V ac or 240 V ac output. Whether in grid connected or islanded mode, the local load inverter is controlled exactly the same. The source voltage for the local load inverter labeled Vdc in Figure 2.4 is regulated by different converters between grid connected and islanded modes. V_{dc} is controlled by the dual active bridge DC/DC converter in grid connected mode, while in islanded mode V_{dc} is controlled by the battery bidirectional DC/DC converter.

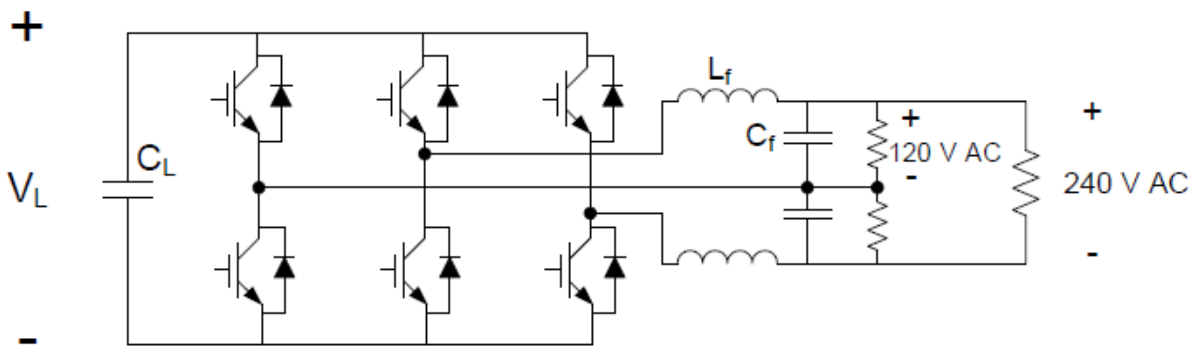

Figure 2.4: Local load inverter

To develop a model of the local load inverter, the phase leg averaging technique is applied. Phase leg averaging has been described in [13] and [14]. Figure 2.5 shows one phase leg of the local load inverter, the switches can be replaced with a SPDT switch as previously seen.

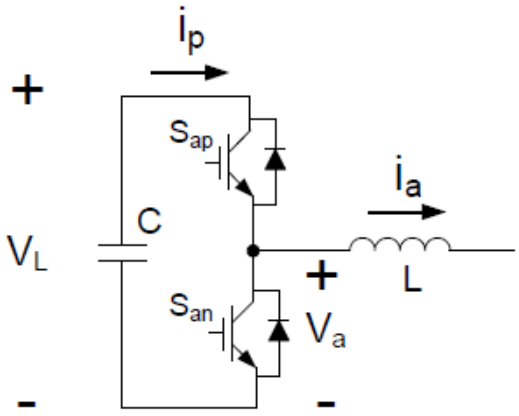

Figure 2.5: Inverter phase leg

The phase leg should follow some basic rules for its switching procedure, firstly the source voltage V_{dc} should not be short circuited, secondly the current flow through the inductor i_a should never be open circuited, therefore the phase leg should follow the switching functions in eqs. (2.1) and (2.3). From the switching functions the terminal quantities can now be defined.

$$v_a(t) = S_{ap} V_L \tag{2.4}$$

$$i_a(t) = S_{ap} i_p \tag{2.5}$$

Figure 2.6 shows the ideal switching logic for the phase leg, we can apply the moving average operator given in equation 2.6 to obtain average values. In order to apply the moving average operator the carrier signal frequency must be much larger than the modulating signal frequency in this way the average value of voltage or current will be approximately constant over one switching period [15].

$$\overline{x}(t) = \frac{1}{T_s} \int_{t-T_s}^{t} x(\tau) d\tau \tag{2.6}$$

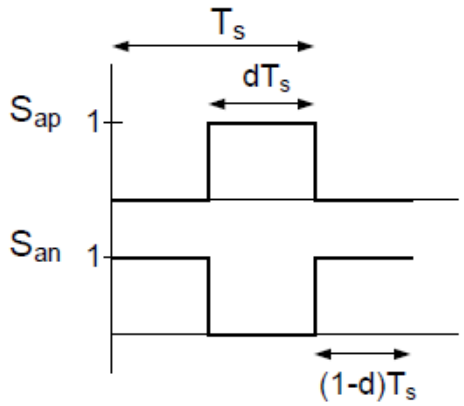

Figure 2.6: Phase leg switching

Upon applying the moving average operation we can easily find the average value to be proportional to the duty cycle as given in eqs. (2.7) to (2.9) where the bar indicates an average value.

$$\overline{S}_{ap} = d \tag{2.7}$$

$$\overline{v}_a = dV_L \tag{2.8}$$

$$\overline{i}_a = di_p \tag{2.9}$$

From the relations given in eqs. (2.8) and (2.9), the phase leg shown in Figure 2.5 can be redrawn to represent the average operation of the terminal quantities. The phase leg average model is shown in Figure 2.7. It should be noted that all values given in the model are averaged quantities although the bar notation as previously used is now dropped.

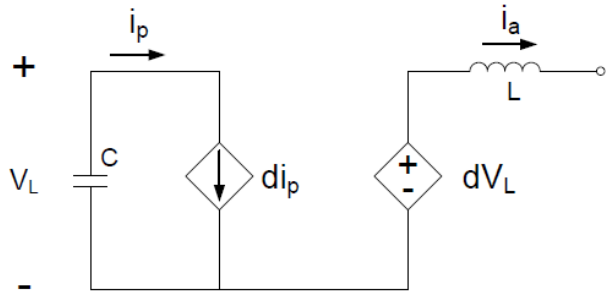

Figure 2.7: Averaged phase leg

Substituting the averaged phase leg model for the phase legs in the local load inverter, the average model is obtained in Figure 2.8.

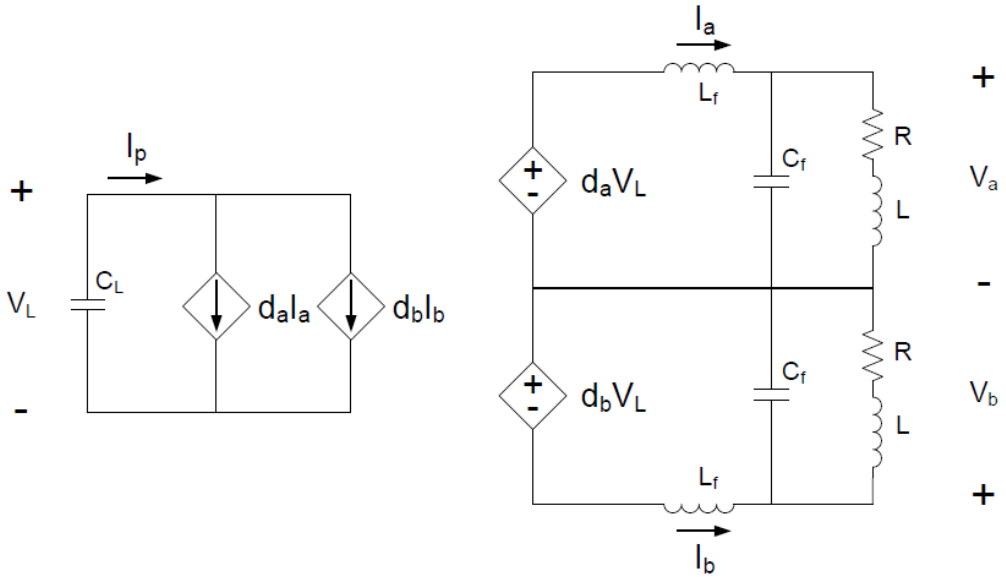

Figure 2.8: Averaged local load inverter model

Because of the symmetry of the system, we will only consider the top half of the averaged model, the designed controller can be the same for the other phase leg. From KVL and KCL, the following differential equations can be written from the averaged model. To obtain a state-space model the equations are written for the energy storage elements in the system which represent the system state variables.

$$L_f \frac{dI_a}{dt} = d_a V_L - V_a \tag{2.10}$$

$$C_f \frac{dV_a}{dt} = I_a - I_{La} \tag{2.11}$$

$$L \frac{dI_{La}}{dt} = V_a - I_{La} R \tag{2.12}$$

The steady-state DC values can be solved for by setting the differentials equal to zero.

$$V_a = d_a V_L \tag{2.13}$$

$$I_a = I_{La} \tag{2.14}$$

$$I_{La} = \frac{V_a}{R} \tag{2.15}$$

A small perturbation is added to the system in order to obtain the small-signal model, high order terms are discarded while first order terms are kept in the small-signal model which are represented with a hat.

Letting the line input disturbance go to zero ($\hat{V}_{dc} = 0$), the following small-signal ac equations can be found.

$$\frac{d\hat{i}_a}{dt} = -\frac{1}{L_f}\hat{V}_a + \frac{V_L}{L_f}\hat{d}_a \tag{2.16}$$

$$\frac{d\hat{V}_a}{dt} = \frac{1}{C_f}\hat{i}_a - \frac{1}{C_f}\hat{i}_{La} \tag{2.17}$$

$$\frac{d\hat{i}_{La}}{dt} = \frac{1}{L}\hat{V}_a - \frac{R}{L}\hat{i}_{La} \tag{2.18}$$

The differential equations eqs. (2.16) to (2.18) can be rewritten in state-space form given as follows where the superscript dot notation indicates a derivative with respect to time $\frac{d}{dt}$.

$$\begin{bmatrix} \dot{\hat{i}}_a \\ \dot{\hat{i}}_{La} \\ \dot{\hat{V}}_a \end{bmatrix} = \begin{bmatrix} 0 & 0 & -\frac{1}{L_f} \\ 0 & -\frac{R}{L} & \frac{1}{L} \\ \frac{1}{C_f} & -\frac{1}{C_f} & 0 \end{bmatrix} \begin{bmatrix} \hat{i}_a \\ \hat{i}_{La} \\ \hat{V}_a \end{bmatrix} + \begin{bmatrix} \frac{V_L}{L_f} \\ 0 \\ 0 \end{bmatrix} d_a \tag{2.19}$$

Using the small signal state space model in equation 2.19, the following transfer functions can be easily derived.

$$\frac{\hat{i}_a}{\hat{d}_a} = V_L \frac{s^2 C_f L + s C_f R + 1}{s^3 L_f C_f L + s^2 L_f C_f R + s(L_f + L) + R} \tag{2.20}$$

$$\frac{\hat{i}_{La}}{\hat{d}_a} = V_L \frac{1}{s^3 L_f C_f L + s^2 L_f C_f R + s(L_f + L) + R} \tag{2.21}$$

$$\frac{\hat{V}_{aN}}{\hat{d}_a} = V_L \frac{sL + R}{s^3 L_f C_f L + s^2 L_f C_f R + s(L_f + L) + R} \tag{2.22}$$

$$\frac{\hat{i}_c}{\hat{d}_a} = V_L \frac{s^2 L C_f + s C_f R}{s^3 L_f C_f L + s^2 L_f C_f R + s(L_f + L) + R} \tag{2.23}$$

In order to verify the transfer functions, the average model is built in Matlab Simulink using the PLECS toolbox and the Simulink Linear Analysis function is used to obtain the transfer function. The transfer function is obtained and compared with the $\frac{\hat{i}_c}{\hat{d}_a}$ transfer function above. The values used in the comparison are given below.

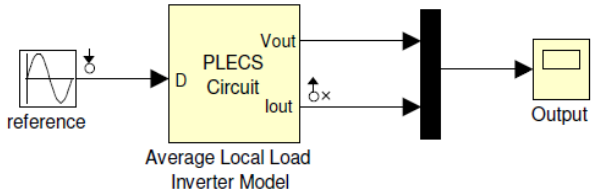

Figure 2.9: Averaged local load inverter

Table 2.1: Local load inverter parameters

Local Load Inverter Parameters		
Parameter	Value	Unit
V_L	400	V
f_s	10	kHz
L_f	1	mH
C_f	120	μF
L	0	H
R	1.44	Ω

Using the parameters in 2.1 equation 2.23 can be written as:

$$\frac{\hat{i}_c}{\hat{d}_a} = \frac{400000s}{s^2 + 5787.04s + 8.33333e6} \tag{2.24}$$

The calculated transfer function is plotted in Figure 2.10, while the bode plot obtained using the Simulink Linear Analysis is plotted in Figure 2.11. From the plots it can be seen that the bode plots are the same and the calculated transfer function is accurate and can be used for control design.

2.3.1 Local load inverter transfer function verified

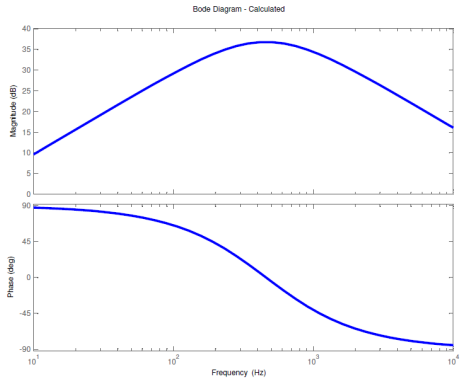

Figure 2.10: Calculated transfer function

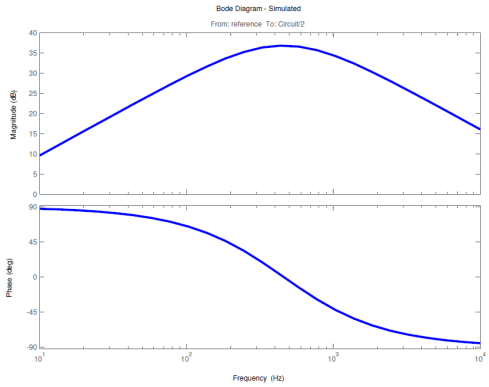

Figure 2.11: Simulated transfer function

2.4 Dual Active Bridge

The dual active bridge (DAB) consists of two H-bridges, one high voltage and one low voltage. The DAB is an important subsystem of the solid state transformer, it provides galvanic isolation between the high voltage and low voltage sides of the solid state transformer provided by the high frequency transformer between the two H-bridges. The DAB has a DC source voltage which is inverted to an AC voltage by one of the H-bridges, the second H-bridge rectifies the AC voltage to give the DC output voltage. When in grid connected mode the DAB regulates the low voltage DC bus V_L while the high voltage DC bus V_H is regulated by the AC/DC converter (stage 1 in Figure 1.10). If the solid state transformer is islanded, the low voltage DC bus V_L is regulated by the battery bidirectional DC/DC converter shown in Figure 1.11, while the high voltage DC bus V_H is regulated by the DAB.

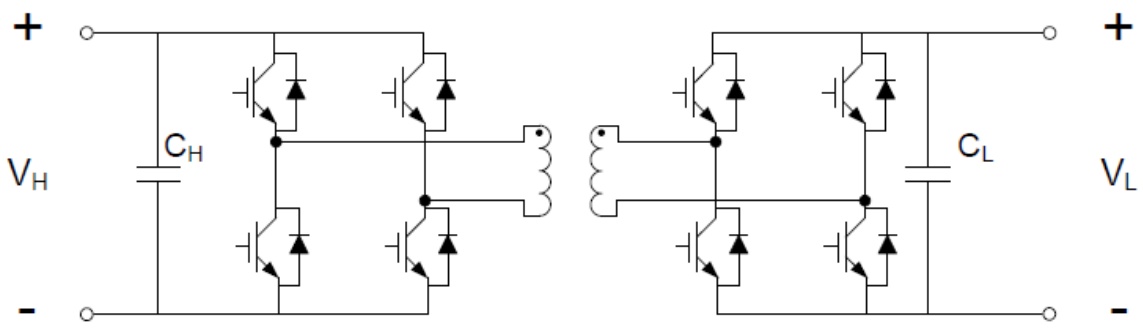

Figure 2.12: Dual Active Bridge (DAB)

The dual active bridge (DAB) topology has been extensively studied in [16] and [17]. The real power in the DAB will flow from the bridge with leading phase angle to the bridge with lagging phase angle as in the classical circuit of two ac sources connected by an inductive impedance. The power transfer of the DAB is given by equation 2.25 while the average current is given in 2.26 [18].

$$P = \frac{nV_L V_H}{2fL} d_h(1 - d_h) \tag{2.25}$$

$$I_{avg} = \frac{nV_{dc}T_s}{2L} d_h(1 - d_h) \tag{2.26}$$

In equation 2.25, n is the turns ratio of the high frequency transformer, V_L is the low voltage DC bus, V_H is the high voltage DC bus, f is the switching frequency, L is the transformer leakage inductor, d_h is the ratio of time delay between the bridges and half the switching period. In equation 2.26 V_{dc} is the input voltage, T_s is the switching period.

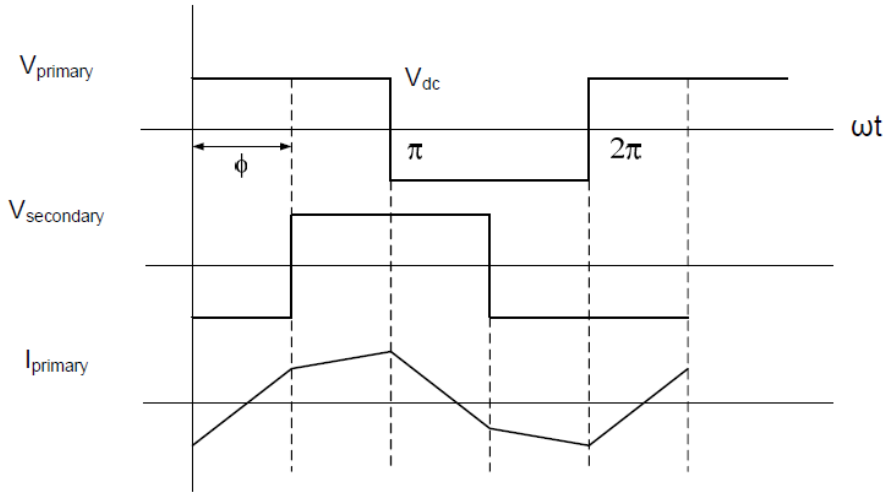

Figure 2.13: DAB Waveforms

From equation 2.25, it is clear that the transformer leakage inductance is the limiting factor for the power output of the DAB, if the leakage inductance is made small than the power output of the DAB can be increased. The transformer turns ratio is $\frac{n_1}{n_2} = \frac{400}{3800}$, the leakage inductance can be determined as follows.

$$P_o = 20\ kW = \frac{(\frac{400}{3800})(400\ V)(3800\ V)}{2(3000\ Hz)(L)} 0.25(1 - 0.25)$$

$$L = 0.00025\ H$$

The leakage inductance is calculated as 250 μH operating at a delay of $\frac{\pi}{8}$ ($d = \frac{\frac{\pi}{8}}{\frac{\pi}{2}} = 0.25$) for the rated operating power of 20 kW, this gives the DAB the ability to increase the delay to $\frac{\pi}{2}$ to increase output power during transient conditions.

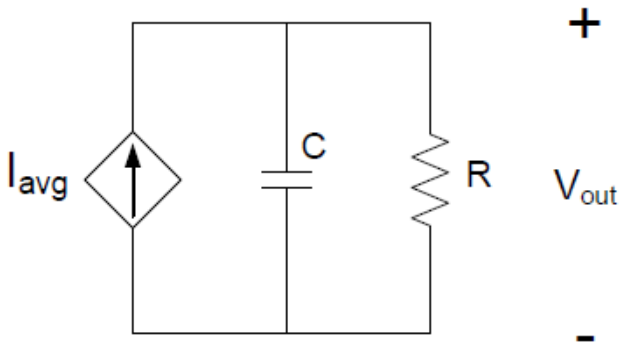

Figure 2.14: DAB average model

The small signal control to output transfer function is given in equation 2.27. The output voltage of the DAB can be controlled by controlling the phase shift, or delay between the input and output bridges.

$$\frac{\hat{v}_{out}(s)}{\hat{d}_h(s)} = \frac{V_{dc}T_s}{2L}(1-2D)Z_{out}(s) \tag{2.27}$$

$$\text{where } Z_{out}(s) = \frac{1}{sC}||R$$

To verify the DAB equations, the average model and switching model are compared through simulation. The average model shown in Figure 2.14 and the switching model shown in Figure 2.12 are simulated in Matlab Simulink with the PLECS toolbox, the simulation is shown in Figure 2.15.

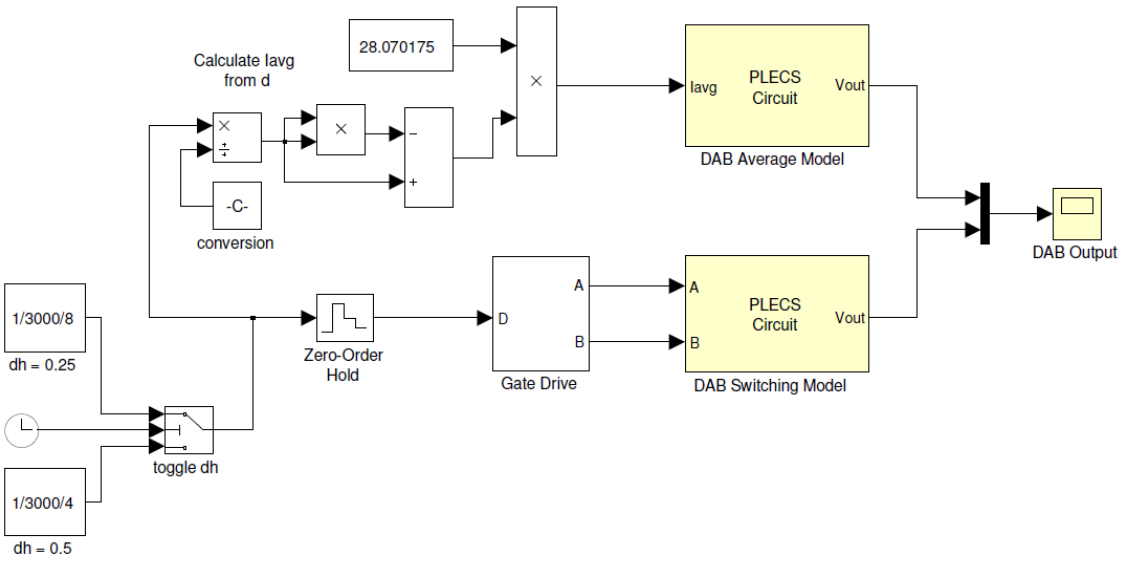

Figure 2.15: DAB simulation - average and switching models

In the simulation the delay d_h is initially set at $\frac{\pi}{2}$ ($d_h = 0.5$), and at 0.3 seconds d_h is switched to $\frac{\pi}{4}$ ($d_h = 0.25$). The parameters for the simulation are given in Table 2.2.

Table 2.2: DAB Parameters

DAB Parameters		
Parameter	Value	Unit
V_L	400	V
f_s	3	kHz
$\frac{n_1}{n_2}$	$\frac{400}{3800}$	-
C_H	50	μF
C_L	2	mF
L (leakage)	250	μH
$R(load)$	722	Ω

According to equation 2.26, the average current for $d_h = 0.5$ should be 7.017 A, while the average current for $d_h = 0.25$ should be 5.263 A. Correspondingly, the average output voltage should be 5066.67 V for $d_h = 0.5$ and 3800 V for $d_h = 0.25$, the case of $d_h = 0.25$ is the nominal operating condition where the DAB controls the high voltage bus at 3800 V.

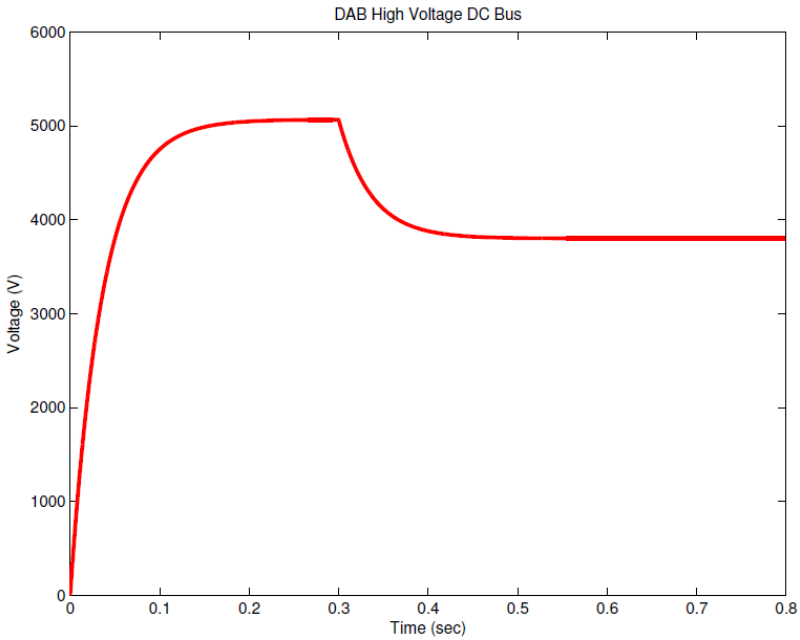

Figure 2.16: DAB simulation C_H voltage - average (green line) and switch model (red line)

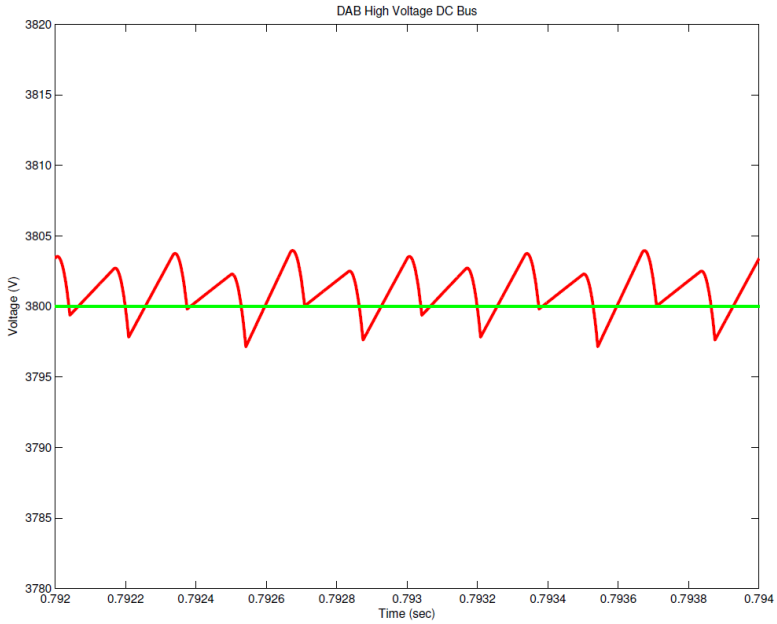

Figure 2.17: Detailed view of Figure 2.16 from 0.792 to 0.794 seconds

The simulation results are shown in figs. 2.16 and 2.17, from the figures the voltage increases to approximately 5066 V and decreases to 3800 V as the delay is decreased at 0.3 seconds. A close up view is shown in Figure 2.17 and it is seen that the average model correctly tracks the switching waveform.

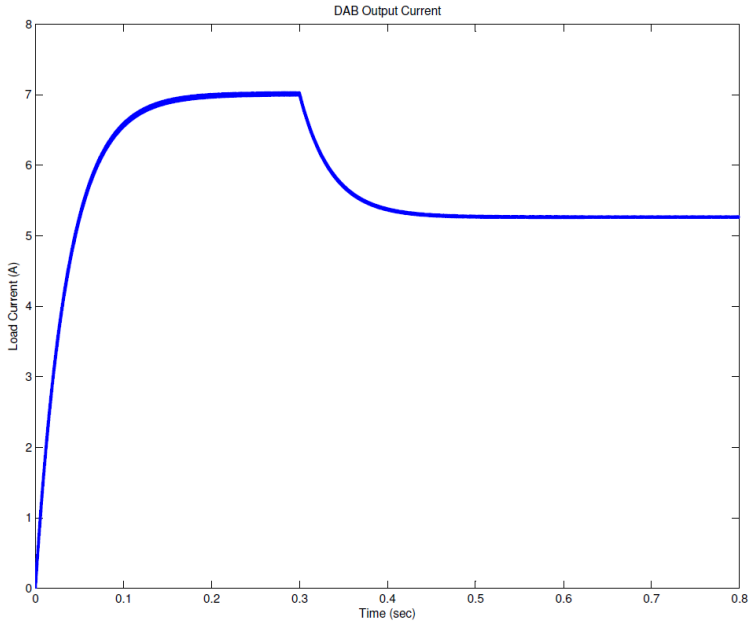

Figure 2.18: DAB load current for switching model

The DAB load current during the test is shown in Figure 2.18, the load current reaches steady state values as previously determined. It should be noted that the DAB model should be constrained to the region of phase shift between $-\frac{\pi}{2} \leq \phi \leq \frac{\pi}{2}$ to be valid [16], this is shown in Figure 2.19.

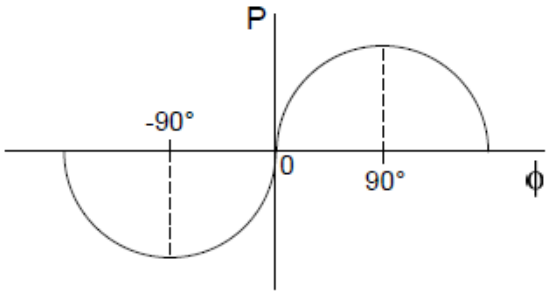

Figure 2.19: Operating constraints for the DAB average model

2.5 Grid Tied Rectifier / Black Start Inverter

During grid connection mode, stage 1 in Figure 1.10 acts as a grid-tied rectifier, if the grid connection is lost, stage 1 will be controlled as an inverter during the black start procedure. The different operating modes are treated individually starting with the grid-tied rectifier mode. The filter is also analysed to determine the best configuration for the converter.

2.5.1 Output Filter Design

Filter design is an important consideration for any power electronics system, the filter design is determined based on cost/weight, power transfer, and switching ripple/harmonic attenuation. Three common filters include the L, LC, and LCL types. The different filters that have been considered are now described.

The L type filter is shown in Figure 2.20, where V_t represents the terminal voltage of the inverter and PCC is the Point of Common Coupling with the grid. The grid line impedance is represented by an inductor in series with a resistor. The inductor can provide $-20\frac{db}{dec}$ of attenuation beyond the crossover frequency, in order to have acceptable harmonic attenuation the converter switching frequency must be increased which will increase switching losses. In [7], the filter inductor is calculated to be 0.4 H, which is considerably large. Ignoring the grid side impedance, the L filter transfer function can be written as follows.

$$\frac{i_g}{V_t} = \frac{1}{Ls + r_L} \tag{2.28}$$

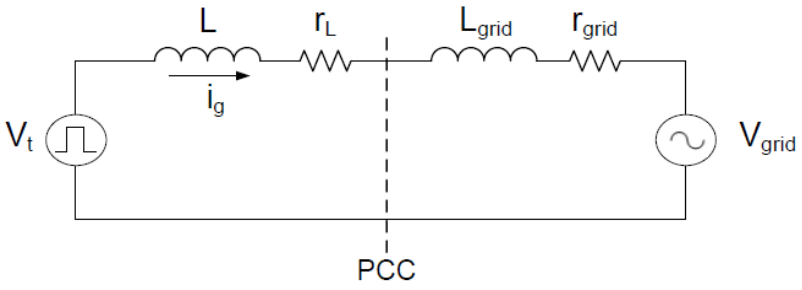

Figure 2.20: L type filter

The L filter has both advantages and disadvantages especially for our application. The L filter is inherently simple and has no problems with resonance, however it is bulky and creates a large voltage drop across it. We will later see in the control design that having a large inductive interface to the grid could be useful.

The LC type filter is shown in Figure 2.21, it can provide $-40\frac{db}{dec}$ of attenuation, however it is not effective when connected to a stiff grid because the stiff grid provides a low impedance harmonic path effectively shorting the shunt C element [19]. Additionally, it can be seen that the LC filter will have a resonance that is dependant on the line impedance parameters which will could cause stability problems. The LC filter is better suited towards a standalone application such as seen on the solid state transformer local load inverter where the output has a substantial impedance.

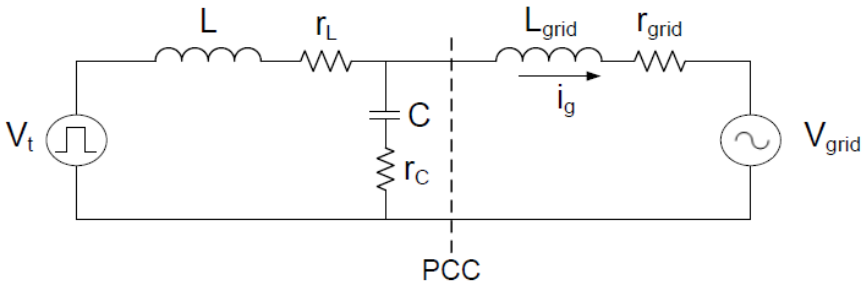

Figure 2.21: LC type filter

The LCL type filter is shown in Figure 2.22, it can provide $-60\frac{db}{dec}$ of attenuation, allowing the converter to operate at much lower switching frequencies as compared to the L type filter for equivalent harmonic attenuation. The grid side inductor helps to decouple the filter from

the grid line impedance parameters and makes the filter effective. For our application the LCL filter is adopted because of its greater attenuation and decreased size.

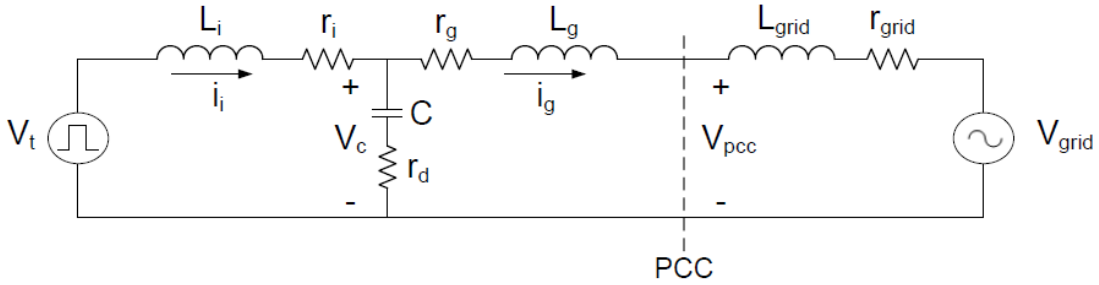

Figure 2.22: LCL type filter

Problems associated with the LCL filter include resonance and oscillations which can cause current distortion and stability issues without damping [19]. The resonant frequency of the LCL filter is given by equation 2.29 [20].

$$\omega_{res} = \sqrt{\frac{L_i + L_g}{L_i L_g C}} \tag{2.29}$$

The transfer functions for the LCL filter can be determined as follows by considering the PCC voltage to be a short circuit for harmonic frequencies [21].

$$i_g = i_i - i_c \tag{2.30}$$

$$V_t - V_c = i_i(sL_i + r_i) \tag{2.31}$$

$$V_c - V_g = i_g(sL_g + r_g) \tag{2.32}$$

$$V_c = i_c(\frac{1}{sC} + r_d) \tag{2.33}$$

From eqs. (2.30) to (2.33) the LCL filter transfer functions can be derived, the equations are as follows.

$$\frac{i_g}{V_t} = \frac{Cr_d s+1}{CL_g L_i s^3+(CL_g r_d+CL_g r_i+CL_i r_d+CL_i r_g)s^2+(Cr_d r_g+Cr_d r_i+Cr_g r_i+L_g+L_i)s+r_g+r_i} \tag{2.34}$$

$$\frac{i_i}{V_t} = \frac{CL_g s^2+Cr_d s+Cr_g s+1}{CL_g L_i s^3+(CL_g r_d+CL_g r_i+CL_i r_d+CL_i r_g)s^2+(Cr_d r_g+Cr_d r_i+Cr_g r_i+L_g+L_i)s+r_g+r_i} \tag{2.35}$$

$$\frac{V_c}{V_t} = \frac{CL_g r_d s^2+(Cr_d r_g+L_g)s+r_g}{CL_g L_i s^3+(CL_g r_d+CL_g r_i+CL_i r_d+CL_i r_g)s^2+(Cr_d r_g+Cr_d r_i+Cr_g r_i+L_g+L_i)s+r_g+r_i} \tag{2.36}$$

The transfer functions for the LCL filter in eqs. (2.34) to (2.36) are complex and can be simplified by only considering the damping resistor r_d. If only r_d is considered the transfer functions can be simplified as follows.

$$\frac{i_g}{V_t} = \frac{Cr_d s+1}{CL_g L_i s^3+(CL_g r_d+CL_i r_d)s^2+(L_g+L_i)s} \tag{2.37}$$

$$\frac{i_i}{V_t} = \frac{CL_g s^2+Cr_d s+1}{CL_g L_i s^3+(CL_g r_d+CL_i r_d)s^2+(L_g+L_i)s} \tag{2.38}$$

$$\frac{V_c}{V_t} = \frac{CL_g r_d s^2+(Cr_d r_g+L_g)s}{CL_g L_i s^3+(CL_g r_d+CL_i r_d)s^2+(L_g+L_i)s} \tag{2.39}$$

The procedure for designing an LCL filter has been a discussed in many different literature [20][19][22], however the design procedure is not straight forward and often may require a redesign if specifications are not met or component sizes are too small. The first step is to decide on the design goals of the filter, for our design we will consider the following figures of merit for the filter [20]:

1. The decrease in power factor at the rated power will limit the size of the filter capacitor C_f. For the islanded condition the decrease in power factor will be limited to 10% max at the rated power.

2. The resonant frequency of the filter should ideally fall between $\frac{1}{2}$ the switching frequency on the upper end and 10 times the line frequency on the lower end. This helps avoid problems with resonance.

3. Passive damping should be used to avoid oscillation but optimized to have acceptable losses.

The system parameters for the LCL filter design are given in table 2.3.

Table 2.3: System parameters during black start

Parameter	Value	Unit
V_{pcc}	700	V
f_n	60	Hz
f_s	6	kHz
S_n	20	kVA

The LCL filter parameters are calculated using the system base values, and are calculated as follows.

$$Z_b = \frac{V_{pcc}^2}{P_n} = 24.5\Omega \tag{2.40}$$

$$C_b = \frac{1}{\omega_n Z_b} = 108.3\mu F \tag{2.41}$$

The general design procedure for the LCL filter is to first design the inverter side inductor L_i based on a specified current ripple, next an LC section is added. The capacitor C_f is designed as to limit the amount of reactive power supplied and the decrease in power factor at the nominal power output while the grid side inductor L_g is given as a percentage of the inverter side inductor based on the ripple attenuation from the inverter to grid.

To calculate the inverter side inductance equation 2.42 [20] can be used, where h_{sw} is the switching frequency harmonic.

$$\frac{i_i(h_{sw})}{v_i(h_{sw})} \approx \frac{1}{\omega_{sw} L_i} \tag{2.42}$$

$$\text{Let} \quad \frac{i_i(h_{sw})}{v_i(h_{sw})} = 1\%$$

$$0.01 \approx \frac{1}{\omega_{sw} L_i} \rightarrow L_i = 2.65mH \tag{2.43}$$

The inverter side inductance is calculated as $L_i = 2.65$mH based on a current ripple value of 1% on the inverter side, this value is rounded up to $L_i = 3$mH.

The filter capacitor C_f is calculated based on the limit in the decrease in the power factor at the nominal power output, which for the solid state transformer is 20 kVA.

$$C_f = 10\% \frac{1}{\omega_n Z_b} = 10.83\mu F \tag{2.44}$$

The calculated filter capacitor C_f value is $10.83\mu F$, this value is rounded up to $12\mu F$.

The grid side inductor is designed based on a ripple reduction of 25% as follows [20].

$$\frac{i_g(h_{sw})}{i_i(h_{sw})} = \frac{1}{|1 + r[1 - a \cdot x]|} \tag{2.45}$$

$$a = L_i C_b \omega_{sw}^2 \tag{2.46}$$

$$x = \frac{C_f}{C_b} \tag{2.47}$$

Therefore the values are found as $a = 461.755$ and $x = 0.110803$. With a 25% ripple reduction as the design, the grid side inductor can be calculated.

$$0.25 = \frac{1}{|1 + r[1 - 461.755 \cdot 0.110803]|} \rightarrow r = 0.099673 \tag{2.48}$$

The value r is the ratio between the grid side and converter side inductors, therefore the grid side inductor can be calculated as follows.

$$L_g = r \cdot L_i \rightarrow L_g = 270\mu H \tag{2.49}$$

With the LCL filter parameters determined, the resonant frequency of the filter can now be checked to determine if it falls within the requirements previously given. The resonant frequency can be calculated as follows.

$$\omega_{res} = \sqrt{\frac{L_i + L_g}{L_i L_g C}} = 18341.7 \frac{rad}{sec} \rightarrow f_{res} = 2919.18 Hz$$

The resonant frequency is 2919.18 Hz, this is close to half the switching frequency of 6000 Hz.

The final requirement is to add damping to the LCL filter at the resonant frequency where the impedance is zero. The damping resistor is set at a similar value as the magnitude of the capacitor impedance at the resonant frequency [20].

$$|X_c| = |\frac{1}{\omega_{res} C_f}| = 4.6\Omega \tag{2.50}$$

The resistance of the damping resistor r_d will be set to 1/3 of the impedance of the filter capacitor at the resonant frequency, therefore the damping resistance is $r_d \approx 1.6\Omega$.

The LCL filter parameters are summarized in table 2.4.

Table 2.4: LCL filter parameters

Parameter	Value	Unit
L_i	3	mH
C_f	12	μF
L_g	270	μH
r_d	1.6	Ω
f_{res}	2.92	kHz

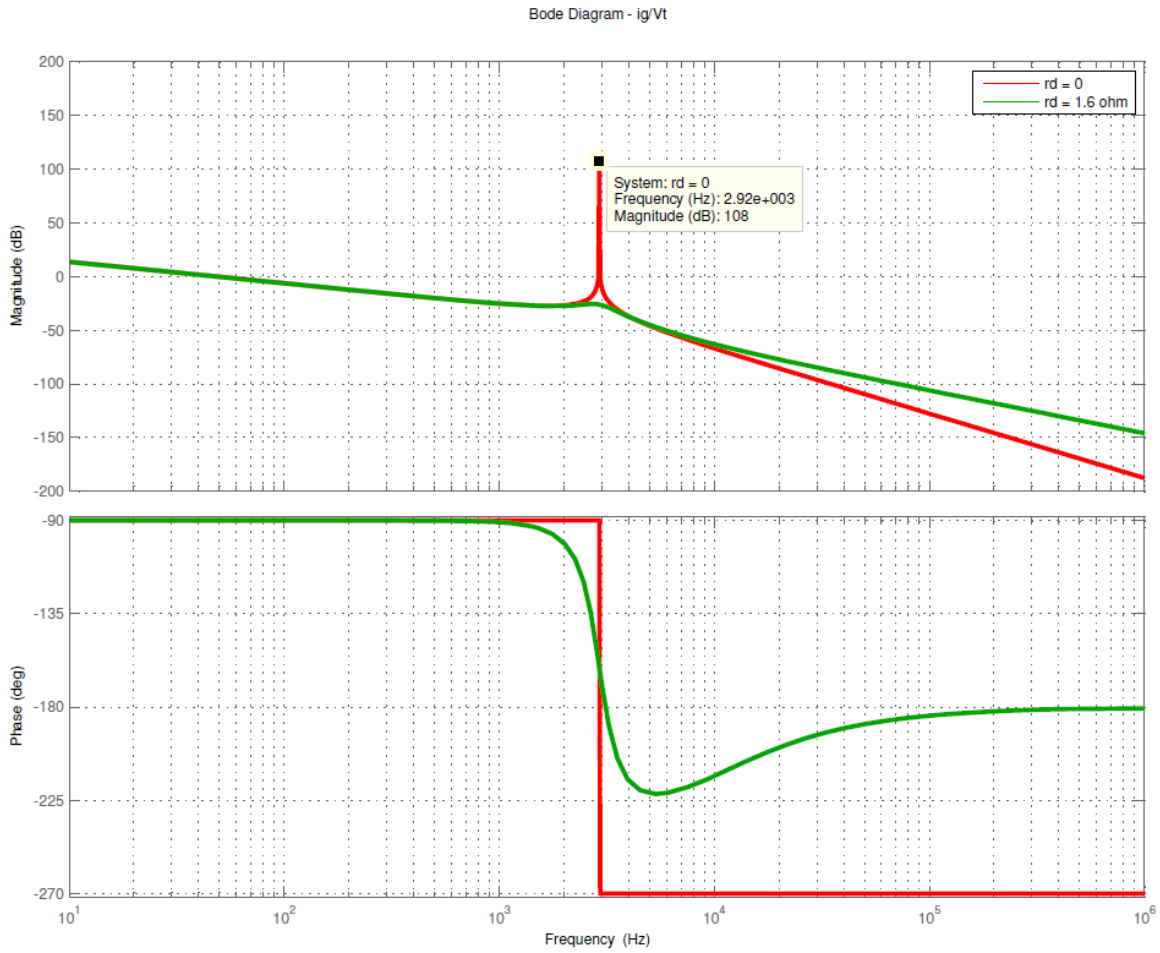

Figure 2.23: LCL filter $\frac{i_g}{V_t}$ comparison - damping vs no damping

The bode plot of $\frac{i_g}{V_t}$ is plotted in Figure 2.23 with the undamped ideal filter shown with the red line and the damped filter shown with the green line. The plot shows that the resonant frequency is indeed at 2.92 kHz as previously calculated and that the damping drastically reduces the resonant peaking which could cause stability problems. It can also be seen that the insertion of the damping resistor r_d causes decreased attenuation starting from the resonant peak into the high frequency region, this is a tradeoff between the filter attenuation and the stability gained from the damping resistor. Active damping methods such as using a virtual resistance to eliminate the losses associated with the damping resistor and other methods are available but they will not be considered here [23][24][25].

2.5.2 Grid-Tied Rectifier

The grid tied rectifier is connected to the grid with a filter inductor L and resistor R as shown in Figure 2.24, it is used to control the high side DC bus voltage V_H of the solid state transformers which have no battery energy storage systems and therefore cannot participate in the black start restoration procedure. The normal operating condition of the solid state transformer is the grid tied rectifier mode so it must be thoroughly analysed. It is very common for three-phase grid tied converters to have the controllers designed in the DQ (Direct Quadrature) synchronous reference frame, this allows for a change of variables from AC to DC thus allowing the use of PI (proportional plus integral) type compensators in the DQ frame which achieve a theoretically infinite loop gain and therefore allow excellent tracking of the reference waveforms. The transformation from the stationary frame to the synchronous reference frame requires at least two phases and therefore cannot be implemented on a single phase converter, however the use of an imaginary phase along with the actual phase of the converter has been used to perform DQ control on a single phase converter [26]. The single phase DQ control is used for the grid tied rectifier mode of operation and will be discussed in more detail.

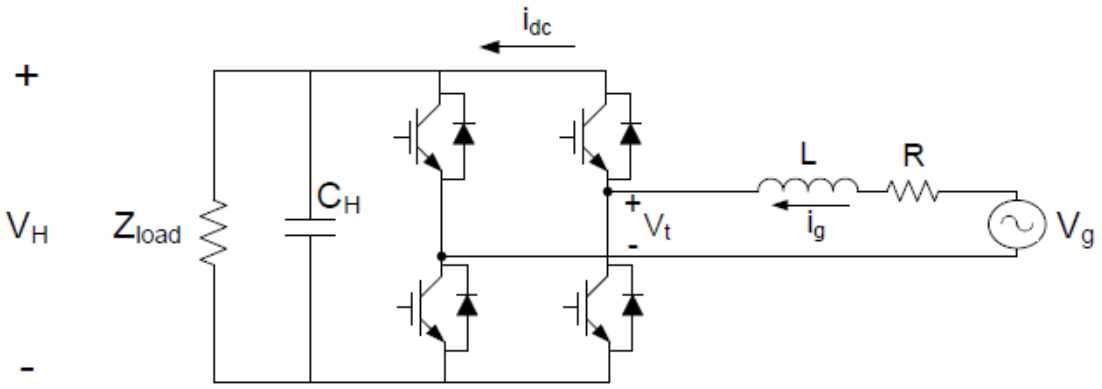

Figure 2.24: Grid-Tied Rectifier

2.5.3 DQ Frame Analysis

The transformation to the synchronous DQ reference frame allows the converter state variables to be changed from AC to DC and allows for simple compensator design, whereas compensator design would be much more complicated and higher order in the stationary reference frame. To perform the transformation from stationary to DQ reference frame, the converter state variables $\overline{\mathbf{x}}_{\mathbf{abc}}$ are initially transformed to another stationary frame of orthogonal vectors $\overline{\mathbf{x}}_{\alpha\beta}$ rotating counter-clockwise. Once the state variables are mapped to the $\alpha\beta$ stationary frame, the reference frame can be rotated at the same radial frequency synchronous to the state variable vectors $\overline{\mathbf{x}}_{\alpha\beta}$ which become the DQ vectors $\overline{\mathbf{x}}_{\mathbf{dq}}$, this is the DQ frame transformation. Once this transformation has been performed, the state variables and reference frame rotate at the same radial frequency and the $\alpha\beta$ vectors become constant in the DQ frame.

The frame transformation from $\alpha\beta$ to DQ is shown in Figure 2.25, the angle between the two frames can be calculated as follows, where θ_0 is the initial angle difference, t is the time, and ω is the angular frequency.

$$\theta = \int_0^t \omega(\tau)d\tau + \theta_0 \tag{2.51}$$

Figure 2.25 shows the state variable $\overline{\mathbf{x}}$ decomposed into its DQ and $\alpha\beta$ components. It can been seen that the state variable in the $\alpha\beta$ frame will vary with time, however if the vector components rotate at the same angular speed as the reference frame, than the state variables will not vary over time and are constant values.

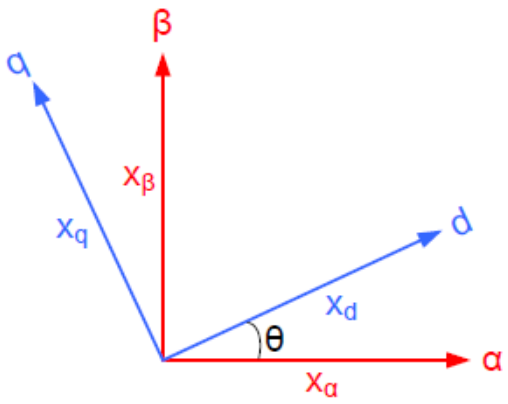

Figure 2.25: $\alpha\beta$ and DQ frames

The transformation between the $\alpha\beta$ and DQ frame is given as follows where the transformation is denoted as T. The transformation T is orthogonal and therefore $T^T = T^{-1}$ where T is defined in equation 2.54 where $\theta = 2\pi ft$ and f is the line frequency.

$$\overline{\mathbf{x}}_{\mathbf{dq}} = \mathbf{T}\overline{\mathbf{x}}_{\alpha\beta} \tag{2.52}$$

$$\overline{\mathbf{x}}_{\alpha\beta} = \mathbf{T}^{-\mathbf{1}}\overline{\mathbf{x}}_{\mathbf{dq}} \tag{2.53}$$

$$T = \begin{bmatrix} cos(\theta) & sin(\theta) \\ -sin(\theta) & cos(\theta) \end{bmatrix} \tag{2.54}$$

In order to perform the transformation the line frequency is necessary as seen in the transformation matrix, this is obtained by measuring at the PCC (point of common coupling) between the converter and the grid. A PLL (phase locked loop) is used to obtain the grid reference to perform the transformation, the PLL can be seen as the downside of using the DQ frame control as it requires its own analysis and control design.

2.5.4 Grid-Tied Rectifier Analysis

To transform the circuit into the DQ reference frame we first must create a second orthogonal phase, to do this we will use an imaginary circuit that is identical as the rectifier circuit with its state variables phase shifted by 90°. The real and imaginary single phase grid tied rectifier circuits are shown in Figure 2.26, the state variables in the imaginary circuit are phase shifted with respect to the real circuit. Two possible methods of obtaining the phase shifted state

variables of the imaginary circuit from the real circuit are either to introduce a quarter cycle delay, or to differentiate the state variables of the real circuit.

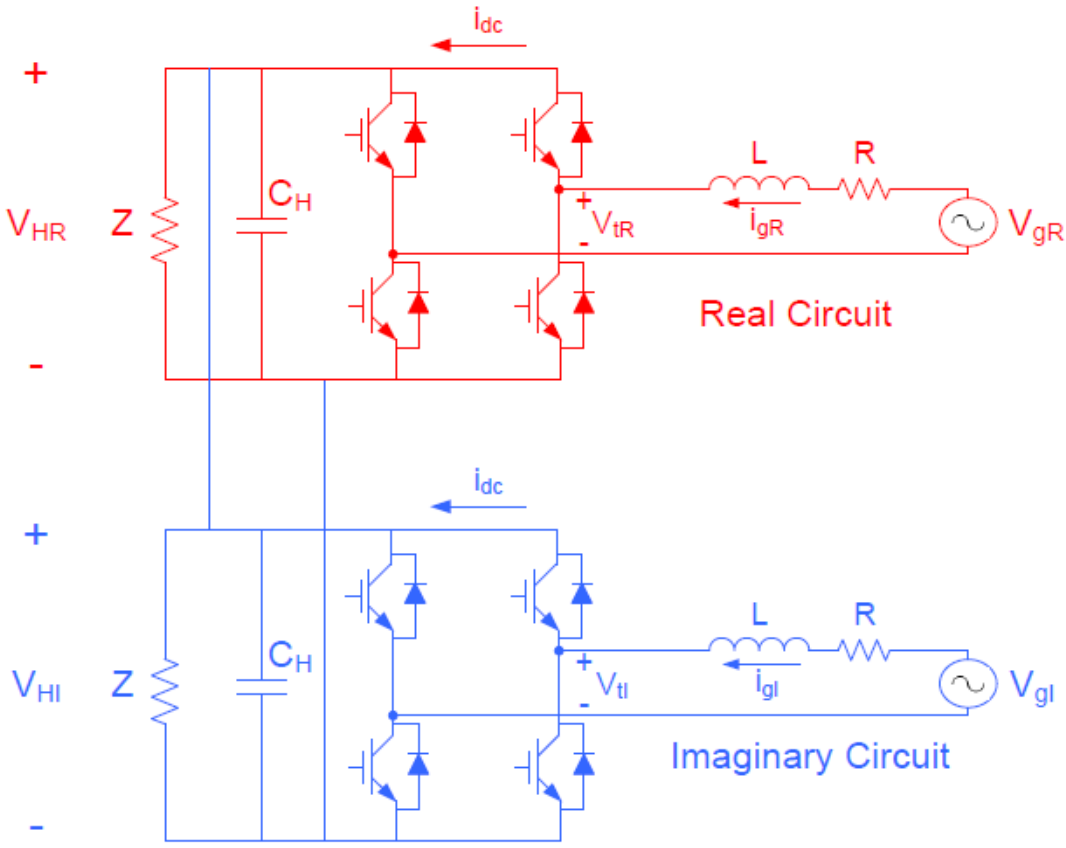

Figure 2.26: Real circuit and orthogonal imaginary circuit for $\alpha\beta$ transformation

The differential equations for the real and imaginary circuits can be derived using KCL and KVL in Figure 2.26, the equations are given in eqs. (2.55) to (2.58). Where $V_t = V_H S_{ab}(t)$ and $i_{dc} = i_g S_{ab}(t)$ and $S_{ab}(t)$ is the switching function of the inverter defined in Equation 2.59.

$$L\frac{di_{gR}}{dt} = -V_{gR} - Ri_{gR} + V_{HR}S_{abR}(t) \tag{2.55}$$

$$C_H\frac{dV_{HR}}{dt} = -i_{gR}S_{abR}(t) - \frac{V_{HR}}{Z} \tag{2.56}$$

$$L\frac{di_{gI}}{dt} = -V_{gI} - Ri_{gI} + V_{HI}S_{abI}(t) \tag{2.57}$$

$$C_H \frac{dV_{HI}}{dt} = -i_{g_I} S_{abI}(t) - \frac{V_{HI}}{Z} \tag{2.58}$$

$$S_{ab}(t) = \begin{cases} 1 & v_t(t) = V_H,\ i_{dc}(t) = i_g \\ 0 & v_t(t) = 0,\ i_{dc}(t) = 0 \\ -1 & v_t(t) = -V_H,\ i_{dc}(t) = -i_g \end{cases} \tag{2.59}$$

Applying the moving average operator in Equation 2.6 and ignoring the 120 Hz voltage ripple on the capacitor ($V_{HR} = V_{HI}$), the average model equations are given in eqs. (2.60) and (2.61) and can now be called α and β as the real and imaginary components are orthogonal.

$$L \frac{d\overline{I}_{g_{\alpha\beta}}}{dt} = -\overline{V}_{g_{\alpha\beta}} - R\overline{I}_{g_{\alpha\beta}} + V_H \overline{d}_{\alpha\beta} \tag{2.60}$$

$$C_H \frac{dV_H}{dt} = \frac{-\overline{I}_{g_{\alpha\beta}} \overline{d}_{\alpha\beta}}{2} - \frac{V_H}{Z} \tag{2.61}$$

With the average model now in the $\alpha\beta$ frame it can be transformed to the DQ frame using the transformation in Equation 2.62 as shown in eqs. (2.63) and (2.64) as defined previously in 2.25.

$$X_{\alpha\beta} = T^{-1} X_{dq} \tag{2.62}$$

$$L \frac{d}{dt}(T^{-1}\overline{I}_{g_{dq}}) = T^{-1}(-\overline{V}_{g_{dq}}) - RT^{-1}\overline{I}_{g_{dq}} + V_H T^{-1}\overline{d}_{dq} \tag{2.63}$$

$$C_H \frac{d}{dt} V_H = \frac{T^{-1}(-\overline{I}_{g_{dq}}) T^{-1} \overline{d}_{dq}}{2} - \frac{V_H}{Z} \tag{2.64}$$

The derivative term can be expanded using the chain rule as shown in Equation 2.65 where the identity in Equation 2.66 is needed, the DQ equations are given in eqs. (2.67) and (2.68).

$$L \frac{d}{dt}(T^{-1}\overline{I}_{g_{dq}}) = T^{-1} \frac{d}{dt} \overline{I}_{g_{dq}} + \overline{I}_{g_{dq}} \frac{d}{dt} T^{-1} \tag{2.65}$$

$$T \frac{d}{dt} T^{-1} = \begin{bmatrix} 0 & -\omega \\ \omega & 0 \end{bmatrix} \tag{2.66}$$

$$\frac{d}{dt} \begin{bmatrix} \overline{I}_{g_d} \\ \overline{I}_{g_q} \end{bmatrix} = \frac{-1}{L} \begin{bmatrix} \overline{V}_{g_d} \\ \overline{V}_{g_q} \end{bmatrix} + \begin{bmatrix} \frac{-R}{L} & \omega \\ -\omega & \frac{-R}{L} \end{bmatrix} \begin{bmatrix} \overline{I}_{g_d} \\ \overline{I}_{g_q} \end{bmatrix} + \frac{1}{L} \begin{bmatrix} \overline{d}_d \\ \overline{d}_q \end{bmatrix} V_H \tag{2.67}$$

$$\frac{d}{dt}V_H = \frac{-1}{2C_H}\begin{bmatrix}\bar{d}_d \\ \bar{d}_q\end{bmatrix}^T \begin{bmatrix}\bar{I}_{g_d} \\ \bar{I}_{g_q}\end{bmatrix} - \frac{V_H}{ZC_H} \tag{2.68}$$

The rectifier average model in DQ coordinates is based on eqs. (2.67) and (2.68) and is shown in Figure 2.27, it can be seen that a coupling between the D and Q circuits is introduced from the transformation, this can be easily compensated in the control design. For simplification the Q channel voltage V_{gQ} is set to 0, this allows for the nominal input voltage to be used directly as the D channel input voltage V_{gD}, also it can be shown that if $V_q = 0$ than the real power is proportional to I_d and reactive power is proportional to I_q, therefore we control $I_q = 0$ for unity power factor operation [15].

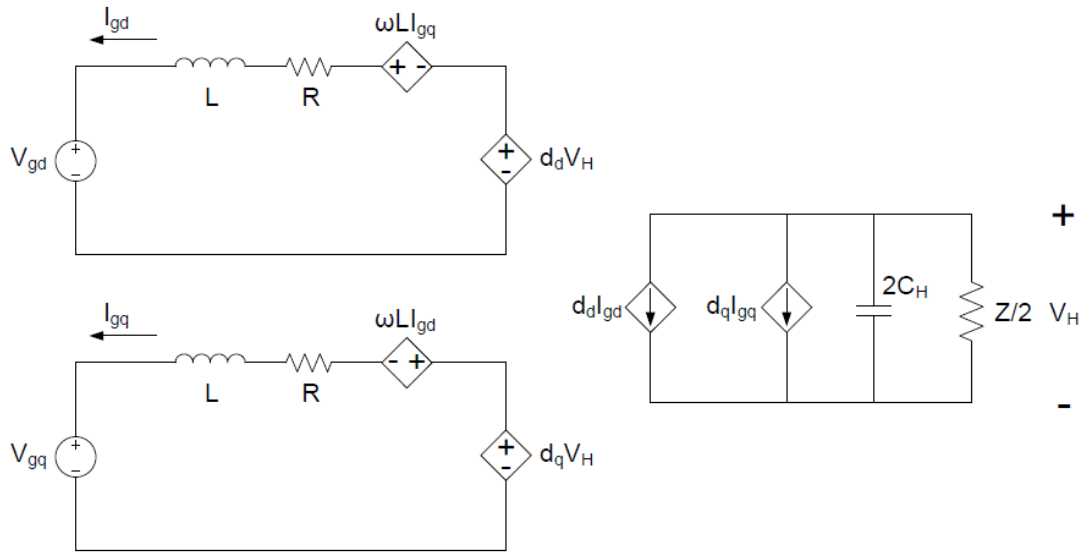

Figure 2.27: Rectifier average model

The steady state operating point equations are given in eqs. (2.69) to (2.73) are developed by considering the average model and the capacitor current and inductor voltage equal to 0.

$$V_{gq} = 0 \tag{2.69}$$

$$I_{gq} = 0 \tag{2.70}$$

$$D_d = \frac{V_{gd} + I_d R}{V_H} \tag{2.71}$$

$$D_q = \frac{\omega L I_{gd}}{V_H} \tag{2.72}$$

$$I_{gd} = \frac{-2V_H}{D_d Z} \tag{2.73}$$

The small-signal model can be derived by adding a perturbation around the operating point of the average model, the small-signal equations are given in eqs. (2.74) and (2.75) and the state-space model is given in Equation 2.76.

$$\frac{d}{dt}\begin{bmatrix}\widetilde{i}_{gd}\\ \widetilde{i}_{gq}\end{bmatrix} = -\frac{1}{L}\begin{bmatrix}\widetilde{v}_{gd}\\ \widetilde{v}_{gq}\end{bmatrix} + \begin{bmatrix}\frac{-R}{L} & \omega\\ -\omega & \frac{-R}{L}\end{bmatrix}\begin{bmatrix}\widetilde{i}_{gd}\\ \widetilde{i}_{gq}\end{bmatrix} + \frac{V_H}{L}\begin{bmatrix}\widetilde{d}_d\\ \widetilde{d}_q\end{bmatrix} + \frac{1}{L}\begin{bmatrix}D_d\\ D_q\end{bmatrix}\widetilde{v}_H \tag{2.74}$$

$$\frac{d}{dt}\widetilde{v}_H = -\frac{1}{2C_H}\begin{bmatrix}D_d\\ D_q\end{bmatrix}^T\begin{bmatrix}\widetilde{i}_{gd}\\ \widetilde{i}_{gq}\end{bmatrix} - \frac{1}{2C_H}\begin{bmatrix}I_{gd}\\ I_{gq}\end{bmatrix}^T\begin{bmatrix}\widetilde{d}_d\\ \widetilde{d}_q\end{bmatrix} - \frac{V_H}{ZC_H} \tag{2.75}$$

$$\frac{d}{dt}\begin{bmatrix}\widetilde{i}_{gd}\\ \widetilde{i}_{gq}\\ \widetilde{v}_H\end{bmatrix} = \begin{bmatrix}-\frac{R}{L} & \omega & \frac{D_d}{L}\\ -\omega & -\frac{R}{L} & \frac{D_q}{L}\\ \frac{-D_d}{2C_H} & \frac{-D_q}{2C_H} & \frac{-1}{ZC_H}\end{bmatrix}\begin{bmatrix}\widetilde{i}_{gd}\\ \widetilde{i}_{gq}\\ \widetilde{v}_H\end{bmatrix} + \begin{bmatrix}\frac{V_H}{L} & 0\\ 0 & \frac{V_H}{L}\\ \frac{-I_{gd}}{2C_H} & \frac{-I_{gq}}{2C_H}\end{bmatrix}\begin{bmatrix}\widetilde{d}_d\\ \widetilde{d}_q\end{bmatrix} + \begin{bmatrix}\frac{-1}{L} & 0\\ 0 & \frac{-1}{L}\\ 0 & 0\end{bmatrix}\begin{bmatrix}\widetilde{v}_{gd}\\ \widetilde{v}_{gq}\end{bmatrix} \tag{2.76}$$

The control design can now be based on the small-signal state space matrices.

2.5.5 Black Start Inverter

The black start inverter operates to maintain the microgrid distribution voltage using any DRER and DESD as the power source. The black start inverter is shown in Figure 2.28, it is modeled as a standalone inverter where the grid impedance Z_g models the power delivered to the distribution line and other solid state transformers without black start resources.

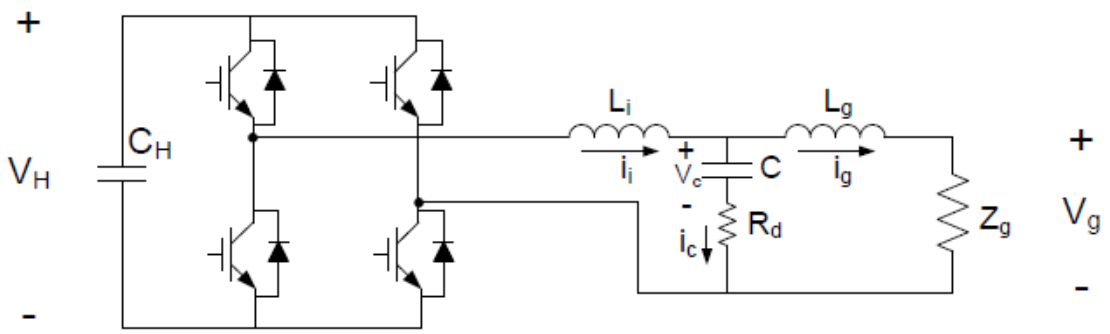

Figure 2.28: Black start inverter

Placing the switch model from Figure 2.1 into the black start inverter we find the simplified model as shown in Figure 2.29. From this circuit model can determine the state space model which can be used for control design.

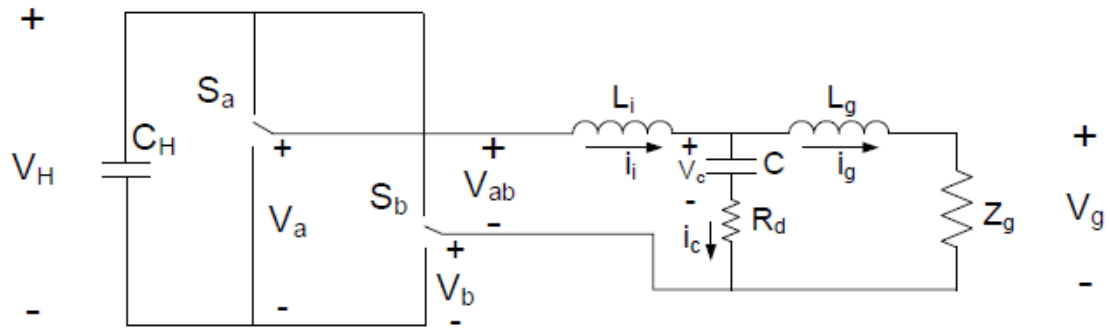

Figure 2.29: Simplified black start inverter

We can write the following differential equations by applying KVL and KCL to the simplified circuit model.

$$C\frac{dV_c}{dt} = i_i - i_g \tag{2.77}$$

$$L_i\frac{di_i}{dt} = V_{ab} - V_c - R_d i_c = V_{ab} - V_c - R_d i_i + R_d i_g \tag{2.78}$$

$$L_g\frac{di_g}{dt} = V_c - V_g + R_d i_c = V_c + R_d i_i - (Z_g + R_d) i_g \tag{2.79}$$

From the previous phase leg analysis we found the average output of a phase leg, we can now find the output voltage V_{ab} with a similar analysis.

$$\begin{aligned} V_a &= S_a V_H \\ V_b &= S_b V_H \\ V_{ab} &= V_a - V_b = S_{ab} V_H \\ &\therefore \text{from previous analysis} \\ \overline{V}_{ab} &= d V_H \end{aligned} \tag{2.80}$$

Using equations 2.80 and averaging the variables, we can obtain the averaged state space equations:

$$C\frac{d\overline{V}_c}{dt} = \bar{i}_i - \bar{i}_g \tag{2.81}$$

$$L_i\frac{d\bar{i}_i}{dt} = dV_H - \overline{V}_c - R_d\bar{i}_i + R_d\bar{i}_g \tag{2.82}$$

$$L_g\frac{d\bar{i}_g}{dt} = \overline{V}_c + R_d\bar{i}_i - (Z_g + R_d)\bar{i}_g \tag{2.83}$$

Finally, adding a small perturbation to eqs. (2.81) to (2.83) and only keeping first order terms we can find the small signal model as given in 2.84.

$$\boxed{\begin{bmatrix} \dot{\hat{V}}_c \\ \dot{\hat{i}}_i \\ \dot{\hat{i}}_g \end{bmatrix} = \begin{bmatrix} 0 & \frac{1}{C} & -\frac{1}{C} \\ -\frac{1}{L_i} & -\frac{R_d}{L_i} & \frac{R_d}{L_i} \\ \frac{1}{L_g} & \frac{R_d}{L_g} & \frac{-Z_g - R_d}{L_g} \end{bmatrix} \begin{bmatrix} \hat{V}_c \\ \hat{i}_i \\ \hat{i}_g \end{bmatrix} + \begin{bmatrix} 0 \\ \frac{V_H}{L_i} \\ 0 \end{bmatrix} \hat{d}} \tag{2.84}$$

Again using the small signal state space in equation 2.84, the transfer functions for this system can be derived.

$$\frac{\hat{V}_c}{\hat{d}} = V_H \frac{L_g s + Z_g}{CL_gL_is^3 + (CL_iR_d + CL_gR_d + CL_iZ_g)s^2 + (L_i + L_g + CR_dZ_g)s + Z_g} \tag{2.85}$$

$$\frac{\hat{i}_i}{\hat{d}} = V_H \frac{CL_gs^2 + (CR_d + CZ_g)s + 1}{CL_gL_is^3 + (CL_iR_d + CL_gR_d + CL_iZ_g)s^2 + (L_i + L_g + CR_dZ_g)s + Z_g} \tag{2.86}$$

$$\frac{\hat{i}_g}{\hat{d}} = V_H \frac{CR_d s + 1}{CL_g L_i s^3 + (CL_i R_d + CL_g R_d + CL_i Z_g)s^2 + (L_i + L_g + CR_d Z_g)s + Z_g} \tag{2.87}$$

The inverter operates in two modes as shown in Figure 2.30. When excess power is generated by the DRER or PV system meaning the battery bank is fully charged, the inverter operates in grid connected mode supplying the power to the grid. During black start operation, the inverter operates as a standalone inverter supplying a load. Because of the complexity involved in the simulation the grid connected mode where the inverter supplies excess power to the grid is not simulated but the analysis for this mode is done. The standalone inverter mode supplying a load is critical to the black start procedure which is the main topic of this work and is therefore analysed fully.

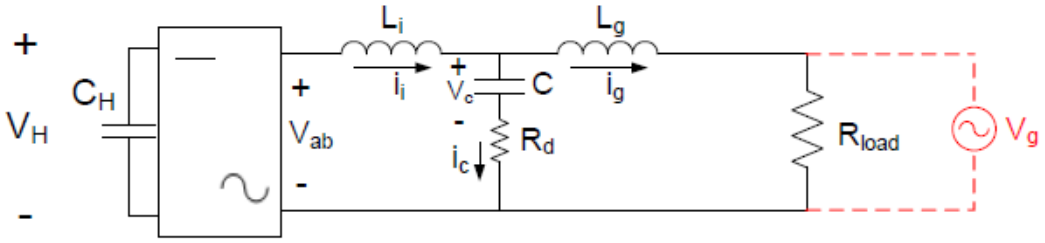

Figure 2.30: Inverter operating modes

Because of the complexity of the plant model as given in Equation 2.84, a block diagram average model of the inverter is developed to simplify the analysis of the converter [27]. The model is shown in Figure 2.31 for the grid connected LCL filter inverter where $u(s)$ is the modulating signal, $G_{pwm}(s)$ represents the pwm gain and delay $G_{pwm}(s) = V_H e^{-T_d s}$ however the time delay is not considered here and only the DC input voltage is considered. The other blocks represent the LCL filters behaviour where R_d is the capacitor series damping resistor. The grid voltage input is indicated as V_g.

The black start block diagram model is shown in Figure 2.32, the black start model does not have the grid voltage and also it considers the load resistance R_{load} with the grid side inductor L_g.

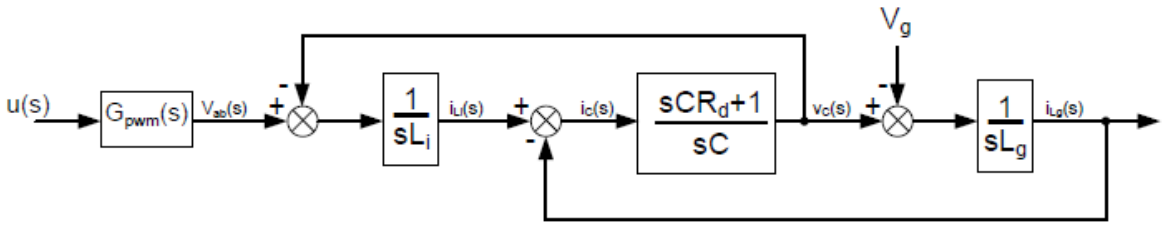

Figure 2.31: Grid connected model

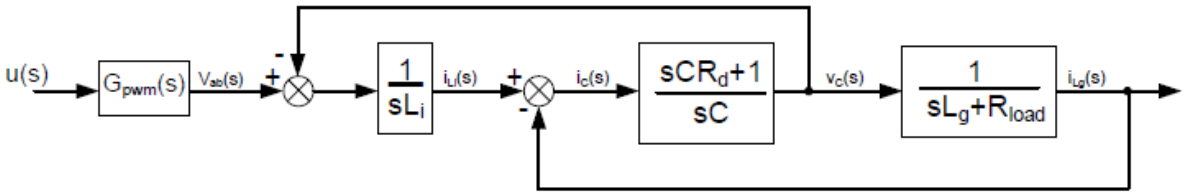

Figure 2.32: Black start model

The control design using the models for the grid connected and black start operating modes are analysed later.

2.6 Battery DC/DC Bidirectional Converter

The battery DC/DC bidirectional converter defines a black start solid state transformer, the battery and converter system allows the solid state transformer to regulate the low voltage DC bus voltage during the black start procedure, it acts as the power source while the grid connection is lost. In grid connected mode the battery is kept fully charged, and can be discharged depending on certain system criteria such as energy prices and system loading. In this study the battery is kept fully charged while a grid connection is available and the battery is used as the energy source while the grid connection is lost, the grid connected battery discharge mode is not considered here.

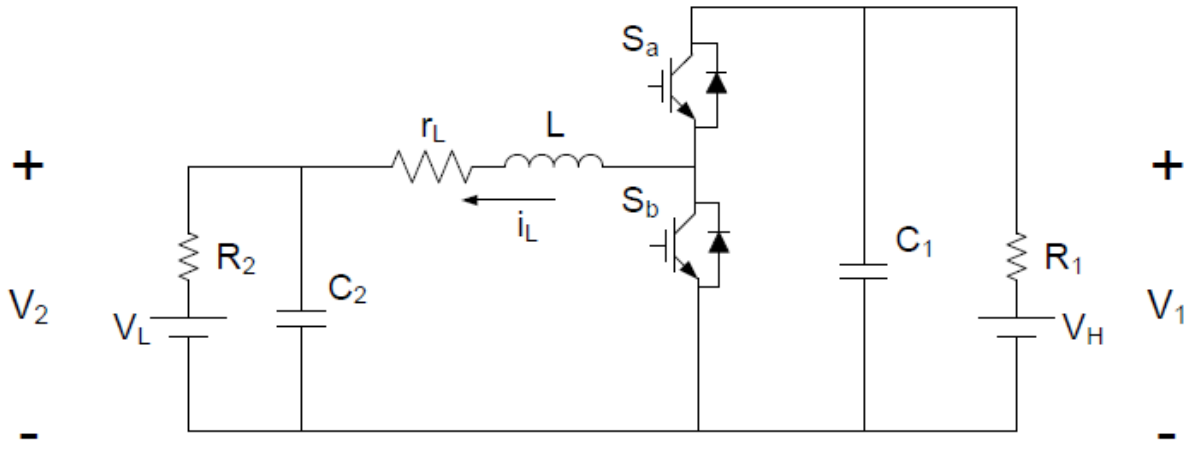

Figure 2.33: Battery DC/DC converter

Figure 2.33 is a general model for both of the conditions that the converter can operate whether in grid connected or islanded mode of operation, the same concept as the multi-use model in [28]. In grid connected mode, the converter low side voltage V_L is equal to the battery voltage while the high side voltage V_H is equal to the low voltage DC bus capacitor C_L voltage which is controlled by the DAB. During a black start condition, the converter low side voltage V_L is the battery voltage while the high side voltage V_H is set to 0 and R_1 becomes the battery load. In either mode of operation R_2 represents the battery internal resistance. The switches operate complementary such that $S_a = \overline{S}_b$, so the converter can be analysed in each switch position and then averaged. The simplified model is shown in Figure 2.34.

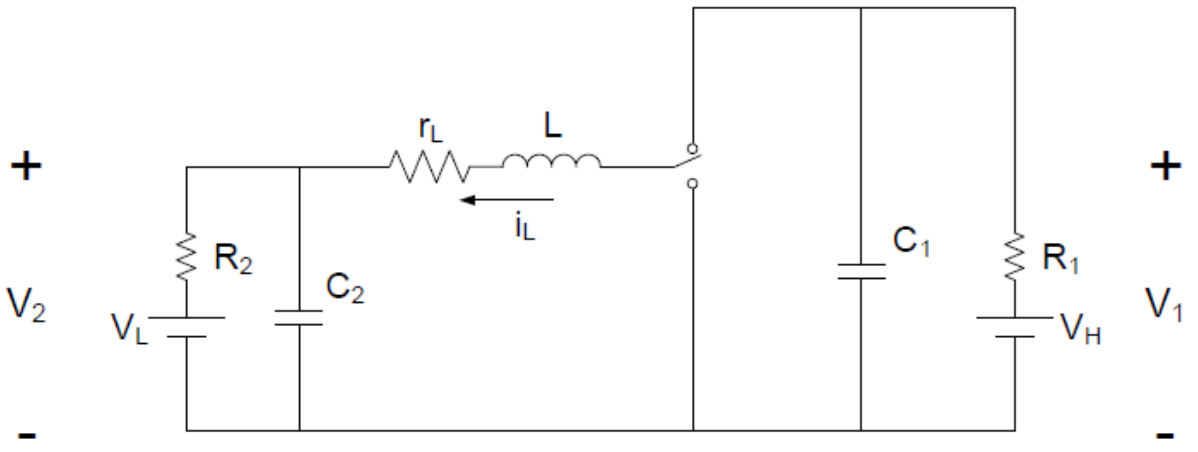

Figure 2.34: Simplified battery DC/DC converter

Applying KVL and KCL the differential equations can be written for the upper switch position.

$$L\frac{di_L}{dt} = V_1 - V_2 - r_L i_L \tag{2.88}$$

$$C_1\frac{dV_1}{dt} = -\frac{V_1 - V_H}{R_1} - i_L \tag{2.89}$$

$$C_2\frac{dV_2}{dt} = i_L - \frac{V_2 - V_L}{R_2} \tag{2.90}$$

And in the bottom switch position, the following equations can be obtained.

$$L\frac{di_L}{dt} = -V_2 - r_L i_L \tag{2.91}$$

$$C_1\frac{dV_1}{dt} = -\frac{V_1 - V_H}{R_1} \tag{2.92}$$

$$C_2\frac{dV_2}{dt} = i_L - \frac{V_2 - V_L}{R_2} \tag{2.93}$$

The first set of equations corresponding to the top switch position, eqs. (2.88) to (2.90), and the second set of equations corresponding to the bottom switch position eqs. (2.91) to (2.93), can be averaged by comparing the corresponding equations individually.

$$L\frac{d\bar{i}_L}{dt} = D\overline{V}_1 - \overline{V}_2 - r_L\bar{i}_L \tag{2.94}$$

$$C_1\frac{d\overline{V}_1}{dt} = -\frac{\overline{V}_1 - V_H}{R_1} - D\bar{i}_L \tag{2.95}$$

$$C_2\frac{d\overline{V}_2}{dt} = \bar{i}_L - \frac{\overline{V}_2 - V_L}{R_2} \tag{2.96}$$

The steady state converter output can be determined by setting the differential terms to zero in eqs. (2.94) to (2.96) and solving the set of algebraic equations. The steady state values of the converter are given in eqs. (2.97) to (2.99).

$$i_L = \frac{DV_H - V_L}{R_1D^2 + R_2 + r_L} \tag{2.97}$$

$$V_1 = \frac{R_2V_H + r_LV_H + DR_1V_L}{R_1D^2 + R_2 + r_L} \tag{2.98}$$

$$V_2 = \frac{R_1 V_L D^2 + R_2 V_H D + V_L r_L}{R_1 D^2 + R_2 + r_L} \tag{2.99}$$

Again to find the small signal state space equations a perturbation is applied to the circuit and the averaged state space equations are rewritten keeping only first order terms. The small signal state space equations are written in eqs. (2.100) to (2.102).

$$L\frac{d\hat{i}_L}{dt} = V_1\hat{d} + D\hat{V}_1 - r_L\hat{i}_L - \hat{V}_2 \tag{2.100}$$

$$C_1\frac{d\hat{V}_1}{dt} = -\frac{\hat{V}_1 - \hat{V}_H}{R_1} - I_L\hat{d} - D\hat{i}_L \tag{2.101}$$

$$C_2\frac{d\hat{V}_2}{dt} = \hat{i}_L - \frac{\hat{V}_2 - \hat{V}_L}{R_2} \tag{2.102}$$

The small signal state space matrix can be written as 2.103, the sources V_H and V_L are assumed to be stiff sources and therefore $\hat{V}_H$ and $\hat{V}_L$ are zero.

$$\boxed{\begin{bmatrix} \dot{\hat{i}}_L \\ \dot{\hat{V}}_1 \\ \dot{\hat{V}}_2 \end{bmatrix} = \begin{bmatrix} -\frac{r_L}{L} & \frac{D}{L} & -\frac{1}{L} \\ -\frac{D}{C_1} & -\frac{1}{R_1 C_1} & 0 \\ \frac{1}{C_2} & 0 & -\frac{1}{R_2 C_2} \end{bmatrix} \begin{bmatrix} \hat{i}_L \\ \hat{V}_1 \\ \hat{V}_2 \end{bmatrix} + \begin{bmatrix} \frac{V_1}{L} \\ -\frac{I_L}{C_1} \\ 0 \end{bmatrix} \hat{d}} \tag{2.103}$$

The system transfer functions are derived from the small signal state space equation 2.103.

$$\frac{\hat{i}_L}{\hat{d}} = \frac{C_1C_2R_1R_2V_1s^2+(C_1R_1V_1+C_2R_2V_1-DC_2I_LR_1R_2)s-DI_LR_1+V_1}{C_1C_2LR_1R_2s^3+(C_1C_2R_1R_2r_L+C_2LR_2+C_1LR_1)s^2+(C_2R_2r_L+C_1R_1r_L+C_1R_1R_2+C_2D^2R_1R_2+L)s+D^2R_1+R_2+r_L} \tag{2.104}$$

$$\frac{\hat{V}_1}{\hat{d}} = \frac{-C_2I_LLR_1R_2s^2-R_1(I_LL+C_2DR_2V_1+C_2I_LR_2r_L)s-R_1(I_Lr_L+DV_1+I_LR_2)}{C_1C_2LR_1R_2s^3+(C_1C_2R_1R_2r_L+C_2LR_2+C_1LR_1)s^2+(C_2R_2r_L+C_1R_1r_L+C_1R_1R_2+C_2D^2R_1R_2+L)s+D^2R_1+R_2+r_L} \tag{2.105}$$

$$\frac{\hat{V}_1}{\hat{d}} = \frac{C_1R_1R_2V_1s-DI_LR_1R_2+R_2V_1}{C_1C_2LR_1R_2s^3+(C_1C_2R_1R_2r_L+C_2LR_2+C_1LR_1)s^2+(C_2R_2r_L+C_1R_1r_L+C_1R_1R_2+C_2D^2R_1R_2+L)s+D^2R_1+R_2+r_L} \tag{2.106}$$

In order to simplify the analysis of the battery DC/DC bidirectional converter we will consider the two cases which the converter will operate, grid connected mode and islanded mode. The first case, grid connected mode is shown in Figure 2.35.

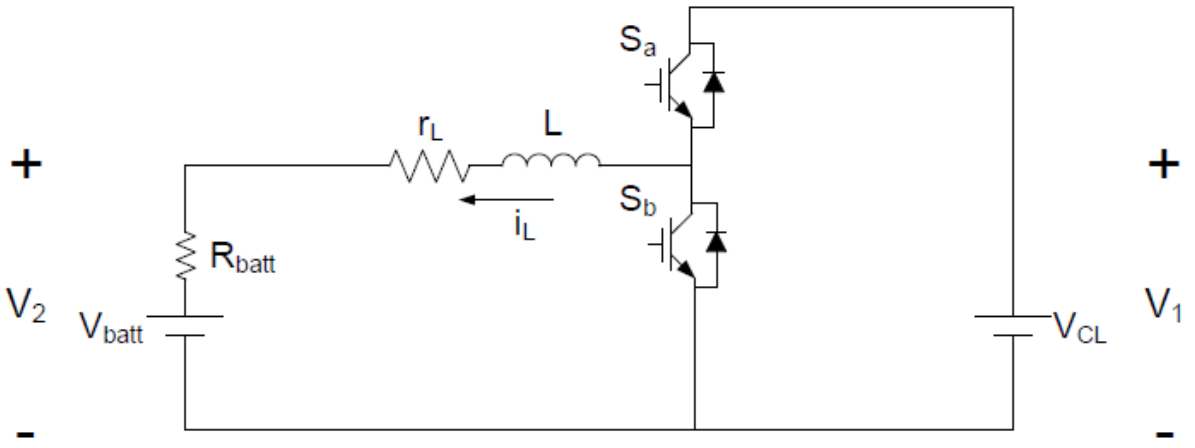

Figure 2.35: Grid connected battery DC/DC converter

In the grid connected battery converter, the resistance R_1 is ignored since $V_1 = V_H = V_{CL}$. Because both ends of the converter have voltage sources connected, one grid controlled while the other is the battery bank, the capacitors C_1 and C_2 can be ignored. The resistance R_2 becomes the battery internal resistance and for this analysis is assumed to be small and negligible. The steady state equations and transfer functions can now be simplified.

$$V_1 = V_{CL} \tag{2.107}$$

$$V_2 = V_{batt} \tag{2.108}$$

$$I_L = \frac{DV_{CL} - V_{batt}}{r_L} \tag{2.109}$$

$$\frac{\hat{i}_L}{\hat{d}} = \frac{V_{CL}}{Ls + r_L} \tag{2.110}$$

The second case, islanded mode, is shown in Figure 2.36. The resistance R_1 becomes the equivalent load of the solid state transformer during the black start procedure and the voltage source V_H is ignored, the capacitor C_2 is ignored because a voltage source is connected across its terminals. Again, R_2 becomes the battery internal resistance R_{batt}. Again, the battery resistance is assumed to be small and negligible. Finally, the capacitor C_1 is renamed to C_L because this capacitor is the low voltage capacitor C_L in the solid state transformer system.

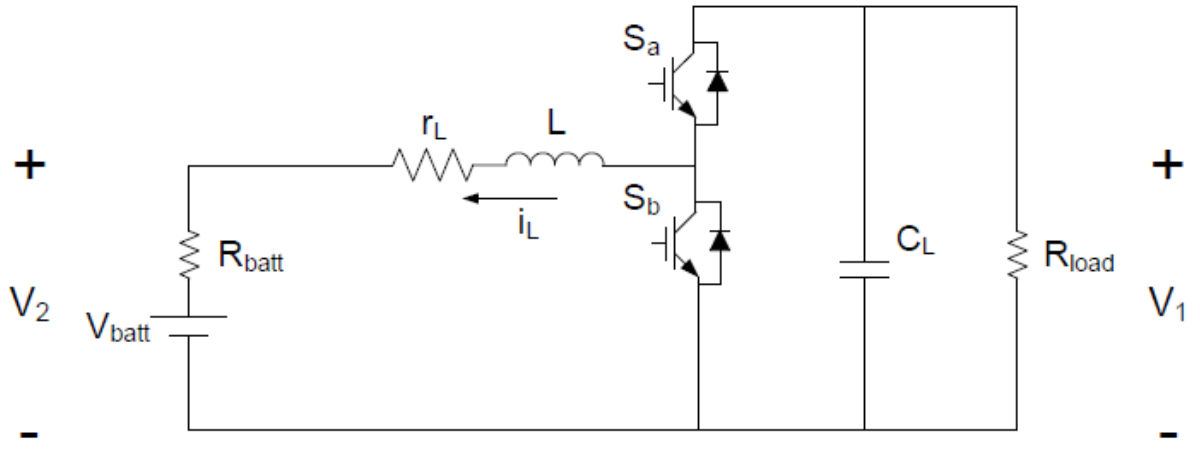

Figure 2.36: Islanded battery DC/DC converter

$$V_1 = \frac{DR_{load}V_{batt}}{R_{load}D^2 + r_L} \tag{2.111}$$

$$V_2 = V_{batt} \tag{2.112}$$

$$I_L = -\frac{V_{batt}}{R_{load}D^2 + r_L} \tag{2.113}$$

$$\frac{\hat{i}_L}{\hat{d}} = \frac{C_L R_{load} V_1 s - D I_L R_{load} + V_1}{C_L L R_{load} s^2 + (C_L R_{load} r_L + L)s + r_L + D^2 R_{load}} \tag{2.114}$$

$$\frac{\hat{V}_1}{\hat{d}} = \frac{-R_{load} I_L s - R_{load} I_L r_L - R_{load} D V_1}{C_L L R_{load} s^2 + (C_L R_{load} r_L + L)s + r_L + D^2 R_{load}} \tag{2.115}$$

The transfer function $\frac{\hat{V}_1}{\hat{d}}$ is determined by simulation and compared with the calculated transfer function in equation 2.115. The parameters for the bidirectional battery converter are given in table 2.5.

Table 2.5: Bidirectional Converter Parameters

Battery Bidirectional Converter Parameters		
Parameter	Value	Unit
V_{batt}	206	V
f_s	6	kHz
L	5	mH
r_L	0.5	Ω
C_L	2	mF
R_{load}	1600	Ω

The control to output transfer functions in eqs. (2.114) and (2.115) can be rewritten using the parameters as given in eqs. (2.116) and (2.117) below.

$$\frac{\hat{i}_L}{\hat{d}} = \frac{1280s + 800}{0.016s^2 + 1.605s + 423.9} \tag{2.116}$$

$$\frac{\hat{V}_1}{\hat{d}} = \frac{3.88s - 3.288e5}{0.016s^2 + 1.605s + 423.9} \tag{2.117}$$

The simulation is shown in figs. 2.37 and 2.38.

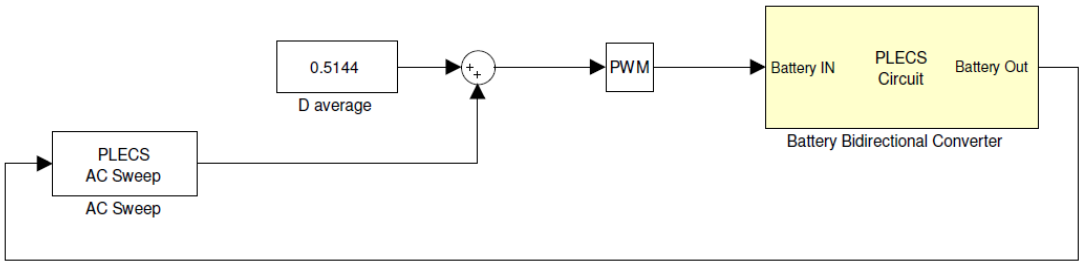

Figure 2.37: Bidirectional battery converter test

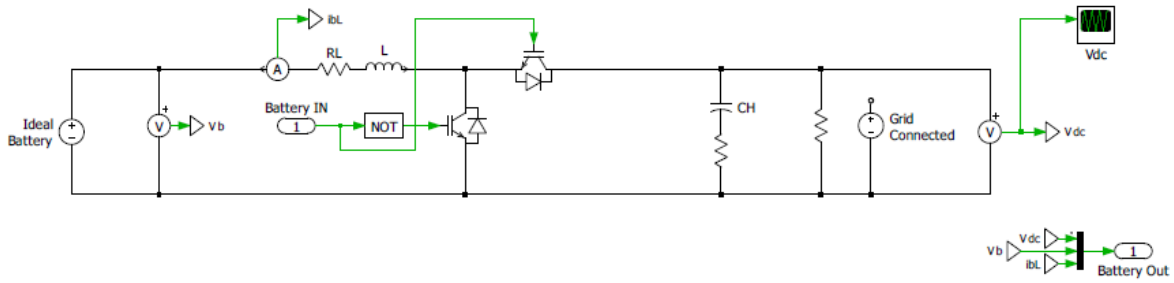

Figure 2.38: Bidirectional battery converter circuit

The simulation results and the calculated results are plotted in figs. 2.39 and 2.40 for the transfer functions $\frac{\hat{i}_L}{\hat{d}}$ and $\frac{\hat{V}_1}{\hat{d}}$. From the plots we can see that the calculated results closely match the simulated results for the battery bidirectional converter.

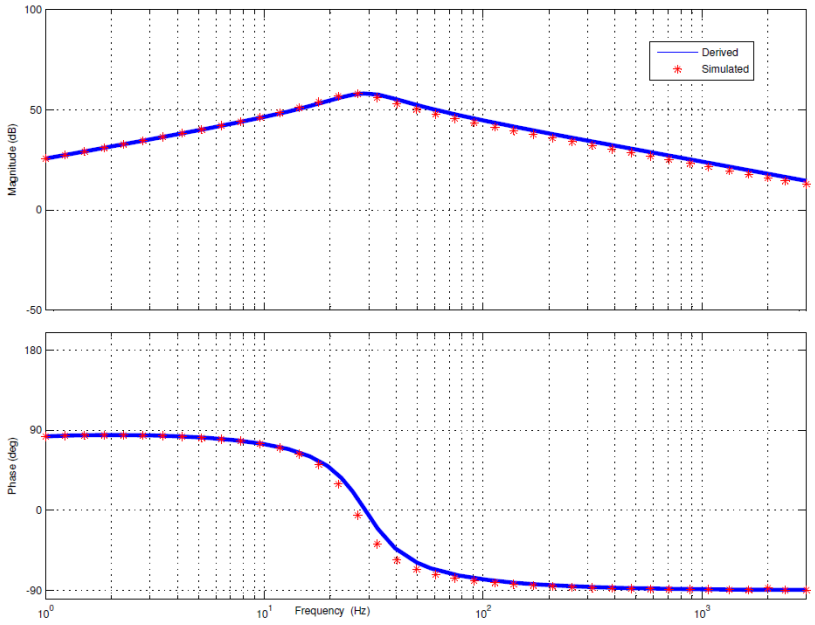

Figure 2.39: $\frac{\hat{i}_L}{\hat{d}}$ simulated and calculated

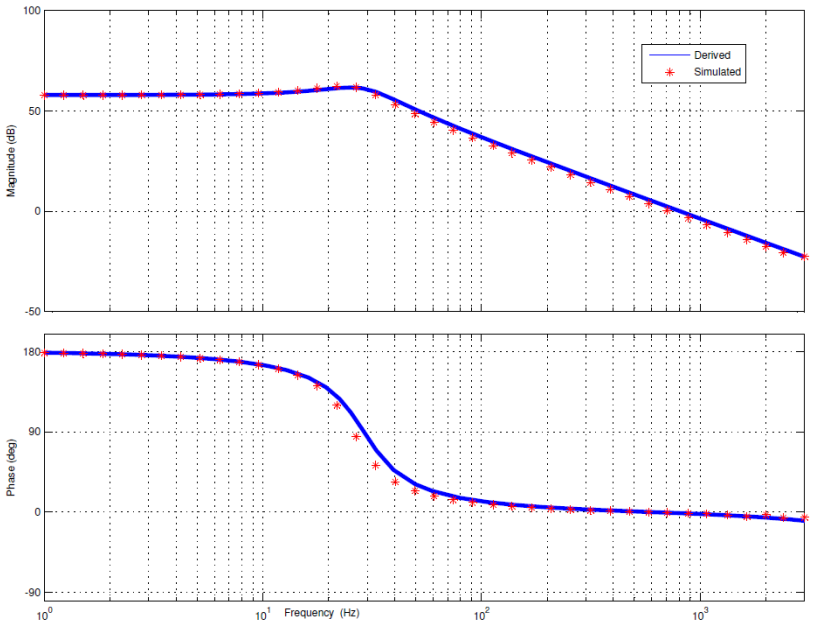

Figure 2.40: $\frac{\hat{V}_1}{\hat{d}}$ simulated and calculated

2.7 Photovoltaic Panel Boost Converter

A photovoltaic (PV) panel array is interfaced to the solid state transformer through a boost converter. The boost converter uses the low voltage DC capacitor C_L bus as a voltage source to increase the PV terminal voltage such that the maximum power is injected. Whether in grid connected or islanded mode of operation, the boost converter operates the same.

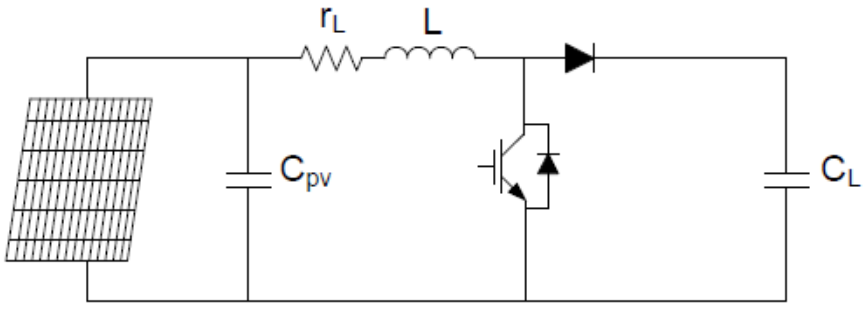

Figure 2.41: PV boost converter

The PV panels are assumed to be exposed to the same amount of sunlight and are the same temperature, in this case the PV panels can be approximately modeled by equations eqs. (2.118) to (2.120) [29].

$$i_{pv} = n_p I_{ph} - n_p I_{rs}[exp(\frac{qv_{dc}}{kTAn_s}) - 1] \tag{2.118}$$

$$I_{ph} = 0.01[I_{scr} + K_\theta(T - T_r)]S \tag{2.119}$$

$$P_{pv} = n_p I_{ph} v_{dc} - n_p I_{rs} v_{dc}[exp(\frac{qv_{dc}}{kTAn_s}) - 1] \tag{2.120}$$

Where I_{rs} is the reverse saturation current of the cell, n_p is the number of parallel cells, n_s is the number of series cells, I_{ph} is the photovoltaic current, q is the unit charge constant, k is Boltzman's constant, T is the cell temperature, A is the ideality factor of the p-n junction, I_{scr} is the cell short circuit current at reference radiation and temperature, K_θ is a temperature coefficient, T_r is the reference temperature for the reverse saturation current, S is the solar irradiation.

A 5 kW PV array system is designed for the boost converter, the variable values in eqs. (2.118) to (2.120) are given in Table 2.6.

Table 2.6: PV panel design

PV Panel Parameters		
Parameter	Value	Unit
n_p	500	cells
n_s	255	cells
I_{scr}	8.03	A
K_θ	0.0017	A/K
T	298	K
T_r	300	K
I_{rs}	1.2e-7	A
q	1.602e-19	C
k	1.38e-23	$\frac{J}{K}$
A	1.92	-

With the PV array as designed in table 2.6, the output current versus DC voltage V_{dc} and

output power versus V_{dc} can be plotted by using the previous equations eqs. (2.118) to (2.120).

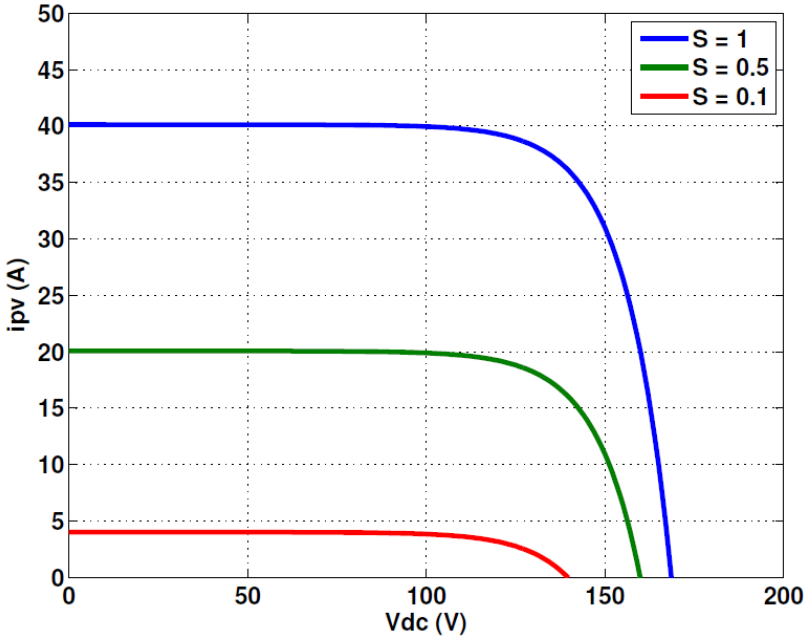

Figure 2.42: PV output current vs. PV terminal voltage

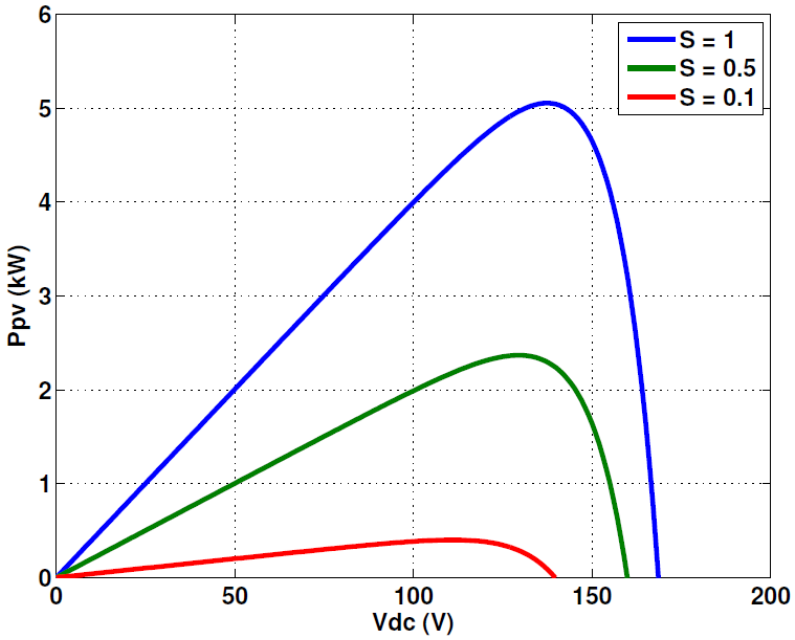

Figure 2.43: PV output power vs. PV terminal voltage

From the Figure 2.43, we can see that the PV panel supplies approximately 5 kW of power at the nominal solar insolation level of 1. As the solar insolation level S drops, the output current and power drop while the output power reaches a maximum at different values of V_{dc} for each level of solar insolation S. A controller designed to track the optimum V_{dc} value is called a Maximum Power Point Tracker (MPPT). The maximum power point for each irradiation level in Figure 2.43 can be found as follows [30].

$$V_{optimal} = \frac{W(ae) - 1}{b} \tag{2.121}$$

where $a = [I_{scr} + K_\theta(T - T_r)]\frac{S}{100I_{rs}} + 1$ and $b = \frac{q}{KTAn_s}$ and W is the Lambert function. The optimal voltage point for the PV array system is shown in Figure 2.44.

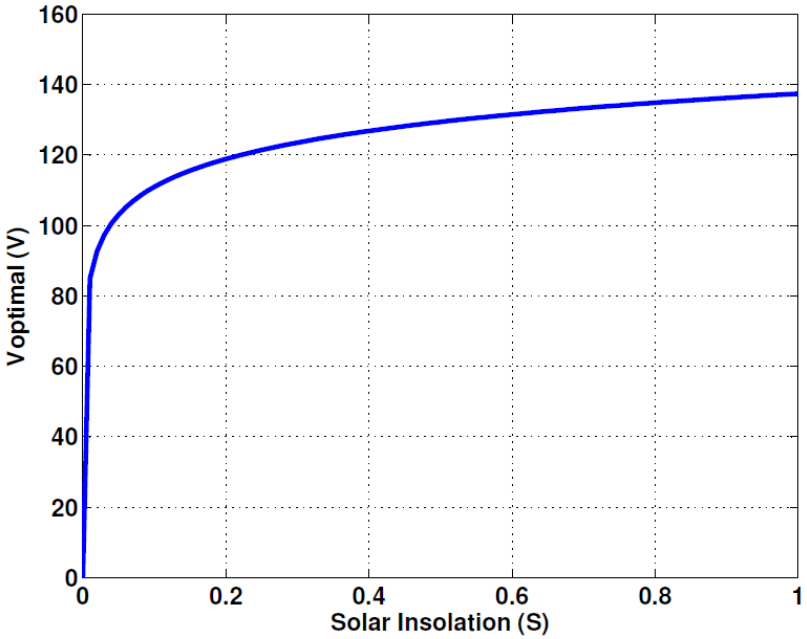

Figure 2.44: Optimal voltage for MPPT

To extract the greatest amount of power from the PV panels, the boost converter should operate by regulating the terminal voltage of the PV panel by tracking the optimal voltage point as plotted in Figure 2.44. From Figure 2.43 the optimal voltage point for $S = 1$ is just under 140 V and on the optimal voltage plot Figure 2.44 the value is just under 140 V, so the plots are in agreement.

Chapter 3

Control Design

3.1 Local Load Inverter

The local load inverter is designed to supply its own load at 120/240 V ac irrespective of the grid connection status. The power flow in this converter is unidirectional from the source voltage across input capacitor C_L to the load that is connected locally to the solid state transformer. In grid connected mode the source voltage of 400 V is controlled by the dual active bridge, in islanded mode the battery bidirectional converter controls the local load inverter source voltage. The control layout is shown in Figure 3.1 with two control loops, an inner capacitor current loop and an outer voltage loop. The control design is exactly the same for the second phase leg of the inverter with the exception that the reference voltage is 180° out of phase. The third phase leg is controlled to give an average output voltage of zero by operating at a fixed 50% duty ratio.

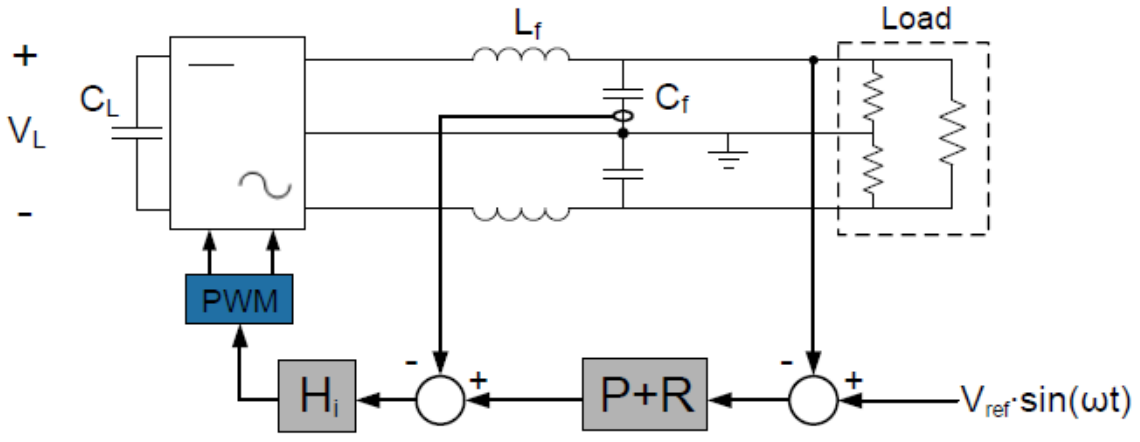

Figure 3.1: Local load inverter control setup

The outer voltage loop uses a proportional plus resonant (P+R) compensator, while the inner loop design is analysed later. The P+R compensator is widely discussed in different literature [31][32] and can provide a high gain at a specified frequency, the ideal P+R and approximate P+R compensator which approximates the ideal integrator using a low-pass filter are given in equations 3.1 and 3.2 respectively where K_p is the proportional gain, K_i is the equivalent integral gain, ω_c is the cutoff frequency of the approximate P+R compensator using the low-pass filter approximation and ω_o is the desired output waveform angular frequency [31].

$$H_{P+R} = K_p + \frac{2K_i s}{s^2 + \omega_o^2} \qquad Ideal \tag{3.1}$$

$$H_{P+R} = K_p + \frac{2K_i \omega_c s}{s^2 + 2\omega_c s + \omega_o^2} \qquad Approximate \tag{3.2}$$

While a PI controller can provide an infinite gain at DC and provide zero error regulation to a DC reference, tracking a sinusoidal signal will have an amplitude and phase error with respect to the reference determined by the loop gain at the reference frequency. Using the P+R compensator, the gain at the reference frequency can be greatly increased and the error is minimized. The P+R compensator is equivalent to the DQ synchronous reference frame control which can also provide a high gain at the reference frame frequency, however for the local load inverter only the P+R compensation is considered. The ideal P+R compensator is plotted in 3.2, while the approximate P+R is plotted in Figure 3.3.

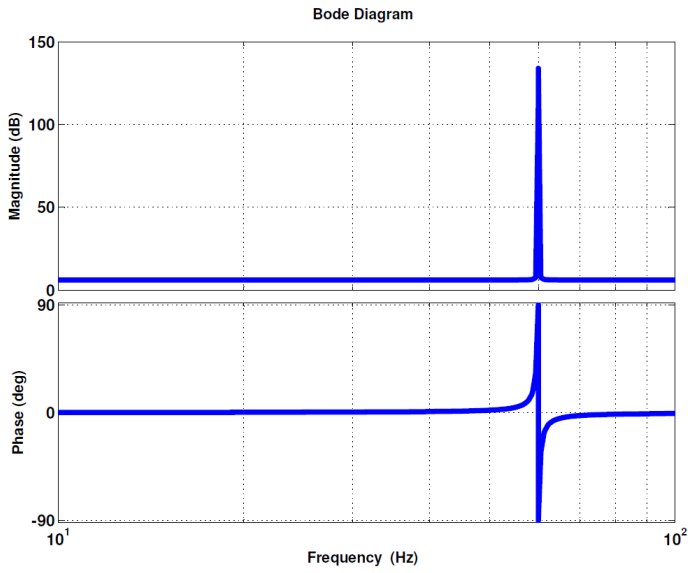

Figure 3.2: Ideal P+R compensator - $K_p = 2$, $K_i = 5$, $\omega_o = 377$

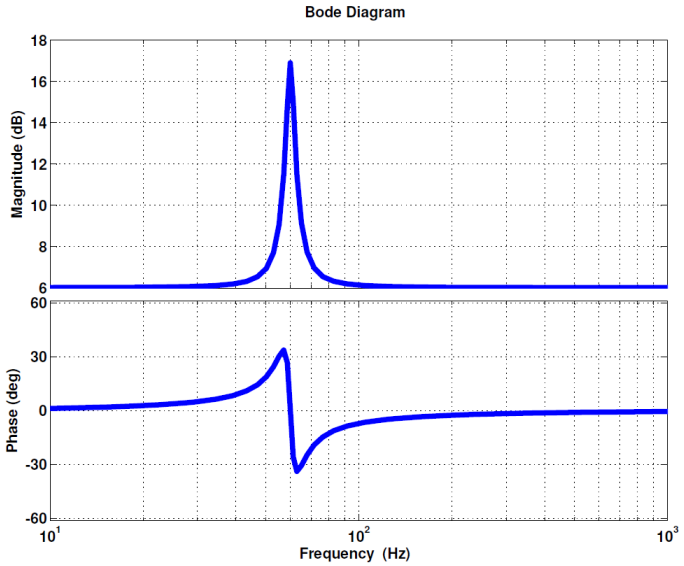

Figure 3.3: Approximate P+R compensator - $K_p = 2$, $K_i = 5$, $\omega_c = 10\ \frac{rad}{s}$, $\omega_o = 377\ \frac{rad}{s}$

The inner current loop is designed first using the control to output transfer function given in Equation 3.3, the parameters for the local load inverter are given in table 3.1

$$\frac{\hat{i}_c}{\hat{d}_a} = V_L \frac{sC_fR}{s^2L_fC_fR + sL_f + R} \tag{3.3}$$

Table 3.1: Local Load Inverter parameters

Parameter	Value	Unit
V_L	400	V
C_L	2	mF
L_f	1	mH
C_f	120	μF
f_s	10	kHz

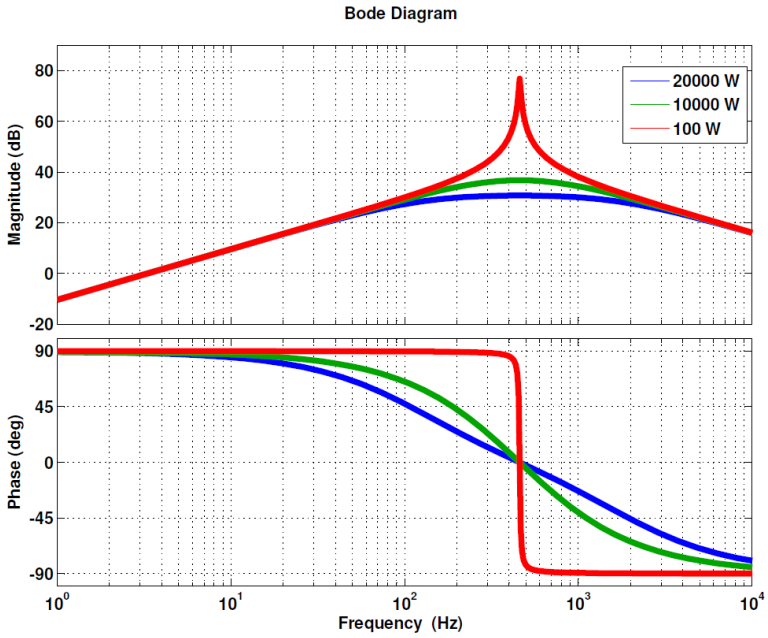

Figure 3.4: Local load inverter $\frac{\hat{i}_c}{\hat{d}_a}$ transfer function under different load conditions

The current loop design is done under the light load condition as shown in Figure 3.4 where the phase shift is the largest.

The PI controller designed is given in Equation 3.4 which gives a crossover frequency of 4.02 kHz, and a phase margin of 60°. The current loop gain with the compensator is shown in Figure 3.5.

$$H_{PI} = K_p + \frac{K_i}{s} = 0.053796 + \frac{791.12}{s} \tag{3.4}$$

In Figure 3.6, the inverter capacitor current using the PI compensator is shown in grey and the reference capacitor current waveform is shown in red. It is clear that there is a magnitude error and phase error between the reference and actual current waveforms, the voltage is uncontrolled without a voltage feedback loop.

The P+R compensator is now designed and the loop gain is shown in Figure 3.7 and the output waveforms are shown in Figure 3.8, the compensator values are given in equation 3.5. The capacitor current follows the reference waveform nicely as it can be seen that the loop gain at 60 Hz is much larger with the P+R compensator. The P+R compensator loop gain has phase margins of 30.9° and 87.9°.

$$H_{P+R} = K_p + \frac{2K_i\omega_c s}{s^2 + 2\omega_c s + \omega_o^2} = 0.05 + \frac{2(10)(2)s}{s^2 + 2(2)s + (2\pi 60)^2} \tag{3.5}$$

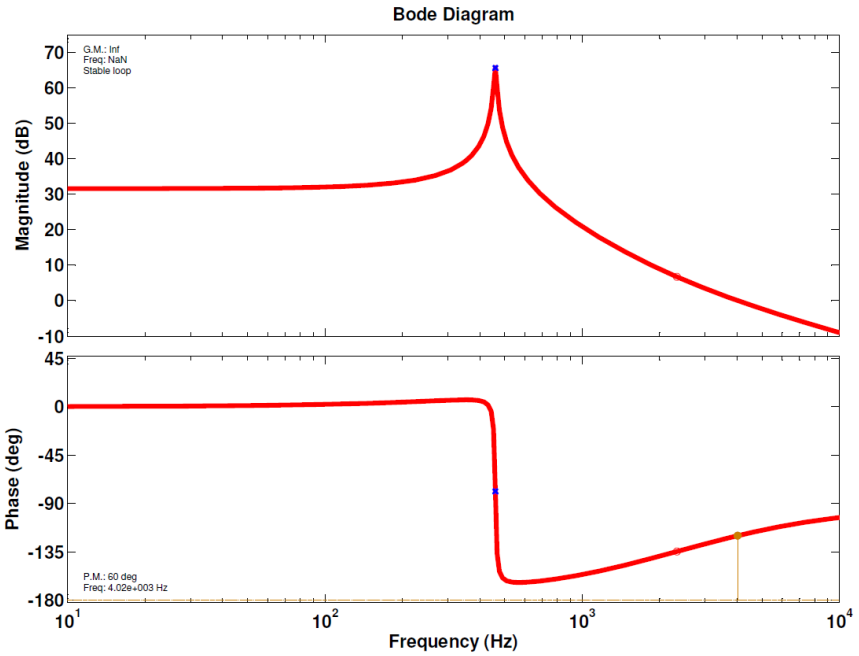

Figure 3.5: Current loop gain with PI compensator

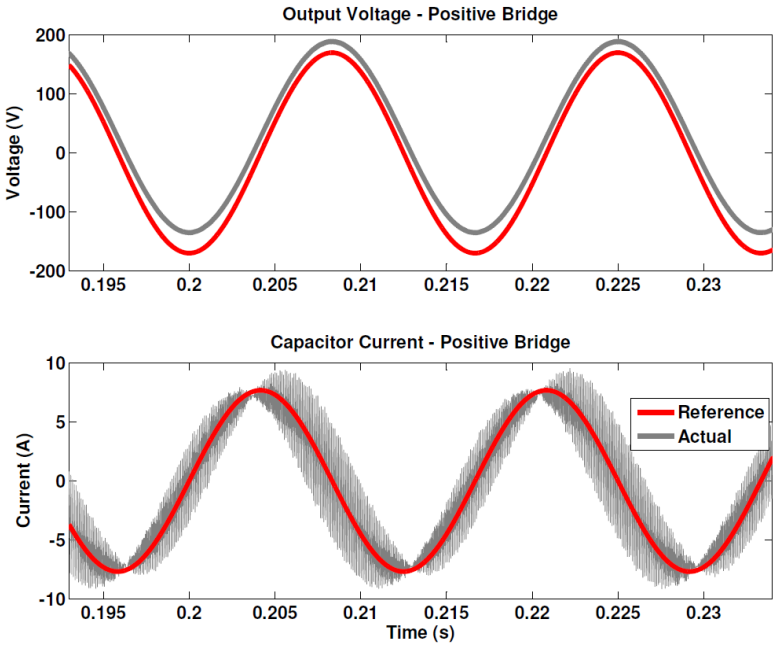

Figure 3.6: Tracking with PI compensator

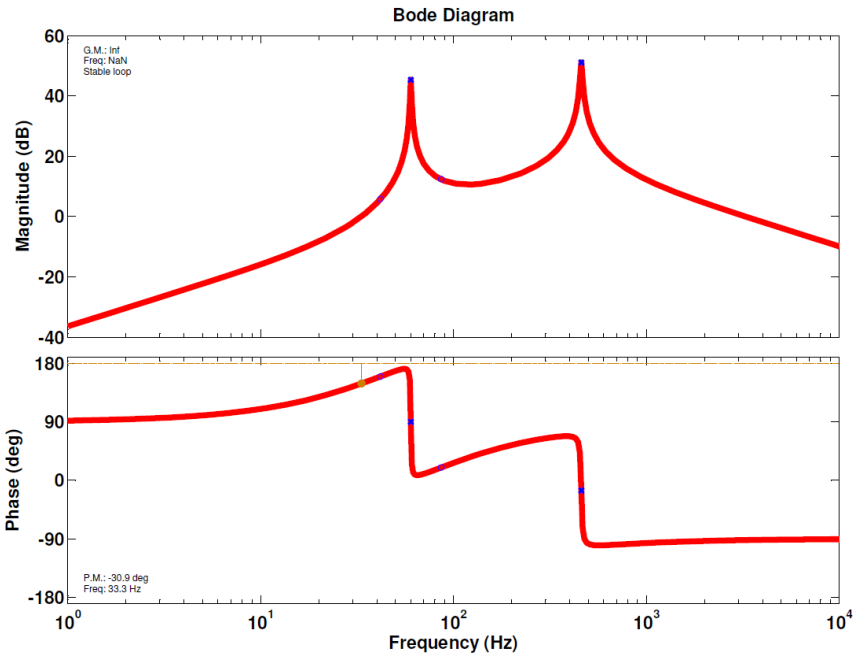

Figure 3.7: Current loop gain with P+R compensator

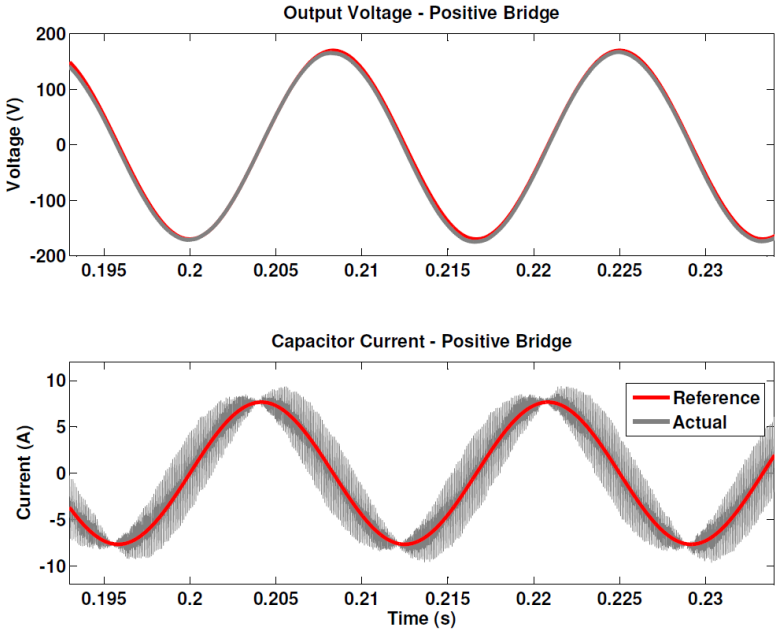

Figure 3.8: Tracking with P+R compensator

The outer voltage loop can now be designed for both the inner current loops previously compared - the PI compensator and the P+R compensator. The loop gain of the outer voltage loop T_v is equal to the forward path gain multiplied by the closed loop gain of the inner current loop, this is shown in Equation 3.6.

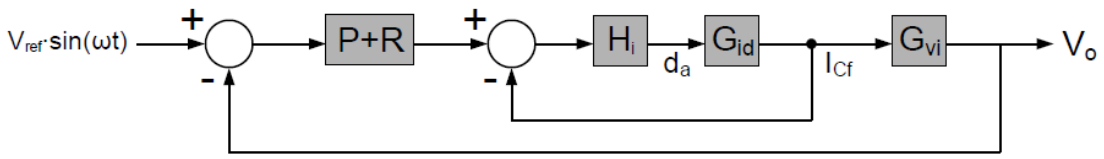

Figure 3.9: Dual feedback loop structure

$$T_v = [P + R]G_{vi}\frac{H_i G_{id}}{1 + H_i G_{id}} \tag{3.6}$$

$$where \quad G_{vi} = \frac{\hat{V}_{aN}}{\hat{i}_c} = V_L \frac{1}{sC_f} \tag{3.7}$$

The closed loop gain T_v in Equation 3.6 is plotted in Figure 3.10 for both conditions of an inner PI current loop and an inner P+R current loop. The loop gain seen by the outer voltage loop at the nominal frequency of 60 Hz is almost the same for both compensators therefore the simpler PI compensator is used.

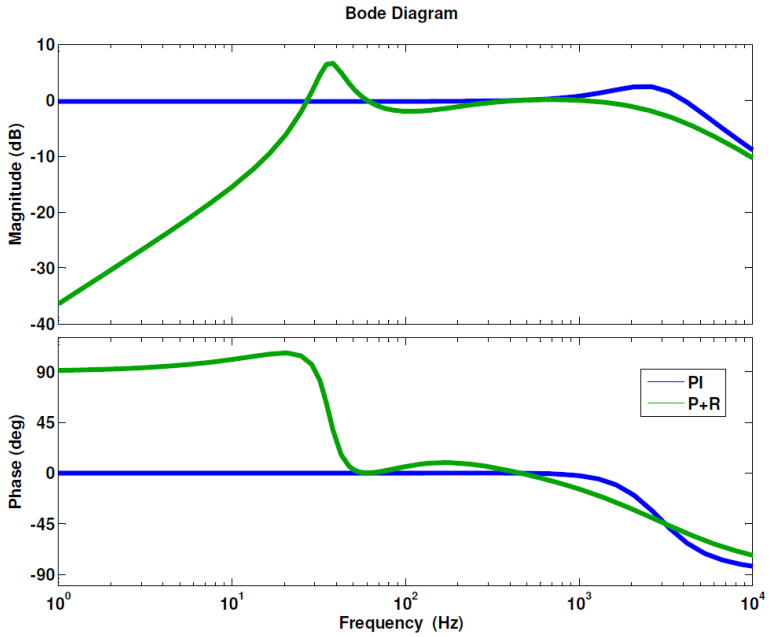

Figure 3.10: Closed loop gain with P+R and PI compensators

The outer voltage loop P+R compensator is designed as given in Equation 3.8. The outer voltage loop gain is shown in Figure 3.11, the loop has a phase margin of 32.3° at a crossover frequency of 3.57 kHz.

$$H_{P+R} = K_p + \frac{2K_i\omega_c s}{s^2 + 2\omega_c s + \omega_o^2} = 0.006 + \frac{2(5)(1)s}{s^2 + 2(1)s + (2\pi 60)^2} \tag{3.8}$$

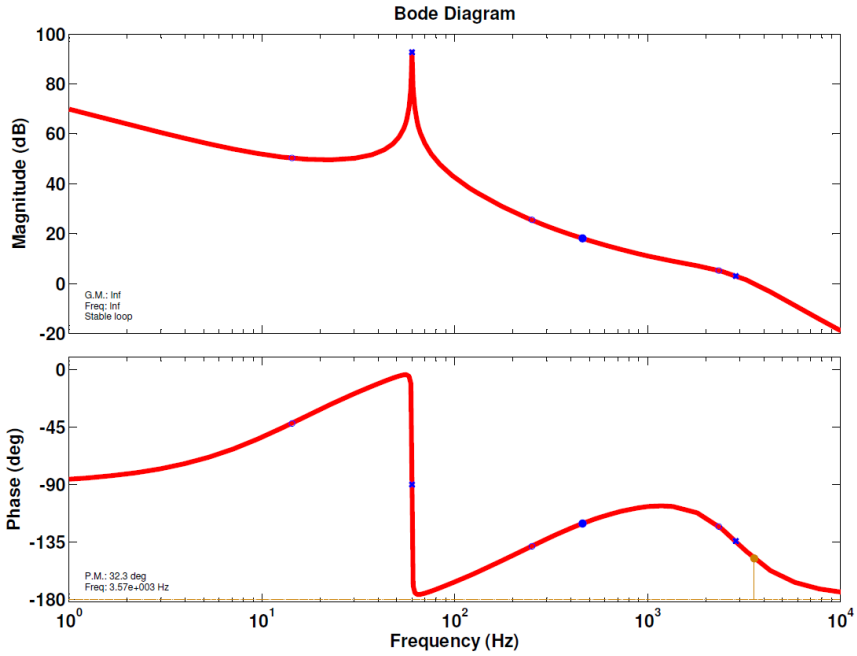

Figure 3.11: Voltage loop gain with P+R compensator

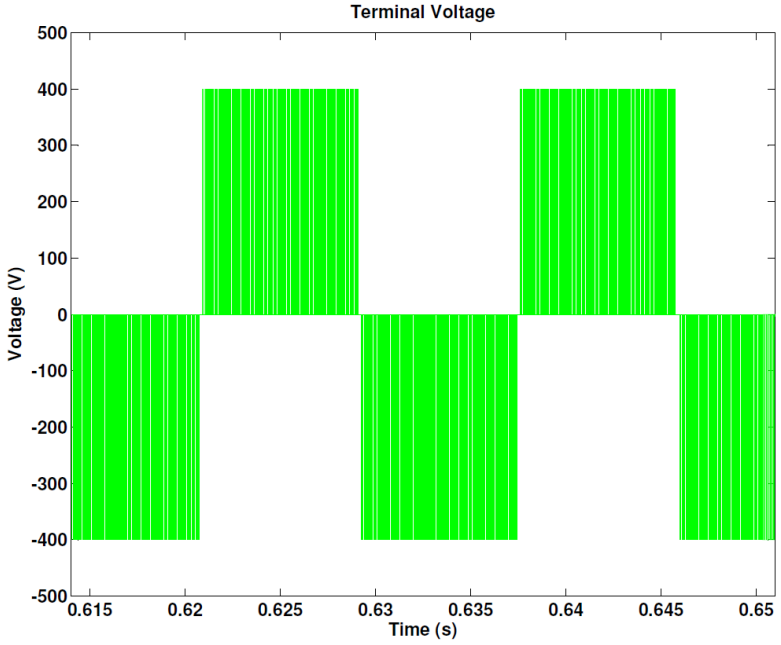

Figure 3.12: Local load inverter terminal voltage

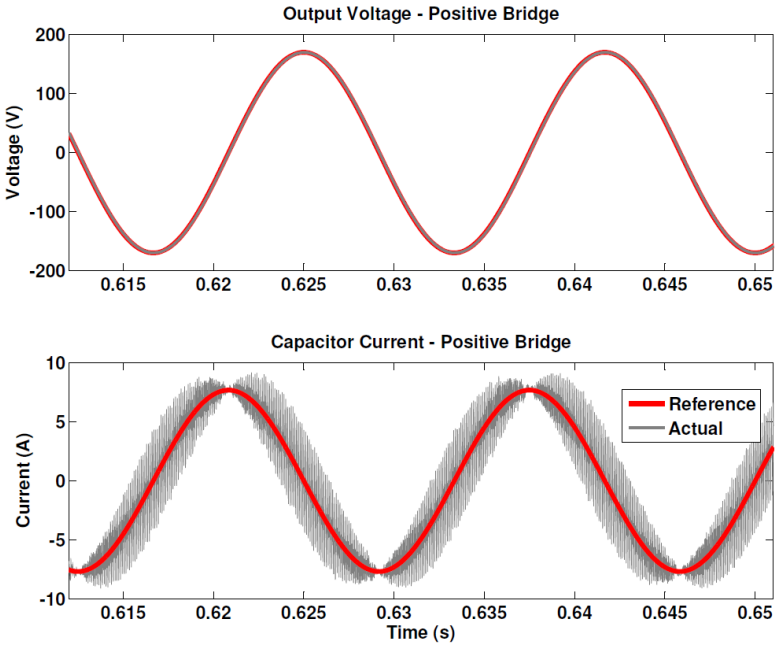

Figure 3.13: Local load inverter output under light load

3.2 Dual Active Bridge Control Design

The DAB is controlled differently depending on if the grid connection is available or not, if it is available the DAB will control the low side DC bus voltage across capacitor C_L, otherwise the DAB should control the high side DC bus voltage across capacitor C_H. The DAB operates by having one H-bridge switch at a fixed frequency while the second H-bridge switches exactly the same but with a time delay introduced. This delay between the bridges can be used to control the DAB output power and average current as previously seen in eqs. (2.25) and (2.26), therefore the time delay can be used as the control variable to regulate the output voltage. The control system layout is shown in Figure 3.14, the green represents the control used during normal grid connected operation while the blue represents the control used during the black start procedure.

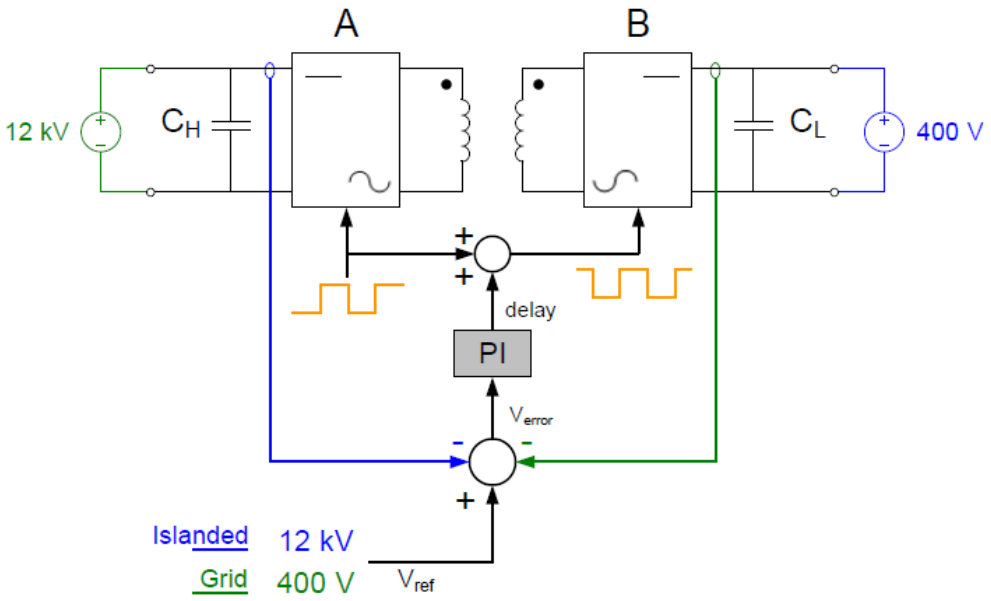

Figure 3.14: DAB Control System

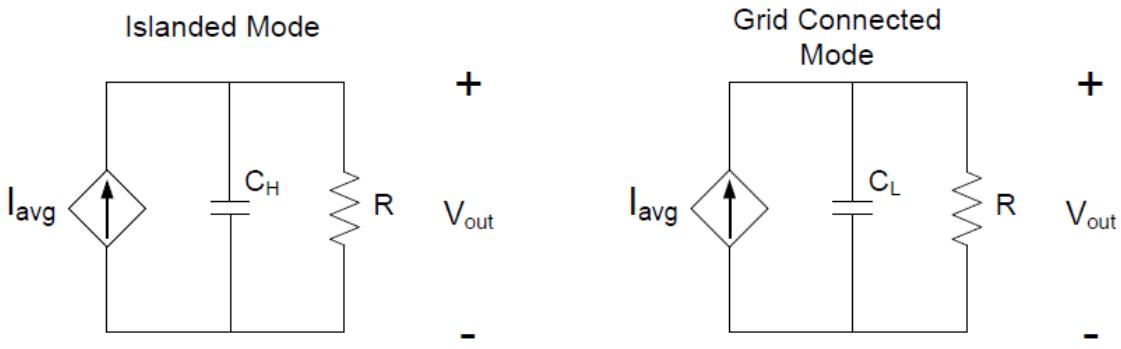

Figure 3.15: DAB average model - Islanded and Grid Connected

In Figure 3.15 the average model of the DAB in grid connected and islanded mode is shown. The difference between the two average models is the output capacitor changes between C_H for islanded mode and C_L for grid connected mode. To control the output capacitor voltage, the small signal transfer function is analysed for the different modes of operation. Equation 3.9 represents the DAB in islanded mode where the low voltage DC bus is controlled by the battery bidirectional converter and is the input voltage for the DAB and the high side DC bus voltage is controlled by the DAB. Likewise, Equation 3.10 represents the DAB is grid connected

mode where the DAB controls the low voltage DC bus and the high voltage DC bus is the input voltage source.

$$\frac{\hat{v}_{out}(s)}{\hat{d}_h(s)} = \frac{V_L T_s}{2L}(1-2D)\frac{\frac{1}{sC_H}+R}{\frac{1}{sC_H}R} \tag{3.9}$$

$$\frac{\hat{v}_{out}(s)}{\hat{d}_h(s)} = \frac{V_H T_s}{2L}(1-2D)\frac{\frac{1}{sC_L}+R}{\frac{1}{sC_L}R} \tag{3.10}$$

Table 3.2: DAB Parameters

Parameter		Value	Unit
V_H		12000	V
V_L		400	V
C_H		50	μF
C_L		2	mF
L		250	μH
T_s		$\frac{1}{3000}$	sec
R	20 kW Island	7200	Ω
R	100 W Island	1440	$k\Omega$
R	20 kW Grid Conn.	8	Ω
R	100 W Grid Conn.	1.6	$k\Omega$
D	20 kW	0.25	-
D	100 W	0.000938	-

With the parameters in table 3.2, the transfer functions for the different operating modes of the DAB are plotted and compared. The transfer functions are plotted in Figure 3.16

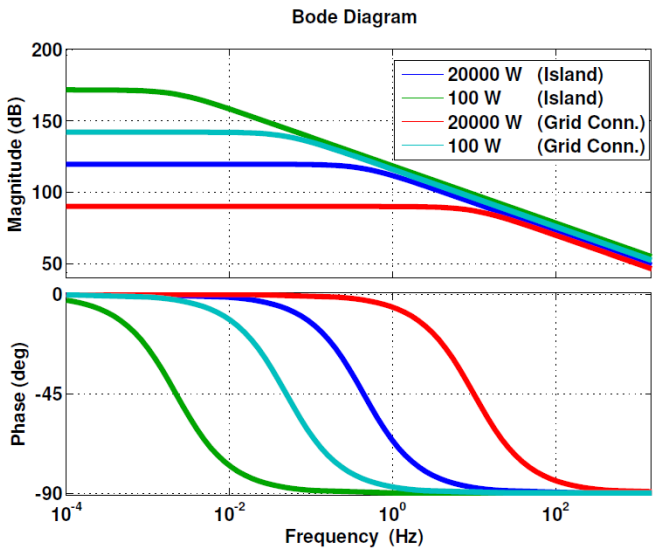

Figure 3.16: DAB $\frac{\hat{v}_{out}(s)}{\hat{d}_h(s)}$ transfer functions

The transfer functions for islanded and grid connected modes for light and heavy loads are plotted, it is clear that the DAB is stable across all the operating conditions, but the light load islanded condition shown in green has the most phase lag and will be used to design the DAB controller. The controller designed is a proportional plus integral type (PI), and the general form is shown below.

$$G_c = K_p + \frac{K_i}{s} = 0.000122 + \frac{0.081015}{s} \tag{3.11}$$

The controller was designed to provide a phase margin of 50° and a crossover frequency of 130 Hz, the loop gain with the designed compensator is shown in Figure 3.17

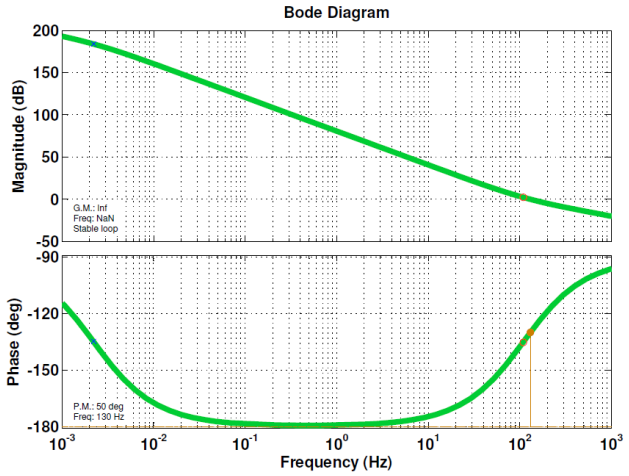

Figure 3.17: $\frac{\hat{v}_{out}(s)}{\hat{d}_h(s)}$ loop gain with compensator

3.3 Grid Tied Rectifier/Black Start Inverter Control Design

The grid tied rectifier interfaces with the distribution grid while the black start inverter must parallel itself with other solid state transformers to supply load throughout the microgrid during the restoration procedure.

3.3.1 Grid Tied Rectifier Control

The DQ model for the grid tied rectifier was previously found, the control design can be designed based on the small signal model of Equation 2.76. The control design for the rectifier is shown in Figure 3.18 consisting of two main control loops, one for the D axis and one for the Q axis. For the D axis control the desired DC bus voltage $V_{Href} = 12kV$ is subtracted from the measured DC bus voltage, the error drives the outer PI controller which gives the i_{dref} reference current. An inner control loop also uses a PI controller to regulate the D axis duty cycle d_d based on the i_d current error, a decoupling term of $\omega L i_q$ is subtracted from the output. For the Q channel the current reference i_q is set to zero as previously discussed and is regulated using a PI controller. A decoupling term is also used in the Q channel of $\omega L i_d$. The measured values of i_d, i_q are obtained by transforming the inductor current ($i_g = i_\alpha$) and a quarter cycle delayed inductor current ($i_g \times e^{-sT/4} = i_\beta$) to the DQ frame, the same can be applied to the grid voltage to obtain the V_d, V_q components. Again, the delay state variables can be obtained through differentiation, or by applying a time delay.

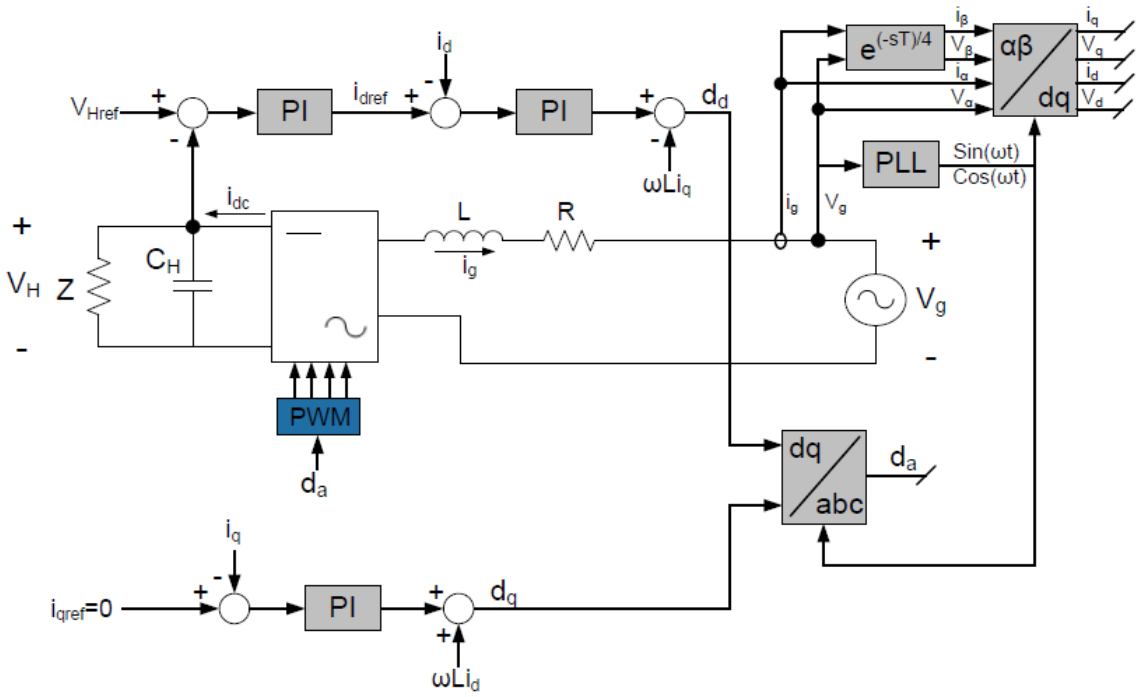

Figure 3.18: Rectifier control layout

3.3.2 Black Start Inverter Control

In the black start procedure the solid state transformers with black start resources such as battery energy storage systems, flywheel energy storage, microturbines, wind turbines and PV panels act in parallel with non black start solid state transformers to supply the total system load as previously mentioned and illustrated in Figure 1.10. Black start procedures have been previously studied in [33], [34] and [35]. In [34] two control strategies for the inverters are identified as PQ controlled where the inverter supplies active and reactive power based on a given set point, or controlled as voltage source inverters (VSI) where the terminal voltage and frequency of the inverter are controlled to supply the load therefore the load defines the output power. The PQ type control can be used when a voltage reference is available such as the distribution grid, however during the black start procedure the voltage reference must be generated by one of the solid state transformers, this eliminates the possibility of using a PQ type control for every inverter in the microgrid. The two options available are to have a combination of PQ and VSI type inverters in the system where the VSI's control the voltage and frequency, this imposes a limit of at least one inverter must be controlled as a VSI in the microgrid. If more than one VSI is operated in the microgrid than a droop type control must additionally be implemented for parallel operation. In [34] these two control strategies are the

Single Master Operation where one VSI is used during the black start procedure and all others are operated in PQ mode, and the Multi Master Operation where there are multiple VSI's along with PQ controlled inverters. A microgrid with multiple VSI's controlling the voltage and frequency is proposed for the black start procedure of the solid state transformer. The multiple VSI control strategy can provide a more robust system because if a failure occurs on one solid state transformers the microgrid voltage and frequency will continue to be regulated.

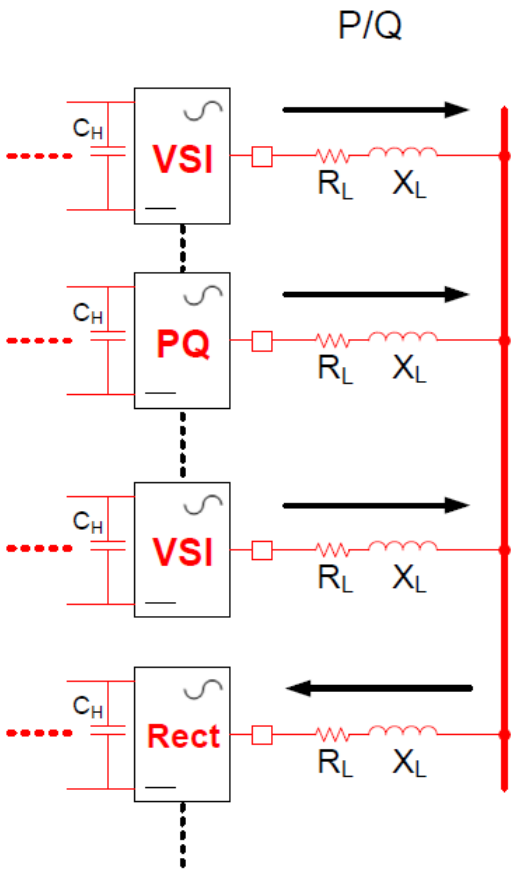

Figure 3.19: Control topology for microgrid black start

The solid state transformer block diagram is shown in Figure 3.19, the solid state transformers are paralleled with the VSI solid state transformers controlling the voltage and frequency. Solid state transformers without any energy storage act as loads for the solid state transformers with energy storage and is labeled as rect (rectifier) in the figure. Only the VSI control design is considered here, the PQ control is dependant on the VSI to establish the reference voltage making it more important to the system operation.

Droop control is commonly used in the control of synchronous generators where a mismatch in generation and load causes a change in output frequency due to a loss or gain of inertia created in the generator. The generator droop speed governor will reduce the reference speed as the load increases, therefore multiple generators on a system will share the load power change at a new system frequency in a stable manner [36]. For a given increase in load power ΔP_L each generator will slow down as the energy stored in the inertia of the rotor starts to transfer to the load, the droop governor responds by increasing the output power of each generator in proportion to the droop characteristic causing the system frequency to settle at a new lower value. The nominal system frequency can be restored through the AGC (Area Generation Control) system by increasing generator load reference setpoints, this will shift the droop governor characteristic such that the current load output operating point is at the nominal system frequency. The general droop concept is illustrated in Figure 3.20.

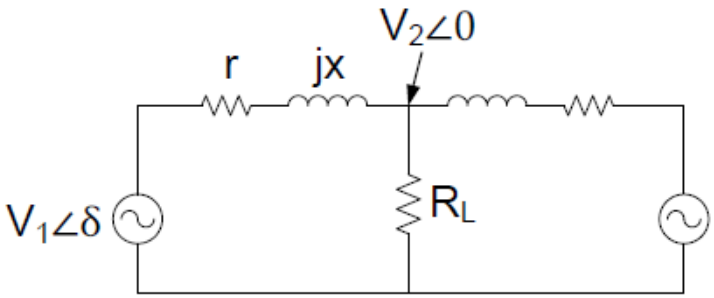

Figure 3.20: Droop control equivalent circuit

From Figure 3.20, the power can be derived as $S = VI^*$ and assuming that the angle difference between the generator and the load is small ($\delta_1 - \delta_2 \approx \delta$) then $sin(\delta) = \delta$ and $cos(\delta) = 1$ then:

$$P \approx \frac{V_1 V_2 r + V_1 V_2 x\delta - V_2^2 r}{r^2 + x^2} \tag{3.12}$$

$$Q \approx \frac{V_1 V_2 x - V_1 V_2 r\delta - V_2^2 x}{r^2 + x^2} \tag{3.13}$$

Assuming only an inductive line impedance ($r = 0$), then eqs. (3.12) and (3.13) can be simplified as given below.

$$P \approx \frac{V_1 V_2}{x}\delta \tag{3.14}$$

$$Q \approx \frac{(V_1 - V_2)V_2}{x} \tag{3.15}$$

Therefore the real power flow is mainly determined by the angle δ while the reactive power flow is mainly determined by the voltage difference $V_1 - V_2$. This implies that a P-ω droop can be used for real power sharing and a Q-V droop for reactive power sharing. This method has also been extended to inverters with much research being done on inverters controlled in droop mode [37][38][39]. The general droop characteristics are shown as follows in Figure 3.21 where the axes are inverter real power output (P) versus output frequency (ω) and reactive power output (Q) versus output voltage (V). For the P-ω droop characteristic P_{max} is the maximum real power output of the inverter, P^* is the real power output in grid connected mode, ω_{min} is the minimum allowed frequency and ω^* is the grid connected frequency of the inverter. Similarly for the Q-V droop Q_{max} is the maximum reactive power output, Q^* is the dispatched reactive power, V_{min} is the minimum allowed voltage and V^* is the nominal grid connected voltage. The droop slope is given by m_P and m_Q and are defined in eqs. (3.17) and (3.19).

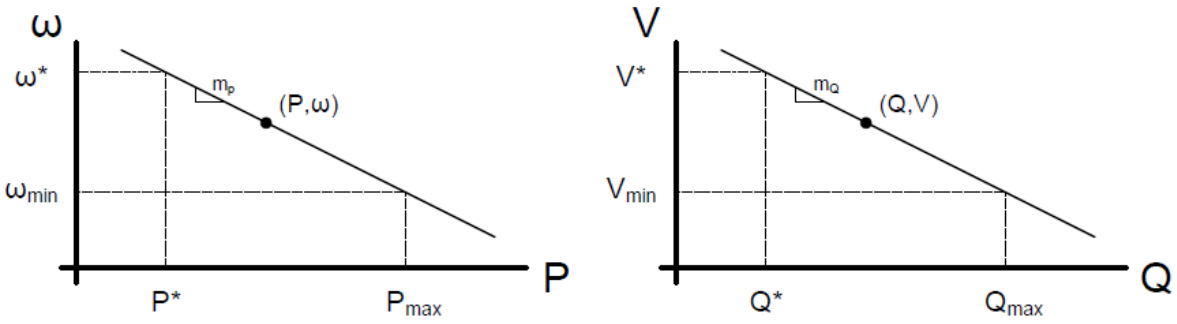

Figure 3.21: P-ω and Q-V droops

$$\omega = \omega^* - m_P(P^* - P) \tag{3.16}$$

$$m_P = \frac{\omega^* - \omega_{min}}{P^* - P_{max}} \tag{3.17}$$

$$V = V^* - m_Q(Q^* - Q) \tag{3.18}$$

$$m_Q = \frac{V^* - V_{min}}{Q^* - Q_{max}} \tag{3.19}$$

In eqs. (3.16) and (3.18) P* and Q* are set to zero in islanded mode, however if the inverters operate in grid connected mode with droop control the P and Q reference values must be set as this allows for power to be delivered to a constant power source such as the utility grid. For the droop control to be implemented it is required to measure the active and reactive power output of the inverters and create a running average over one fundamental frequency cycle often implemented using a low-pass filter. The outer droop control loop is shown in Figure 3.22, the output reference voltage of the droop control loop is the input reference to the inner voltage and current control loops of the inverter.

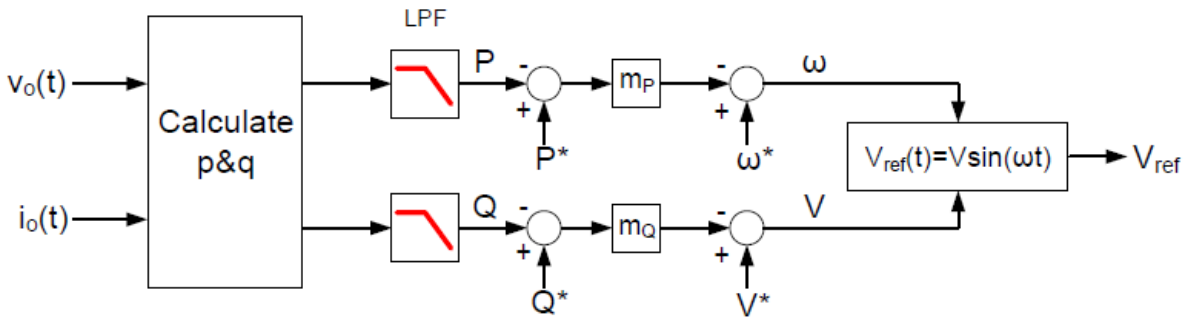

Figure 3.22: Outer droop control loop

One previous assumption for the droop controlled inverter is that the line impedance between the inverters to the load is purely inductive which is a good assumption for transmission lines, however low voltage distribution lines in a microgrid often consist of a non-negligible resistance or may even be mainly resistive. In the case of a non-negligible resistance there will be a coupling between the real and reactive power and they cannot be controlled in an isolated manner previously seen using the voltage magnitude difference and phase (frequency). For a mainly resistive line another approach is adopted by using a P-V droop and Q-ω droop. This coupling between the real and reactive power will be further discussed in a later section. An obvious drawback with the droop method is the loss of frequency accuracy for real power sharing and voltage accuracy for reactive power sharing.

The droop controlled inverter requires another layer of control to track the reference voltage given by the droop control loop, in this case we will consider both voltage and current loops. There are multiple positions which the voltage and current can be measured with the LCL output filter, the voltage sensor is usually placed on the output of the filter because the grid voltage measurement will be necessary for a synchronous reference frame transformation, the current sensor will also be placed on the output of the filter for measurement of the grid side

inductor current. Figure 3.23 shows the control block diagram of the black start inverter.

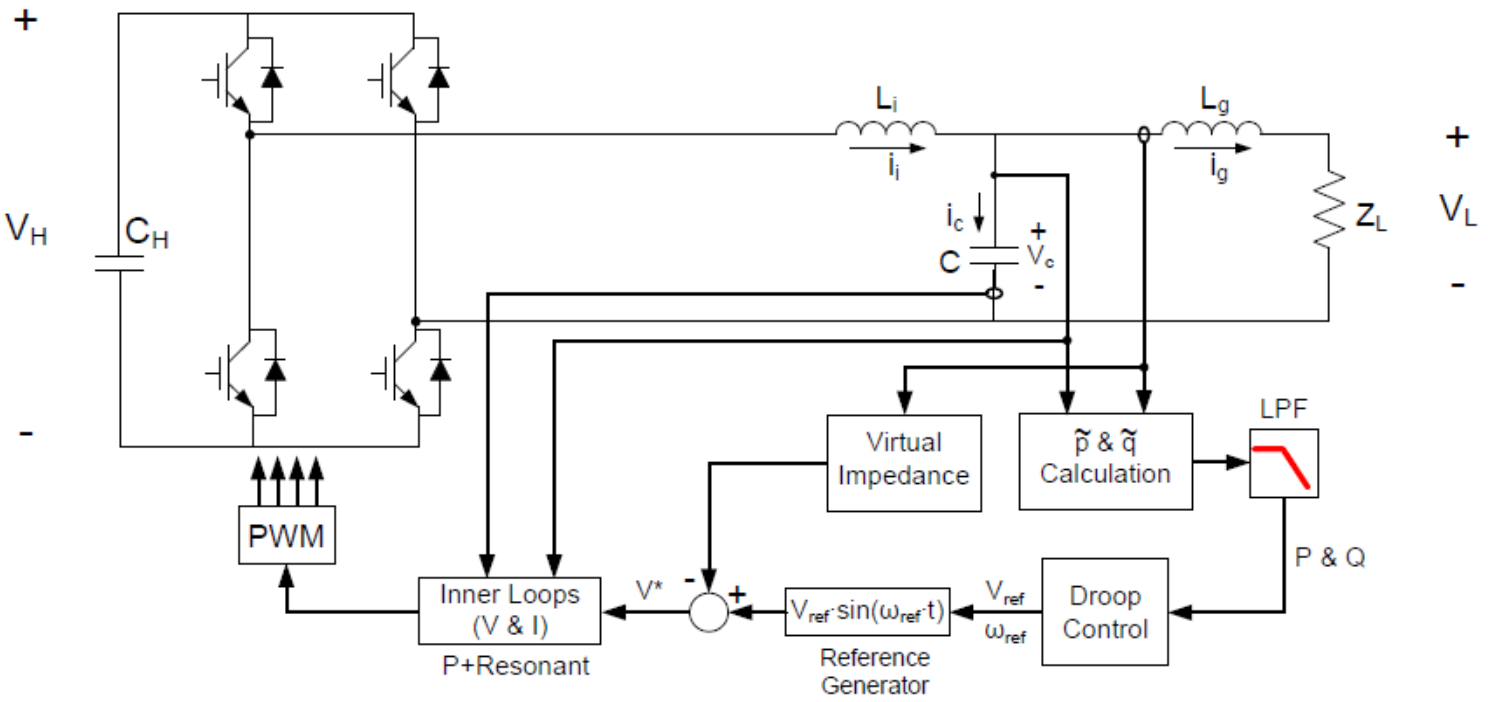

Figure 3.23: Black start inverter control

In grid connected mode during normal operation the solid state transformer rectifies the grid voltage to supply its load, the battery bank charges from a power source such as a PV array. It is possible that PV power could be supplied to the grid, although this mode is not simulated in this work, the current controlled inverter is investigated. The current control is required because the grid dictates the voltage therefore the power supplied to the grid by the inverter can be controlled through a current controlled design.

Figure 3.24 shows the inverter system with the output current i_{Lg} feedback, the transfer function of the system without damping resistor is

$$\frac{i_{Lg}(s)}{u(s)} = \frac{G_{pwm}(s)}{L_i L_g C s^3 + (L_g + L_i)s} \tag{3.20}$$

The bode plot is shown in Figure 3.26, the LCL filter has a resonant peak and will cause stability problems in the system. By adding an additional inner feedback loop of the capacitor current i_C, the resonant peak can be damped dynamically as shown, the control design for this case is shown in Figure 3.25 where $H_I(s)$ is the outer loop compensation and K is the gain of the inner loop compensation and the pwm gain $G_{pwm}(s)$. Figure 3.26 compares the responses of the different control designs including the use of the damping resistor $R_d = 1.6\ \Omega$ in series with the filter capacitor as previously designed. It is clear that the current control utilizing the dual loop design with an inner capacitor current feedback loop and outer grid current loop along with a damping resistor allows for the most simple control design by providing a good phase margin. However, with compensation sufficient stability margins can be obtained with the inner capacitor current feedback loop without the losses associated with the damping resistor, this method is used.

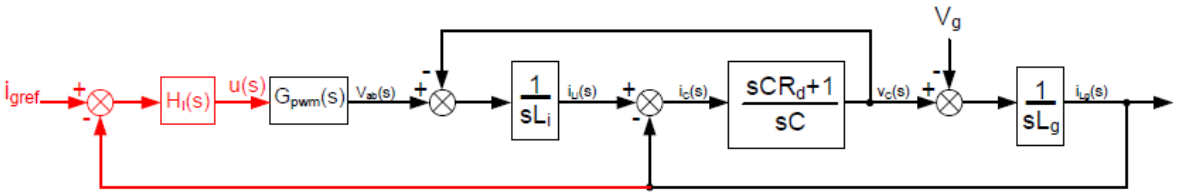

Figure 3.24: Grid connected current control with i_{Lg} feedback

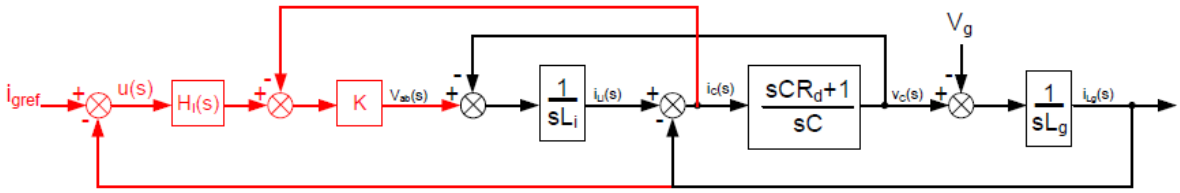

Figure 3.25: Grid connected current control with i_{Lg} outer and i_C inner feedback loops

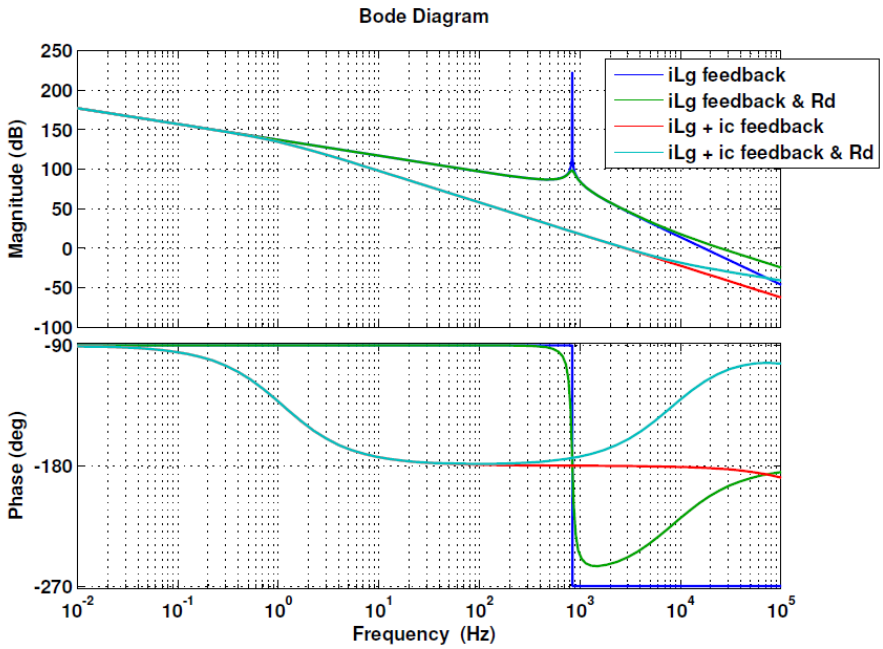

Figure 3.26: Loop gain comparison for different current control topologies

The grid connected inverter control is designed using the dual loop feedback design without damping resistor. Because of the complexity of the plant, the compensators are designed in Matlab. The inner loop is designed with a simple proportional compensator $K = 0.002$, the outer loop gain is designed in Matlab by closing the inner loop with a proportional compensator and opening the outer loop for the outer compensator design. The system is shown in Figure 3.27, the input and output of the loop gain is indicated by the arrows while the 'x' marks the opened loop.

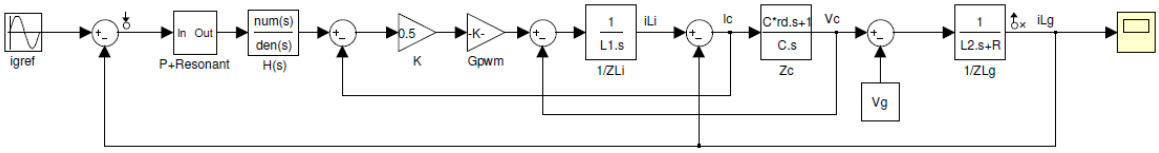

Figure 3.27: Simulink inverter current control system

The compensated loop gain for the inverter is plotted in Figure 3.28 and the compensator is given in Equation 3.22, the phase margin is 16°. A proportional resonant compensator is also added in the outer loop with the following parameters: $K_p = 5$, $K_i = 50$, $\omega_c = 2$, $w_o = 2\pi 60$.

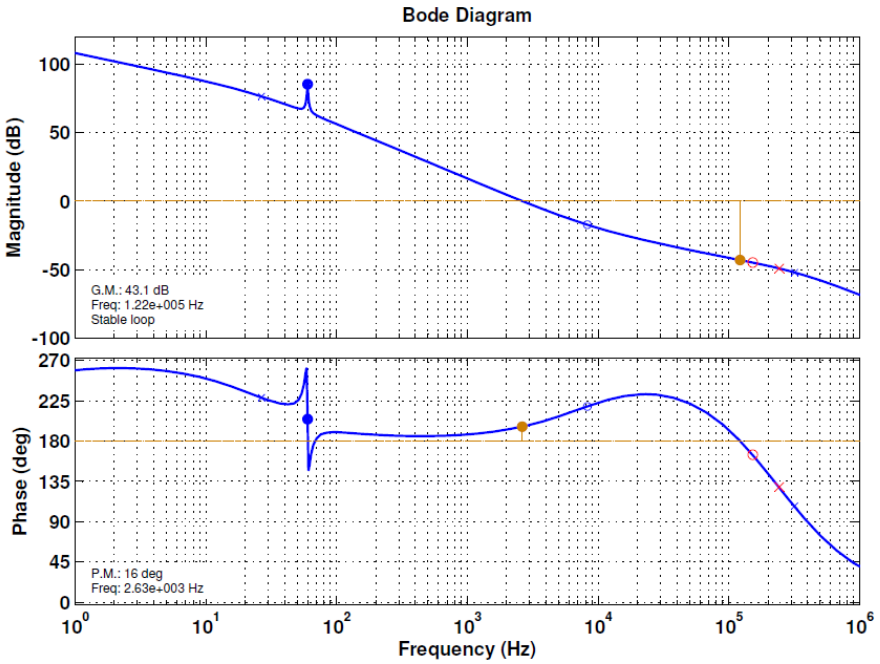

Figure 3.28: Compensated inverter current control loop gain

$$H_{P+R} = K_p + \frac{2K_i\omega_c s}{s^2 + 2\omega_c s + \omega_o^2} \tag{3.21}$$

$$H_I(s) = 0.16941\frac{(1 - 1(10^{-6})s)(1 + 1s)}{s(1 + 6.5(10^{-7})s)} \tag{3.22}$$

The critical operating mode for this stage is during the black start operation of the solid

state transformer which is to operate in an standalone voltage controlled mode. The control design for this mode is designed based on the model previously given under lightly loaded conditions. The control design uses the inner capacitor current feedback loop with an outer capacitor voltage loop to regulate the load voltage as shown in Figure 3.29.

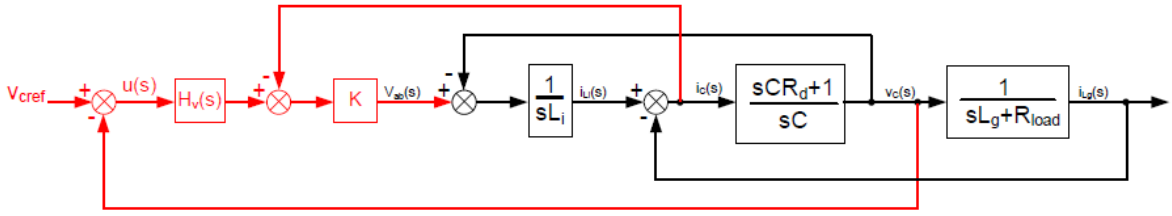

Figure 3.29: Black start inverter operation control

A proportional gain is again used for the inner current loop compensator and is set at a value of $K = 0.002$ and a Proportional + Resonant compensator is used in the outer voltage loop with the following parameters: $K_p = 2$, $K_i = 250$, $\omega_c = 2$, $w_o = 2\pi 60$. A compensator is added after the proportional resonant compensator to achieve a phase margin of 21.4° and crossover frequency of 909 Hz and is given as: $\frac{0.018249s+165.9}{s}$. The inner compensated current loop gain is shown in Figure 3.30 and the outer compensated voltage loop gain is shown in Figure 3.32.

$$\frac{i_c}{u_i(s)} = \frac{CKL_gs^2 + CKR_{load}s}{CL_gL_is^3 + CL_iR_{load}s^2 + (L_i + L_g)s + R_{load}} \tag{3.23}$$

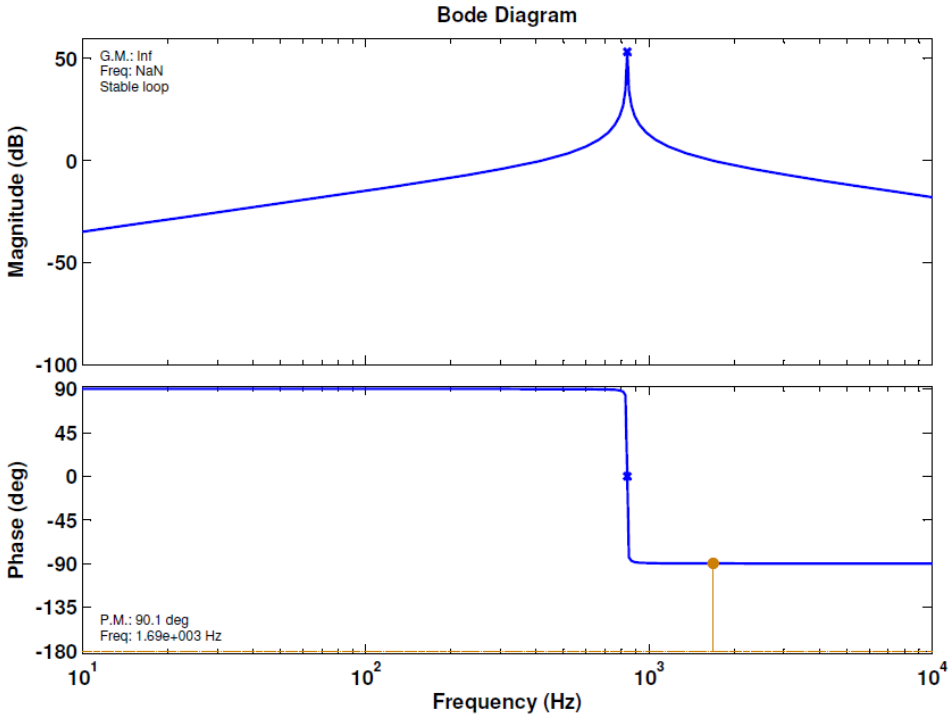

Figure 3.30: Compensated inverter current loop gain

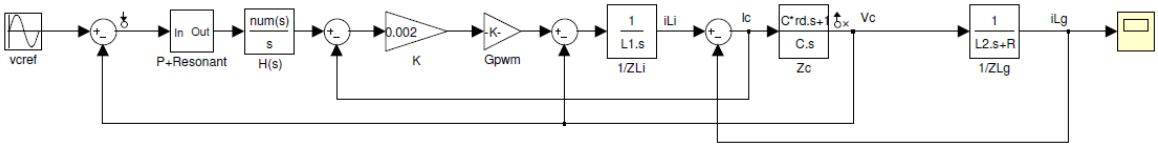

Figure 3.31: Simulink inverter voltage control system

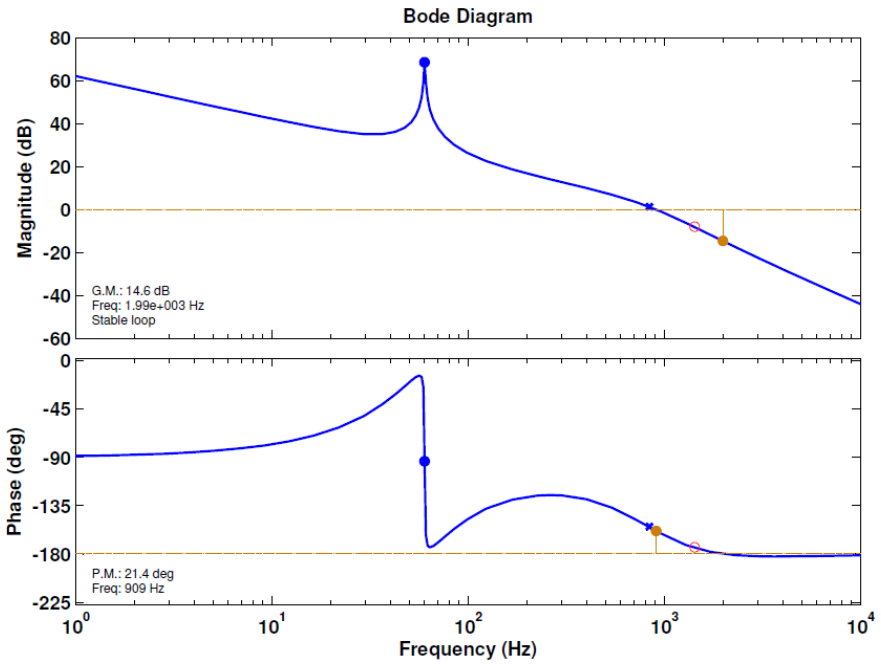

Figure 3.32: Compensated inverter voltage loop gain

The black start control design is tested through simulation in Matlab Simulink shown in Figure 3.33. The simulation includes a line impedance indicated as *Lline* and *Rline* and a load change at 0.1 seconds from a light load of 100 W to a heavy load of 20 kW. The output voltage is regulated at 700 V rms. The capacitor voltage, load current, and load voltage waveforms are shown in Figure 3.34, the load change is visible at 0.1 seconds as the load peak current jumps from approximately 0.02 A to 40.4 A, the capacitor voltage is regulated as required.

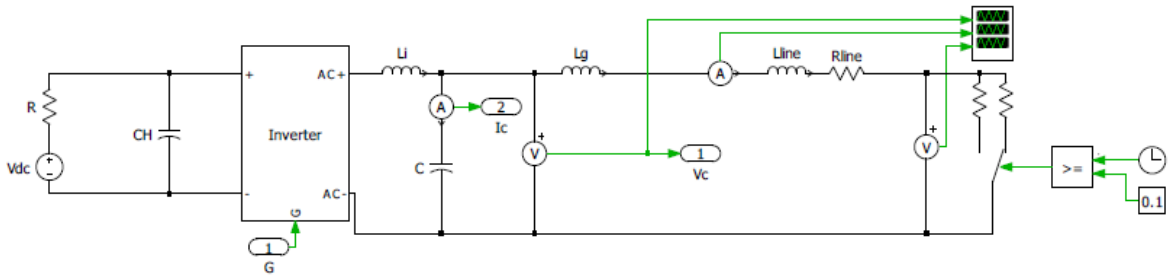

Figure 3.33: Black start inverter system simulation

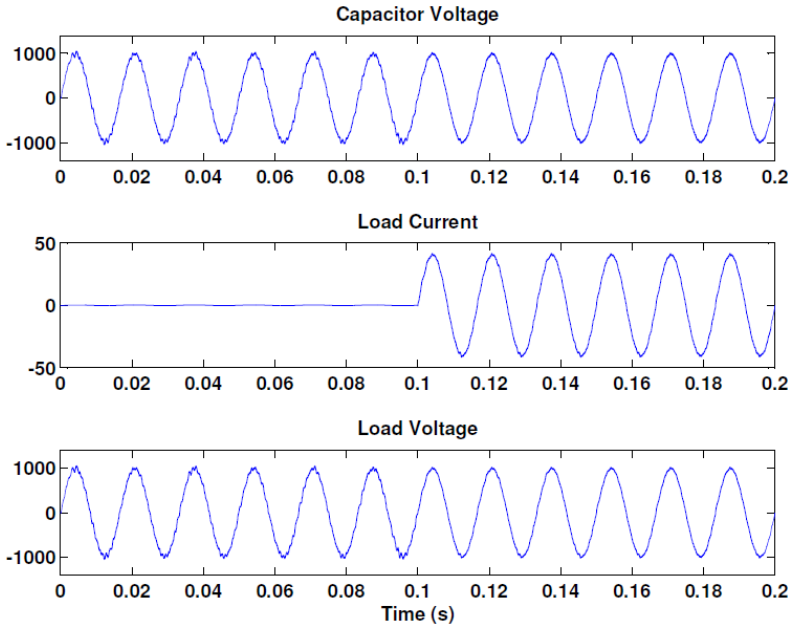

Figure 3.34: Black start inverter system waveforms

The parameters for the droop control are given in the table 3.3.

Table 3.3: System parameters

Parameter	Value	Unit
Nominal grid voltage (rms)	700	V
Minimum grid voltage (rms)	680	V
Nominal grid frequency	60	Hz
Minimum grid frequency	59	Hz
Inverter switching frequency f_s	6	kHz
Line resistance	0.1	Ω
Line inductance	1	μH
Virtual inductance	3	mH
Inverter max power	30	kVA
Inverter nominal power	20	kVA

As previously discussed the droop control allows the inverters to share the load power requirement in a stable manner, however the droop control is based on an inductive line

impedance. Resistance in the line will lead to a coupling between the real and reactive power of the inverters, to solve this problem a virtual impedance control loop is added to the droop control shown in Figure 3.23. The virtual impedance designed is an inductance of 3 mH, this helps to decouple the real and reactive power by imposing an inductive output impedance of the solid state transformer which in turn helps to equalize the output impedances and reduce any mismatches caused by differing line impedances. [40]

Rather than differentiating the line current to obtain the virtual inductance as $L_V \frac{di_L}{dt}$ and possibly amplifying noise through the differentiation process the virtual impedance is calculated from the grid current based on the nominal frequency as $sL_V = j\omega L_V$ where $\omega = 60Hz$. [39]

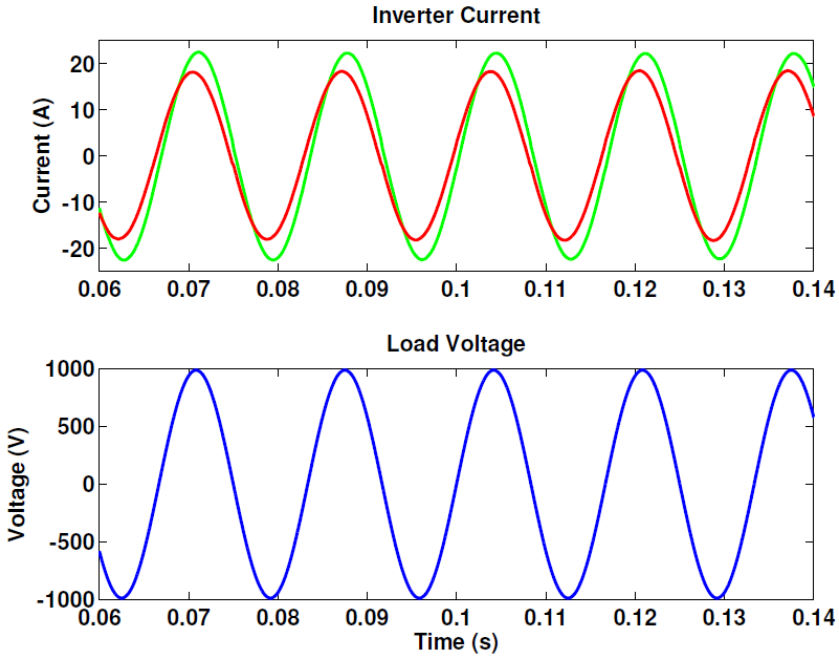

Figure 3.35: Parallel solid state transformer inverter output without virtual impedance

Figure 3.35 shows the output current of the two parallel inverters in droop control without the use of the virtual inductor, it is clear that the output currents are unequal in magnitude and phase.

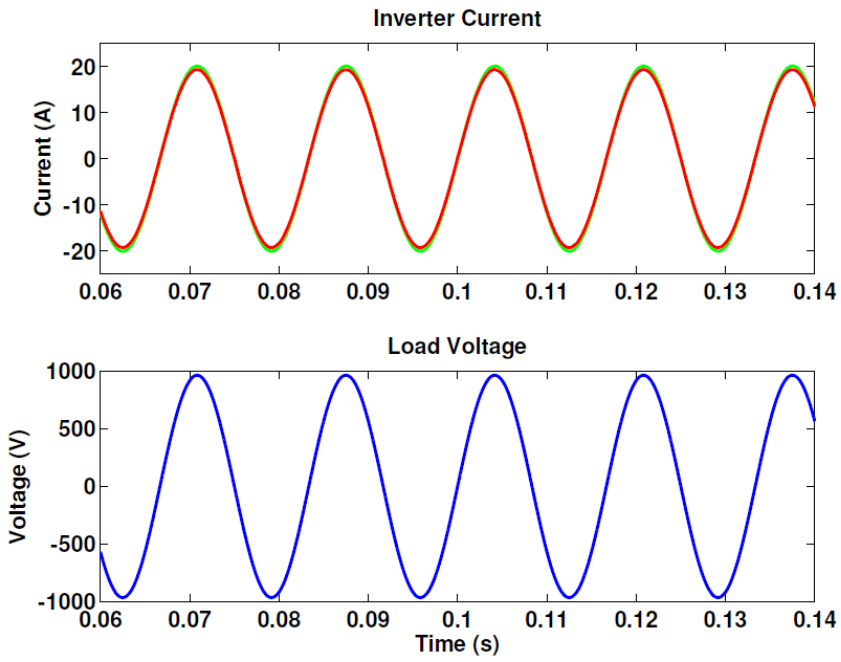

Figure 3.36: Parallel solid state transformer inverter output with virtual impedance

The output current sharing between the inverters is improved by adding the virtual inductor as shown in Figure 3.36. The output current of each inverter is shared much more evenly between the two, a small error still exists but it is a large improvement in the power sharing capability of the inverters.

3.4 Battery DC/DC Bidirectional Converter Control Design

The two modes considered for the battery DC/DC bidirectional converter are the grid connected battery charging mode and the islanded battery discharging mode. In the grid connected battery charging mode the battery is kept fully charged, the bidirectional converter charges the battery using the power supplied by the DRER and the grid if the DRER cannot supply enough power then the additional power drawn by the battery charging current is supplied from the grid. When the grid connection is lost and the solid state transformer is operating as a black start resource, the bidirectional converter uses the battery and DRER as its power source for restoration.

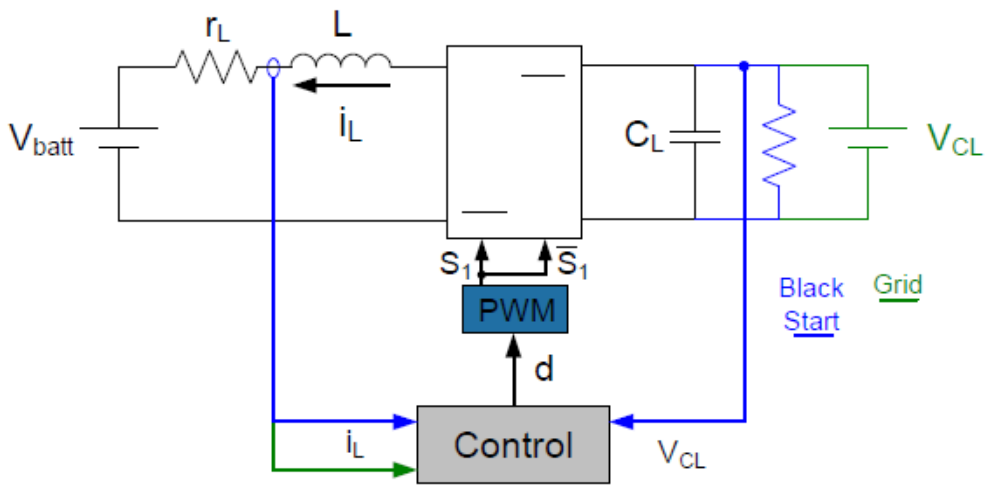

Figure 3.37: Control layout for bidirectional converter

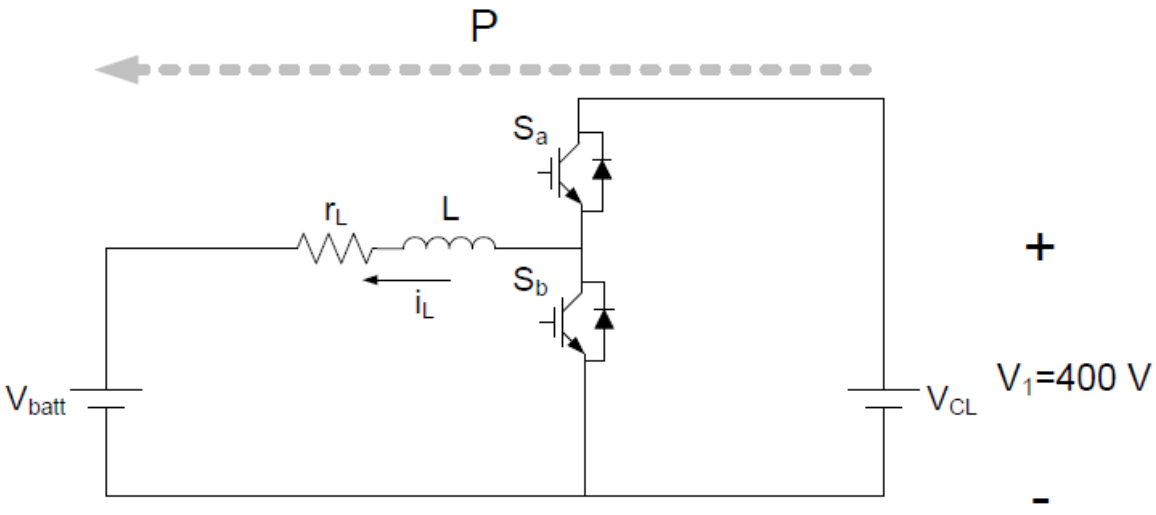

Figure 3.38: Grid connected equivalent circuit

The black start control design is tested through simulation in Matlab Simulink shown in Figure 3.33. The simulation includes a line impedance indicated as *Lline* and *Rline* and a load change at 0.1 seconds from a light load of 100 W to a heavy load of 20 kW. The output voltage is regulated at 700 V rms. The capacitor voltage, load current, and load volt

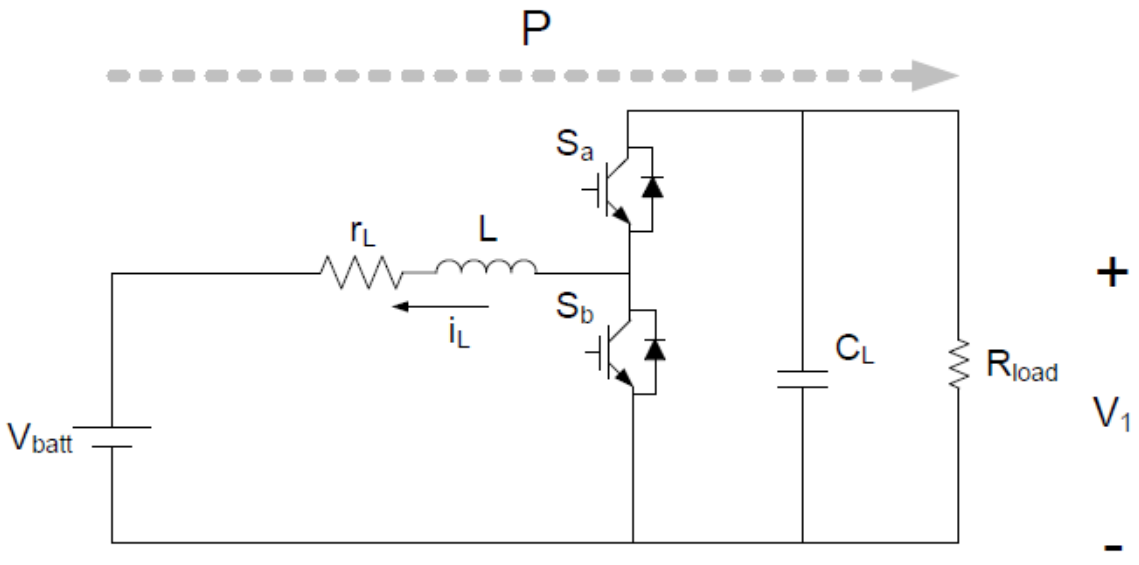

Figure 3.39: Black start (islanded) equivalent circuit

A dual loop control design is used in the both modes of operation of the bidirectional converter as shown in Figure 3.40. For grid connected mode the voltage reference V_{ref} is set equal to the nominal battery voltage therefore the battery charges at a constant voltage, constant current charging can be used by switching open the voltage feedback loop and using the inner current loop during with the appropriate charging current reference. During black start operation the voltage reference is set equal to the nominal low voltage DC link voltage of 400 V. The nominal battery voltage used is 206 V, therefore when the converter operates in grid connected mode it acts like a buck converter while in islanded mode it operates as a boost converter. Figure 3.40 shows the general control layout where the blue lines show the islanded mode and the green lines show the grid connected mode.

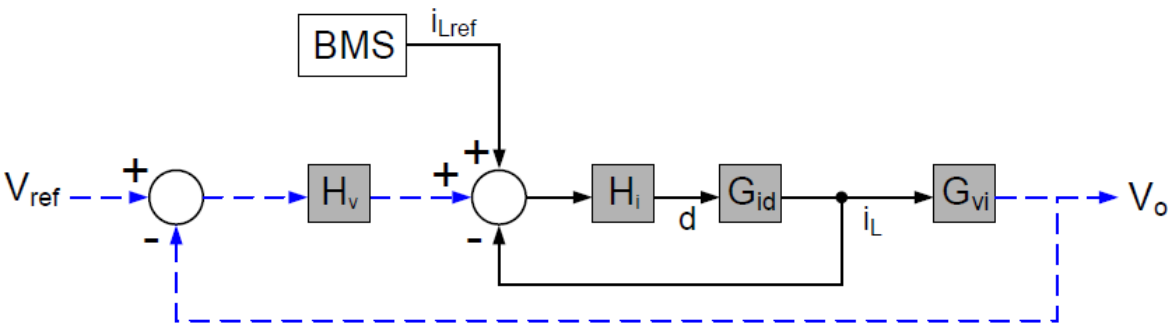

Figure 3.40: Control loop design

The inner current loop is designed first, the open loop transfer functions for grid connected and islanded modes of operation are given in Equation 3.24 and Equation 3.25 respectively. The converter system parameters are again given in table 3.4.

Table 3.4: Bidirectional Converter Parameters

Battery Bidirectional Converter Parameters		
Parameter	Value	Unit
V_{batt}	206	V
f_s	6	kHz
L	5	mH
r_L	0.5	Ω
C_L	2	mF
R_{load}	1600	Ω

$$G_{id} \quad \text{(grid connected)} = \frac{\hat{i}_L}{\hat{d}} = \frac{V_1}{Ls + r_L} = \frac{400\ V}{(5\ mH)s + 0.5} \tag{3.24}$$

$$\text{where } V_1 = V_{CL} = 400\ V$$

$$G_{id} \quad \text{(islanded)} = \frac{\hat{i}_L}{\hat{d}} = \frac{C_L R_1 V_1 s - D I_L R_1 + V_1}{C_L L R_1 s^2 + (C_L R_1 r_L + L)s + D^2 R_1 + r_L} = \frac{80000s + 49999.6}{s^2 + 100.313s + 26492} \tag{3.25}$$

where $R_1 = R_{load}$

$$V_1 = \frac{DR_{load}V_{batt}}{R_{load}D^2 + r_L} \tag{3.26}$$

$$V_2 = V_{batt} \tag{3.27}$$

$$I_L = -\frac{V_{batt}}{R_{load}D^2 + r_L} \tag{3.28}$$

The analysis of the converter is done under the worst case scenario which is when the converter is lightly loaded, for a 100 W load the equivalent load resistance can be calculated as $R_{load} = \frac{(400\ V)^2}{100\ W} = 1600\ \Omega$, the average values for D and I_L are calculated from eqs. (3.26) to (3.28) as $D = 0.5144$ and $I_L = -0.485996$. The transfer functions for the current loop in Equation 3.24 and Equation 3.25 are plotted in Figure 3.41.

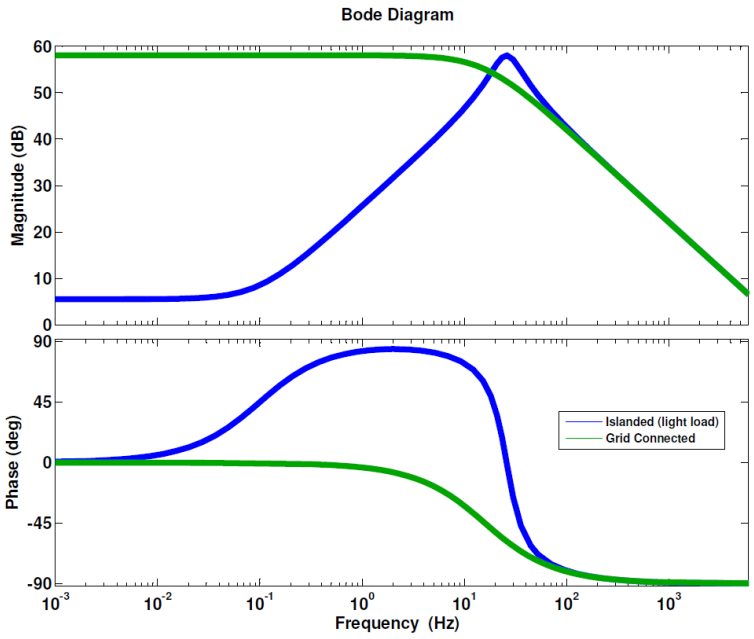

Figure 3.41: Bidirectional converter current loop gains

The loop gains for both modes of operation converge to the same values at around 100 Hz, therefore the inner current loop compensator can be shared for both conditions given the crossover frequency is high enough. The designed current loop compensator is a PI type and

is given in Equation 3.29, the loop gain with the PI compensator is plotted in Figure 3.42, the loop phase margin is 78.8° and a crossover frequency of 173 Hz.

$$G_{ci} = K_p + \frac{K_i}{s} = 0.012767 + \frac{4.1183}{s} \tag{3.29}$$

A step input of 10 A for grid connected mode and -10 A for islanded mode is given and the responses are shown in Figure 3.43 and Figure 3.44 respectively. The islanded mode step response is for the light load condition.

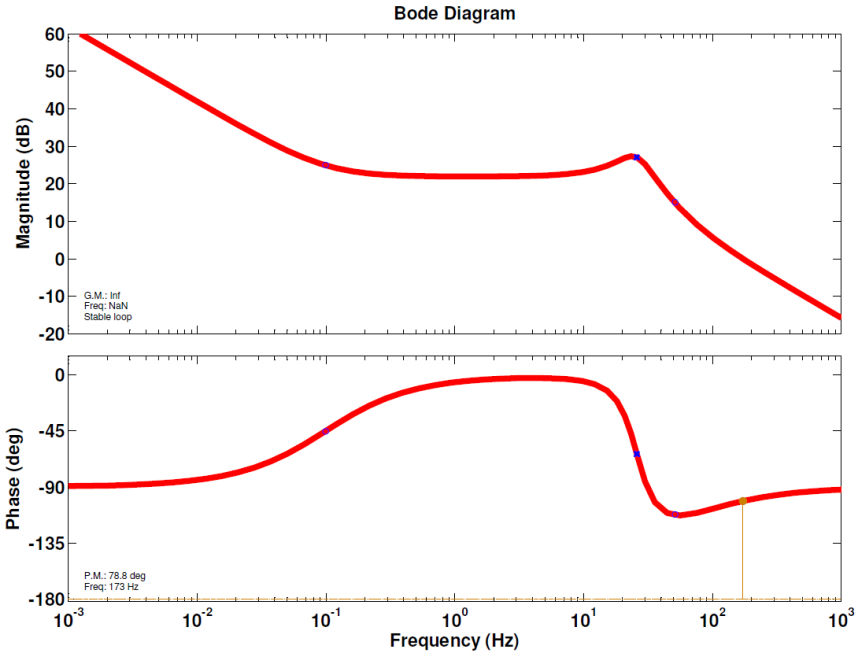

Figure 3.42: Bidirectional converter current loop gain with PI compensator

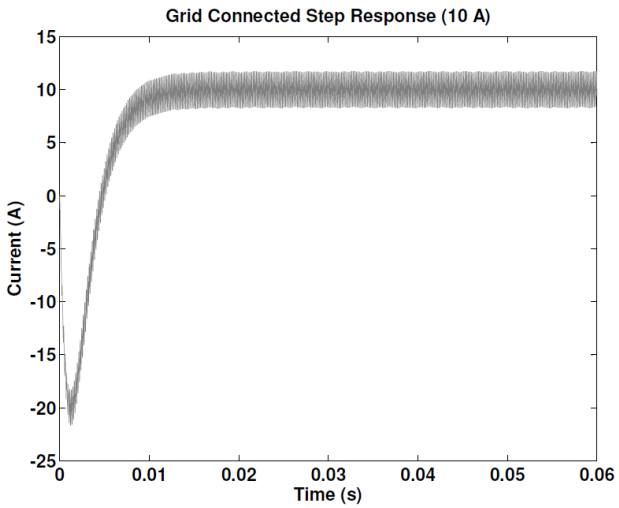

Figure 3.43: Grid connected current step response

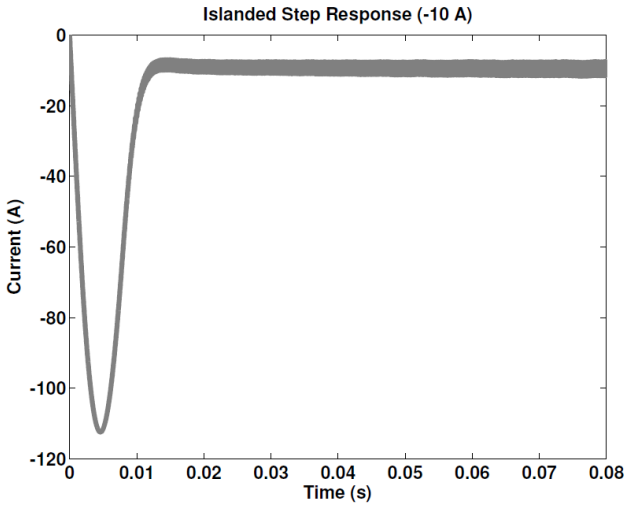

Figure 3.44: Islanded current step response

The voltage loop gain is equal to the closed loop gain of the current loop multiplied by the G_{vi} transfer function as shown in Equation 3.30, and G_{vi} is given in Equation 3.31. The parameter values are the same as the ones used in the current loop for a light load of 100 W.

$$T_v = G_{vi}\frac{G_{ci}G_{id}}{1 + G_{ci}G_{id}} \tag{3.30}$$

$$G_{vi} = \frac{\hat{V}_1}{\hat{i}_L} = \frac{-R_1 I_L L s - R_1 I_L r_L - R_1 D V_1}{C_H R_1 V_1 s - D I_L R_1 + V_1} = \frac{0.003037s - 256.896}{s + 0.624995} \tag{3.31}$$

For the bidirectional converter a PI type compensator can provide zero steady state error output to a DC reference waveform, therefore the PI compensator is designed. The compensator is given in Equation 3.32 and the voltage loop gain is shown in Figure 3.45, the loop has a phase margin of 59.2° and a crossover frequency of 16 Hz.

$$G_{cv} = K_p + \frac{K_i}{s} = -0.357119 + \frac{-21.007}{s} \tag{3.32}$$

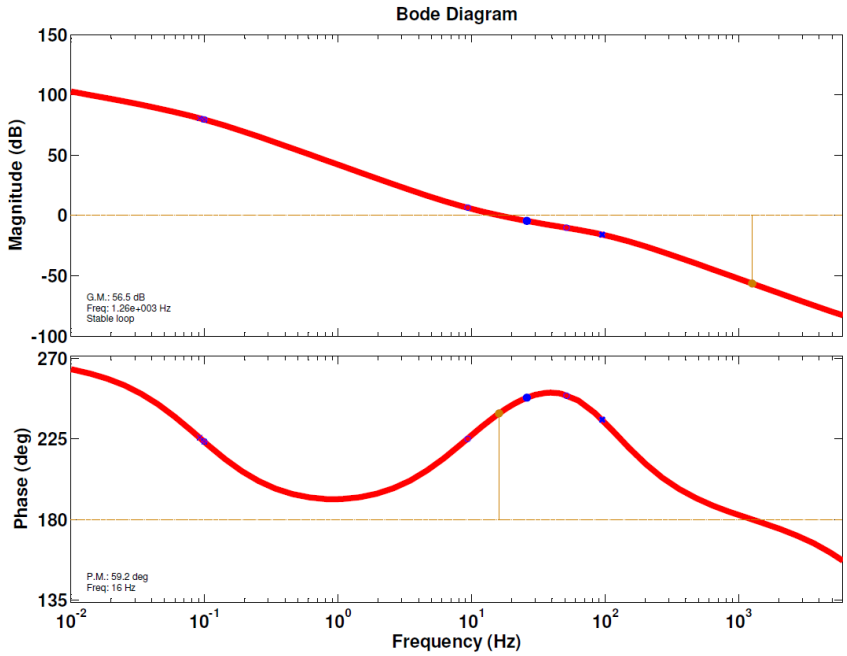

Figure 3.45: Bidirectional converter voltage loop gain with PI compensator

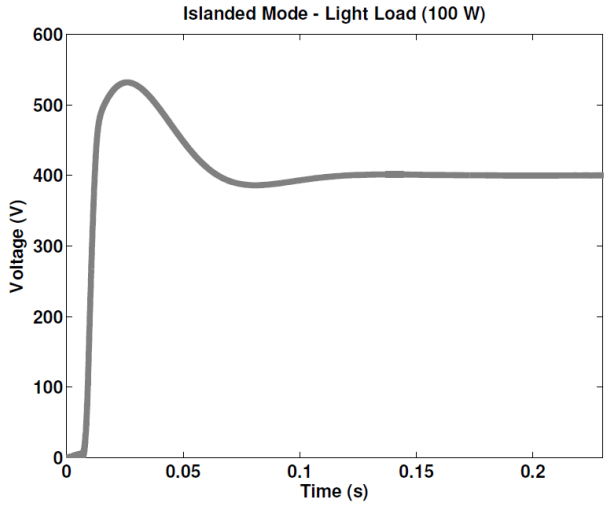

Figure 3.46: Load voltage regulation under light load

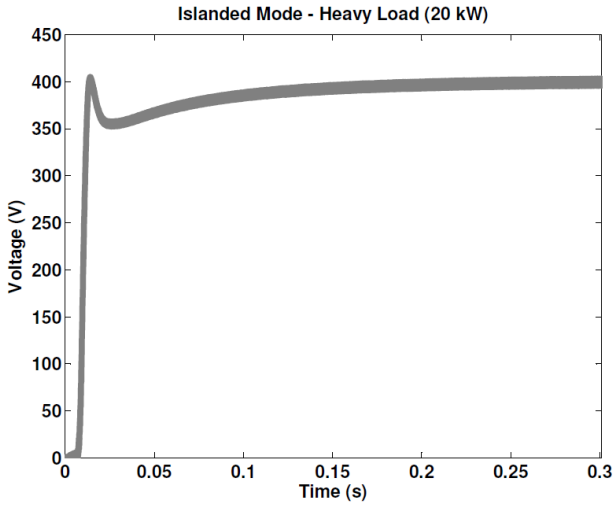

Figure 3.47: Load voltage regulation under heavy load

3.5 PV Panel Boost Converter Control Design

The PV panel is connected to the low voltage DC bus capacitance C_L through a boost converter. The PV panel power is injected into the DC link capacitor C_L, therefore the bidirectional converter for the battery must regulate the DC bus voltage to the specified 400 V while the PV

power is changing throughout the day. The PV panels are modeled as a current source whose current output is based on the plots given in Figure 2.42 while the terminal voltage is based on the solar insulation levels and follows Figure 2.44 tracked using the buck converter. Tracking the voltage level which produces the maximum power output of the PV panels is known as MPPT (Maximum Power Point Tracking) and algorithms to accurately determine what this voltage is can be found in many different literature [41] [42] [43]. The layout of the PV panel buck converter is shown in Figure 3.48, it can be seen that the converter does not change its control during mode changes from grid connected to islanded mode.

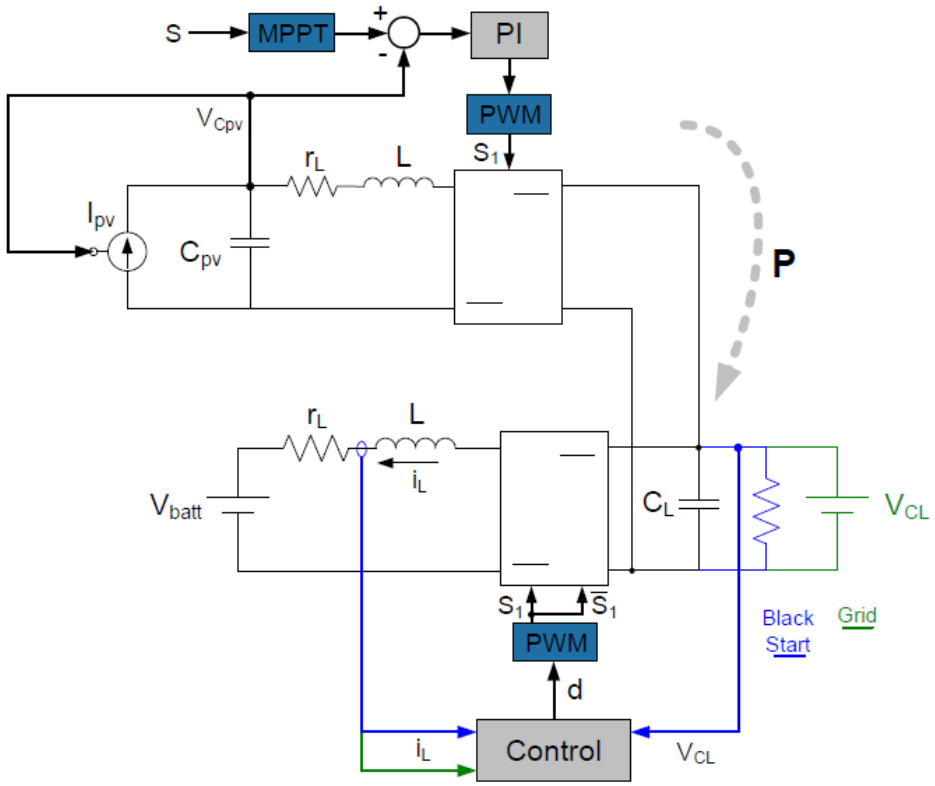

Figure 3.48: PV Panel Boost Converter

The PV panel power is injected to the DC bus capacitor, in grid connected mode the battery converter regulates the charging current of the battery bank, or if the battery bank is above the nominal charging point than the PV power can be delivered to the grid. In islanded mode the grid connection is lost and it is replaced by an equivalent load representing the power delivered to other solid state transformer loads during the black start procedure. The converter parameters are given in 3.5.

Table 3.5: PV Boost Parameters

PV Boost Converter Parameters		
Parameter	Value	Unit
V_{CL}	400	V
f_s	5	kHz
L	2	mH
r_L	0.1	Ω
C_{pv}	220	μF
C_L	2	mF

The PV panel input voltage is controlled using the boost converter with a PI type controller. The control loop is given in Figure 3.49 below. The model represents a boost converter with an MMPT, the solar insolation initially determines the optimal PV terminal voltage which is the boost converter voltage reference. As the boost converter regulates the PV terminal voltage the output current is determined based on the model.

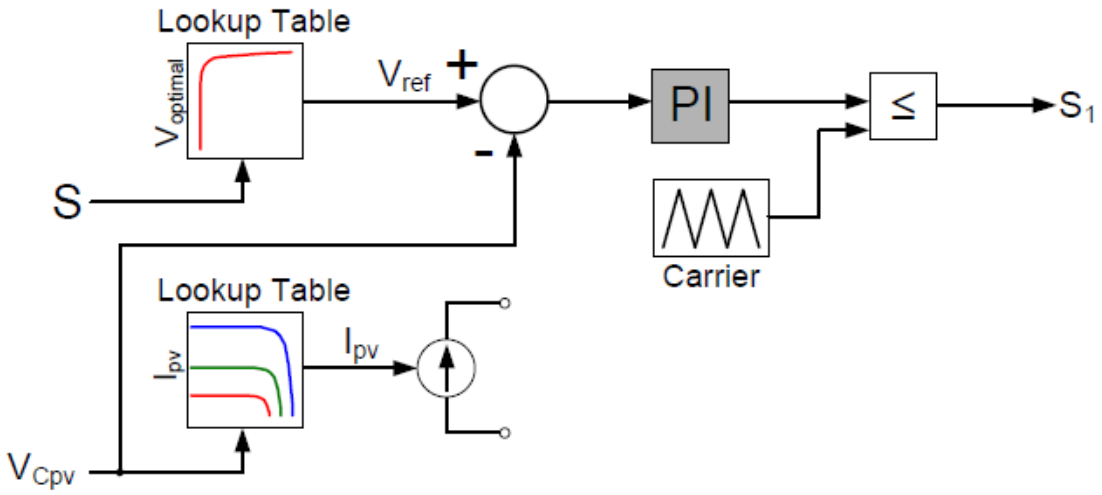

Figure 3.49: PV boost converter loop

$$PI = K_p + \frac{K_i}{s} = 0.9 + \frac{10}{s} \tag{3.33}$$

The converter operation for grid connected mode is shown in Figure 3.50. At the start

the PV solar insolation is set at 1 pu and the battery charging current reference is 0 A. It can be seen that the PV panels inject the peak power of approximately 5 kW, because the battery is not charging the 5 kW PV power flows to the grid. In the second step the solar insolation drops to 0.5 pu and the PV output power drops to approximately 2.35 kW, the battery charging current reference is kept at 0 A and it can be seen that the injected grid power drops correspondingly while the battery power remains at 0 W. In the third step the battery charging current reference is set to 20 A while the solar insolation remains at 0.5 pu. The power delivered to the battery is approximately 4.3 kW, however the PV output is still only approximately 2.35 kW, therefore it can be seen that the grid power increases and becomes positive and starts sourcing power at approximately 1.99 kW to the battery. In the fourth step the solar insolation increases to 1 pu while the battery charging current reference remains at 20 A. The PV power output increases enough to supply the full battery load and the grid power again becomes positive with approximately 600 W of power being delivered to the grid. In the fifth step the solar insolation is reduced to 0 pu while the battery charging current reference is kept at 20 A. The PV power reduces to 0 W and the grid power becomes negative taking on the the full load power of charging the battery at approximately 4.3 kW. The sixth and final step the solar insolation remains at 0 pu and the battery charging current reference is set to 0 A, in this case it is seen that the grid power and battery current correspondingly become 0 W and 0 A.

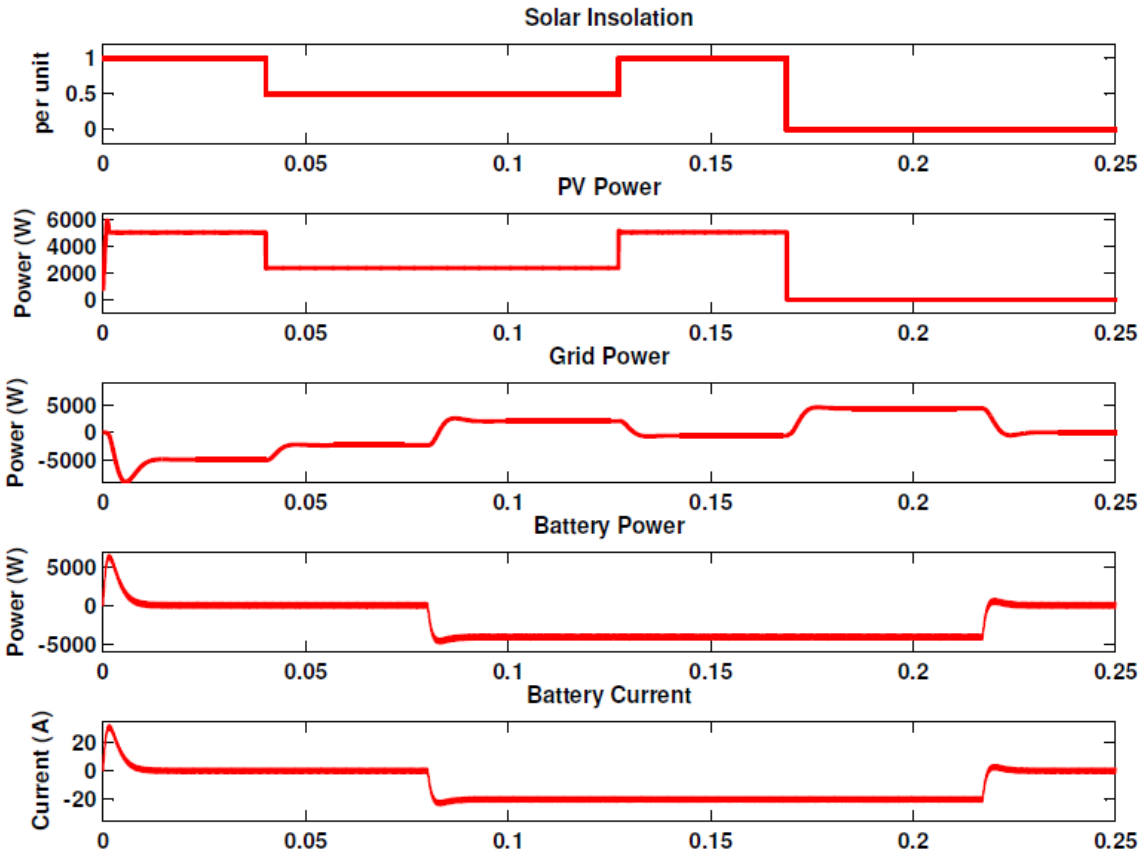

Figure 3.50: PV and battery converter testing - grid connected mode

In the grid connected mode the battery charging current reference must be controlled by a battery management system in order to charge the battery appropriately. It should be noted in Figure 3.50 that a source delivering power is defined as positive.

The converter operation for islanded mode is shown in Figure 3.51, in the first step the PV panel is delivering its rated power of approximately 5 kW and the load is a light load drawing 100 W. The DC bus voltage is regulated to 400 V and the battery absorbs the excess power delivered by the PV panels approximately 4.8 kW. Next the solar insolation is reduced to 0 and the PV panels output no power, the DC bus voltage drops slightly around 0.25 seconds and is regulated back to 400 V. The load power is kept at 100 W, therefore the battery starts to deliver the full load power. In the next step, at 0.5 seconds the load is changed to a heavy load of 16.1 kW while the solar insolation is kept at 0. Another transient is seen in the DC bus voltage, however it is quickly regulated back to 400 V while the battery power output increases to meet the load demand. In the final step at 0.76 seconds the solar insolation is increased to 0.5 and the PV panels injects 2.35 kW of power. The battery power decreases as the PV panel

injects power and another transient is seen on the DC bus voltage which is quickly regulated back to the nominal 400 V bus voltage.

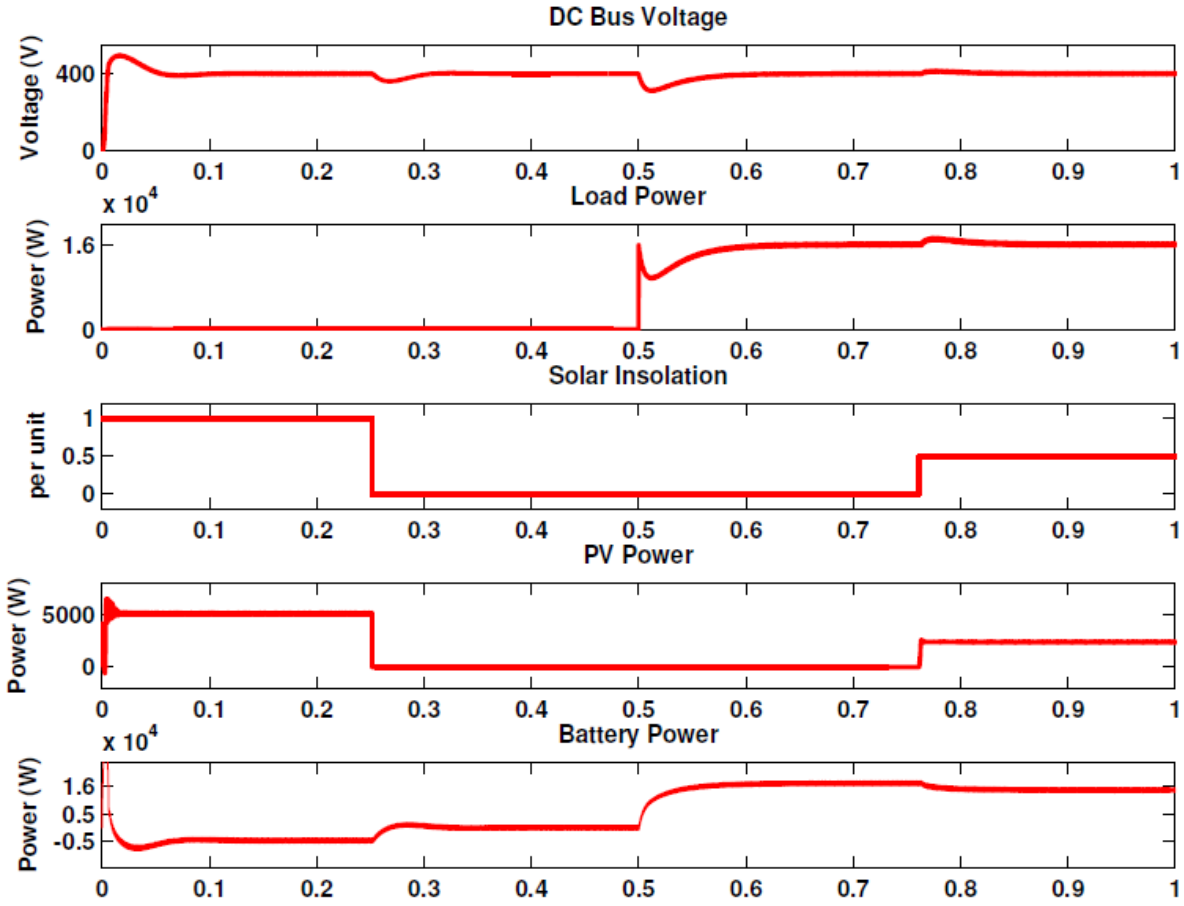

Figure 3.51: PV and battery converter testing - islanded mode

Chapter 4

Microgrid System Simulation

The system simulation is done to test the operation of the solid state transformer in the black start operation and grid connected modes. The grid connected mode is first tested followed by the startup of the solid state transformer in black start mode of operation after the grid connection is lost. The control systems for the three stages of the solid state transformer including the solar panel and battery energy storage system connected at the low voltage DC bus are included and cascaded together to form the complete control system for the solid state transformer. A system diagram showing a simple two solid state transformer system, one with black start capability and the other without, the diagram reviews the overall operation of the converters and is shown in Figure 4.1. A simplified control diagram is shown at the bottom which details the operation of the black start solid state transformer based on the detection of an islanding event. The blocks represent the stages of the solid state transformer, the blue signals on the top of the blocks represent the measured signals required for the control system for that block and the red signals what system variable is being controlled by that block or is an input to that block. The red arrow originating from the block indicates the system variable that is being controlled by that block, while a red arrow ending on a block indicates it is an input to that block.

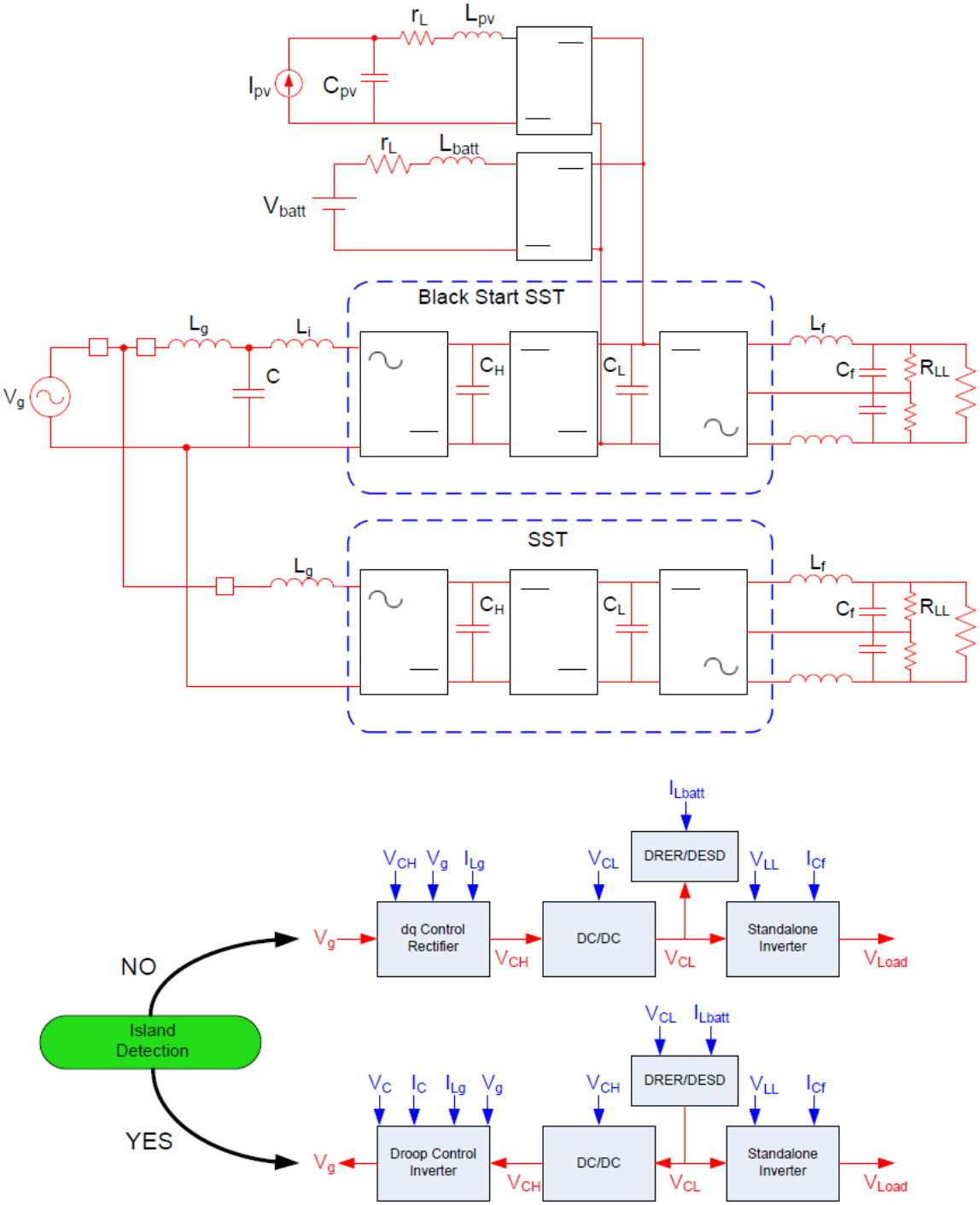

Figure 4.1: System overview

The simulation is again done in Matlab Simulink with PLECS, the simulation subsystems

are shown in figs. 4.2 to 4.7. The top level of the simulation shown in Figure 4.2 shows the black start solid state transformer with the PV/BESS system connected at the low voltage DC bus. The local load inverter load is shown on the left side, while on the grid side of the solid state transformer the LCL filter along with the line impedance is shown. Additionally a grid disconnect switch is used to perform the transition from grid connected to islanded mode of operation. In the grid connected mode the ideal AC source supplies the solid state transformer, when the grid is disconnected an AC load is switched on which represents the load of a non black start solid state transformer connected in the microgrid to which the black start solid state transformer is delivering power. Figure 4.3 shows the three stages of the solid state transformer, namely the local load inverter on the left, the dual active bridge in the center between the two DC buses, and the grid tied rectifier/stand alone inverter on the right. The PV and BESS system is shown in Figure 4.7 with the BESS converter on the bottom and the PV converter on the top.

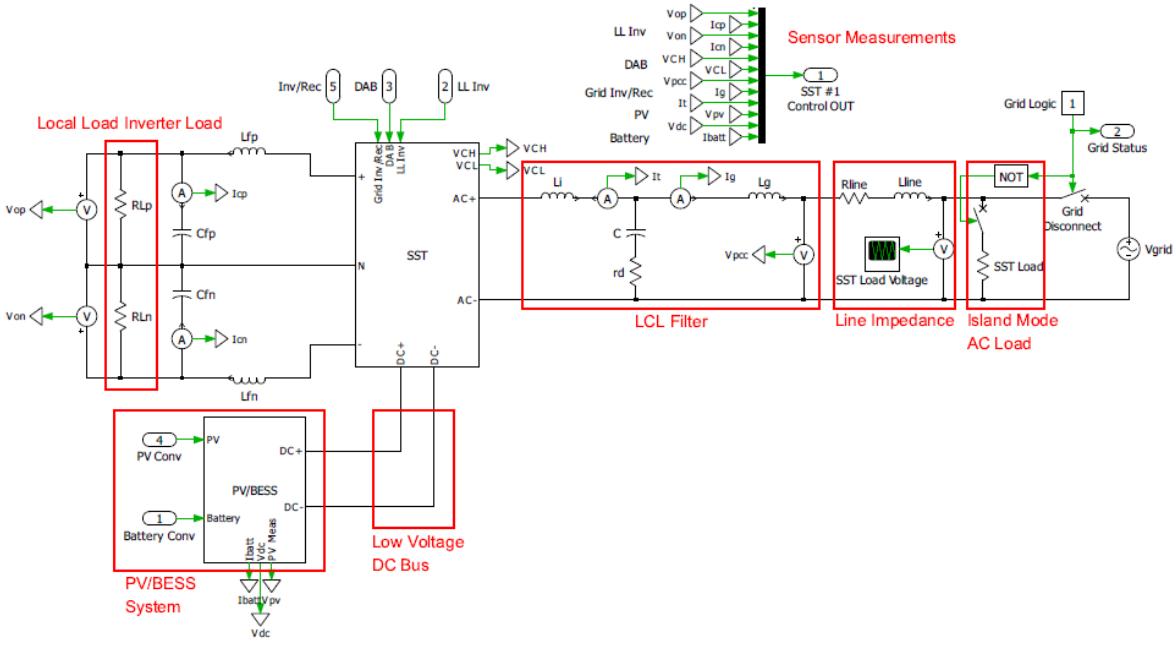

Figure 4.2: SST with PV and BESS simulation model

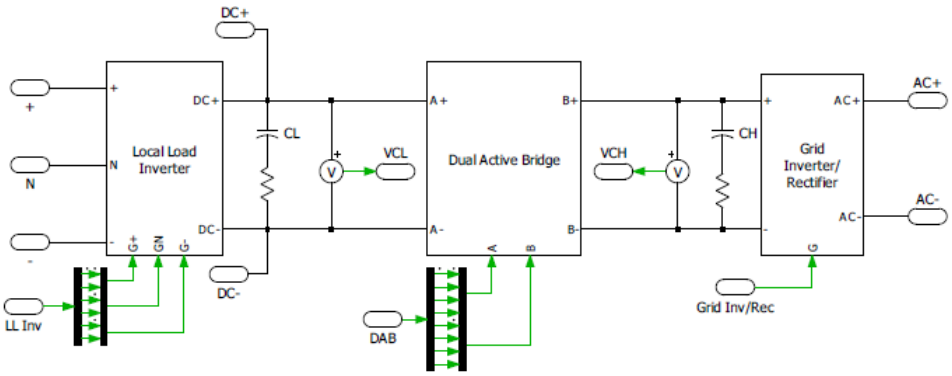

Figure 4.3: SST converter blocks

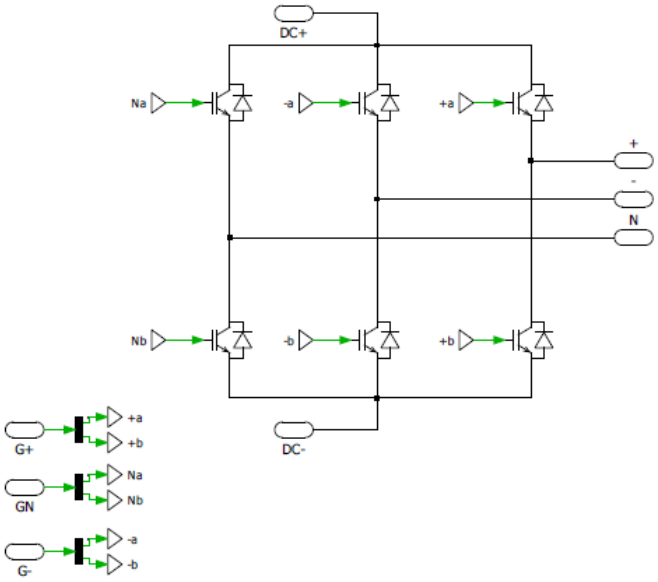

Figure 4.4: Local load inverter subsystem

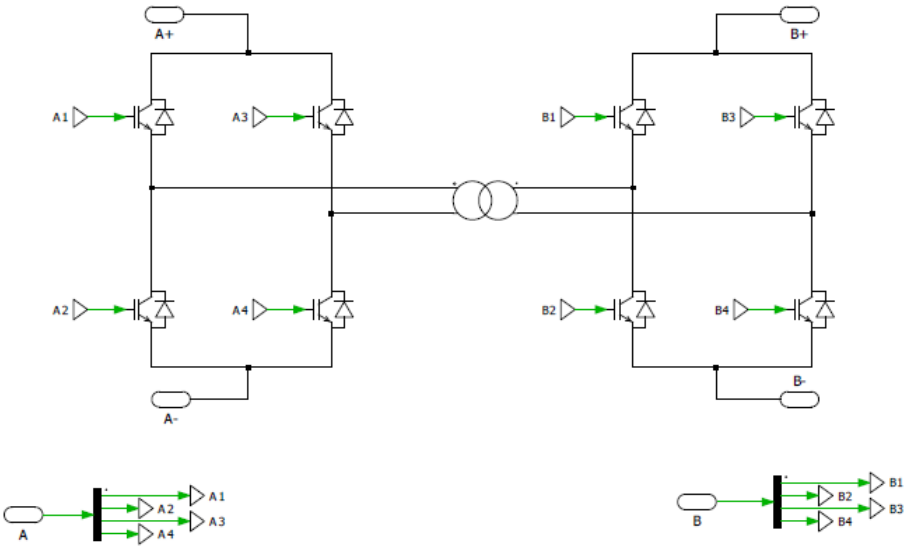

Figure 4.5: Dual active bridge subsystem

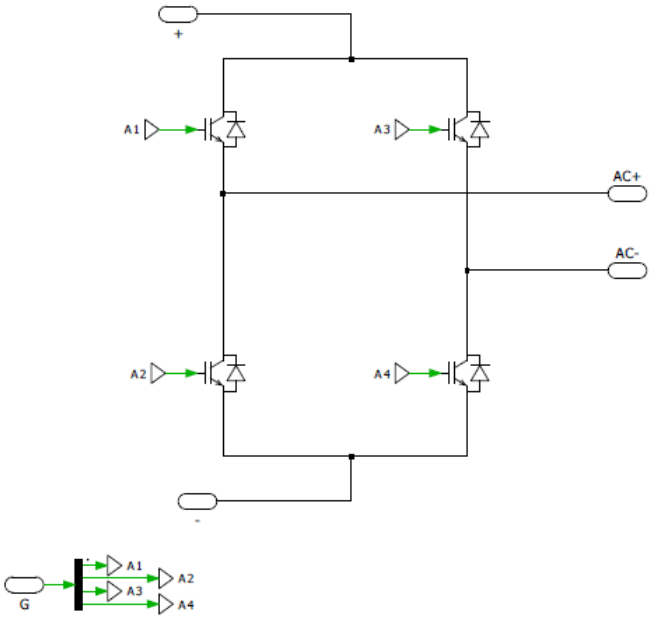

Figure 4.6: Rectifier/Inverter subsystem

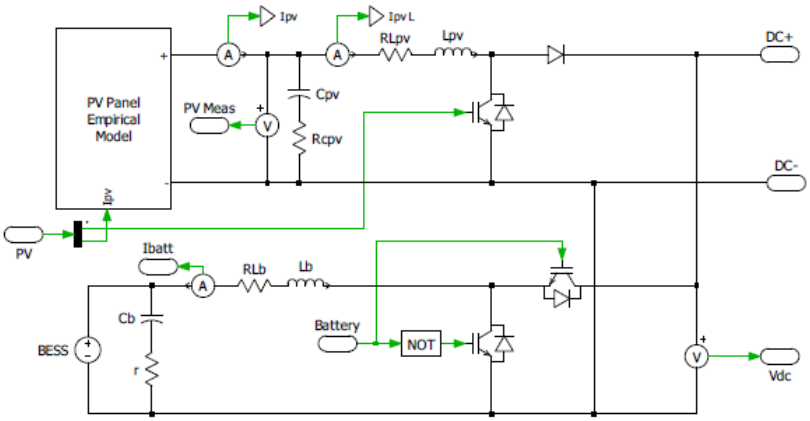

Figure 4.7: PV and BESS converter subsystems

The startup procedure is an important consideration for this application of the solid state transformer and the logic for starting the SST in both modes of operation has been considered. The logic is shown in figs. 4.8 to 4.11 with all of the logic using the DC bus capacitor voltages as the measurement which determines the startup process along with the grid connection status.

For the grid tied rectifier/black start inverter operating in black start mode, the high voltage DC bus voltage V_{CH} is monitored to determine if it falls in an interval around the steady state value of 12 kV, for instance between 11.5 kV to 12.5 kV. When the bus voltage falls within this range a timer is sampled and a countdown is initiated, a time is chosen (shown as the "Steady State Time Allowance" below) for which it is decided that if the bus voltage remains within the steady state operating interval for that time then the bus voltage is determined to have reached steady state and the inverter starts up. In grid tied mode the grid tied rectifier starts immediately as shown by the switch.

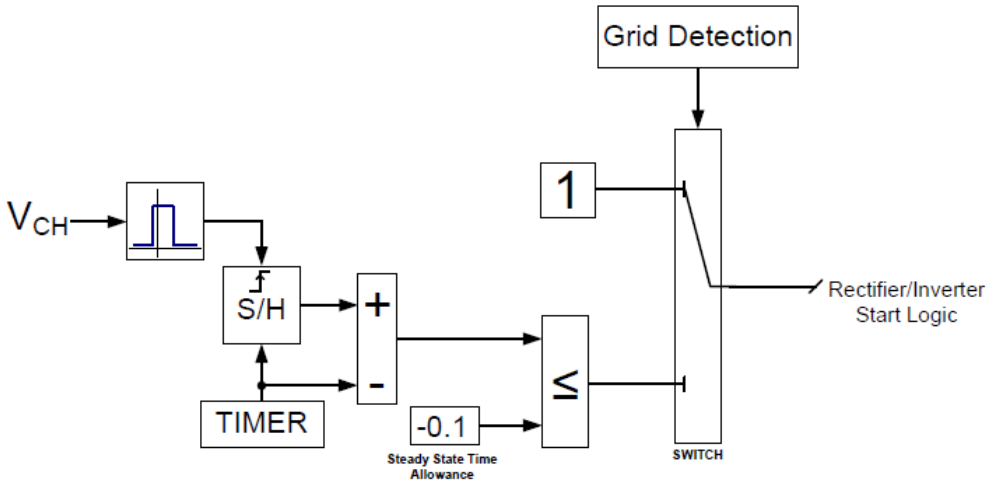

Figure 4.8: Rectifier/Inverter startup logic

The DAB startup logic shown in Figure 4.9 is similar except the high voltage DC bus V_{CH} is monitored in grid tied mode and in black start mode the low voltage DC bus V_{CL} is monitored. Again when the voltage lies within the interval for the specified time period then the DAB will start.

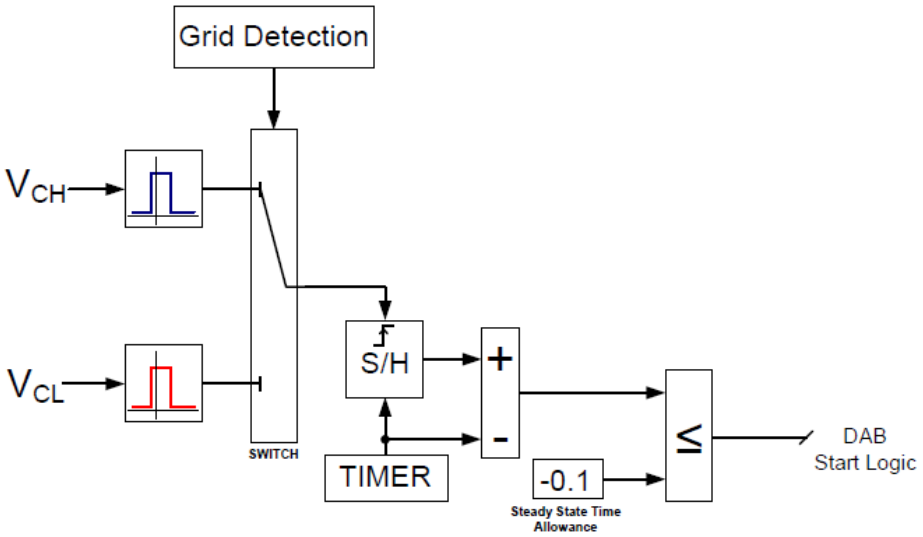

Figure 4.9: Rectifier/DAB startup logic

As the logic shows in Figure 4.10, the local load inverter needs only to monitor the low

voltage DC bus V_{CL} in both grid tied and black start modes of operation, whenever the low voltage DC bus is at its nominal voltage the local load inverter can supply the connected load.

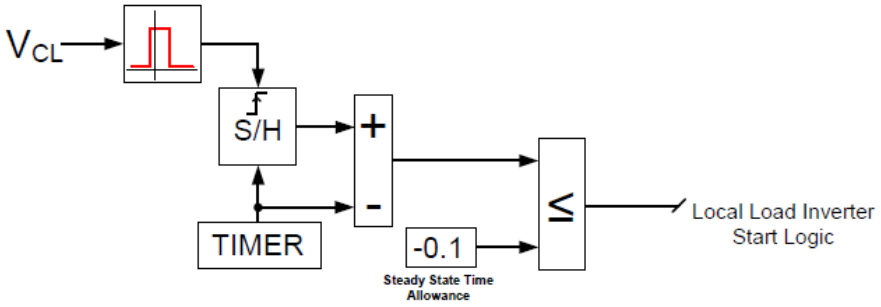

Figure 4.10: Rectifier/Local Load Inverter startup logic

The BESS converter must startup immediately when operating in black start mode because it is the energy source for the solid state transformer. While operating in grid tied mode the BESS converter will monitor the low voltage DC bus V_{CL}, when it has reached steady state the BESS converter can begin to charge its batteries.

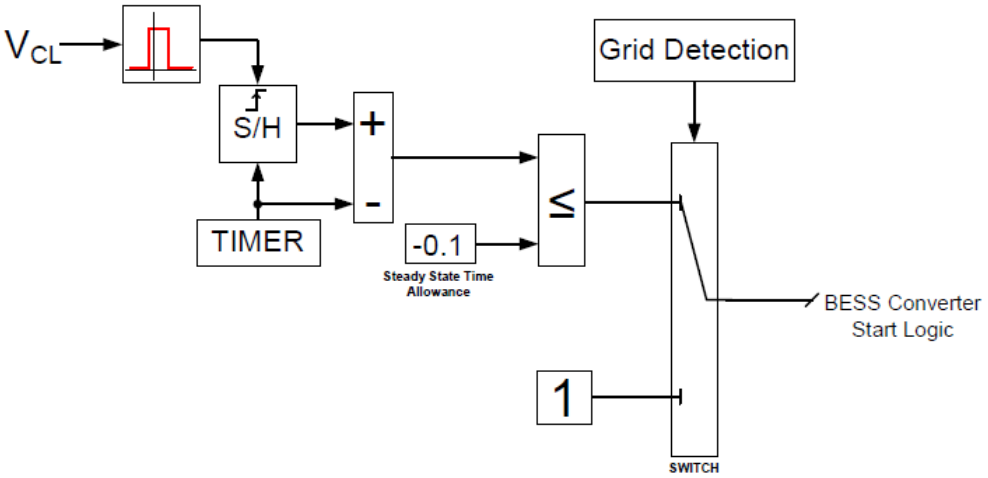

Figure 4.11: BESS startup logic

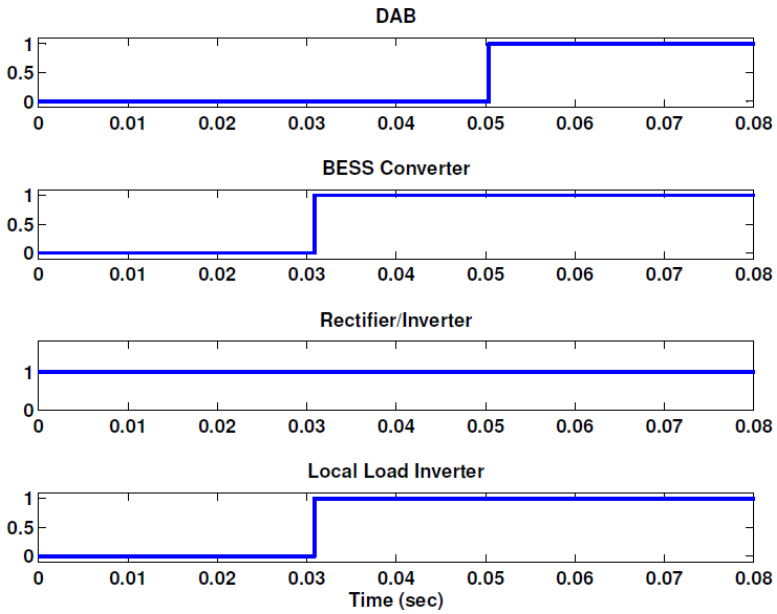

Figure 4.12: Grid connected starting logic

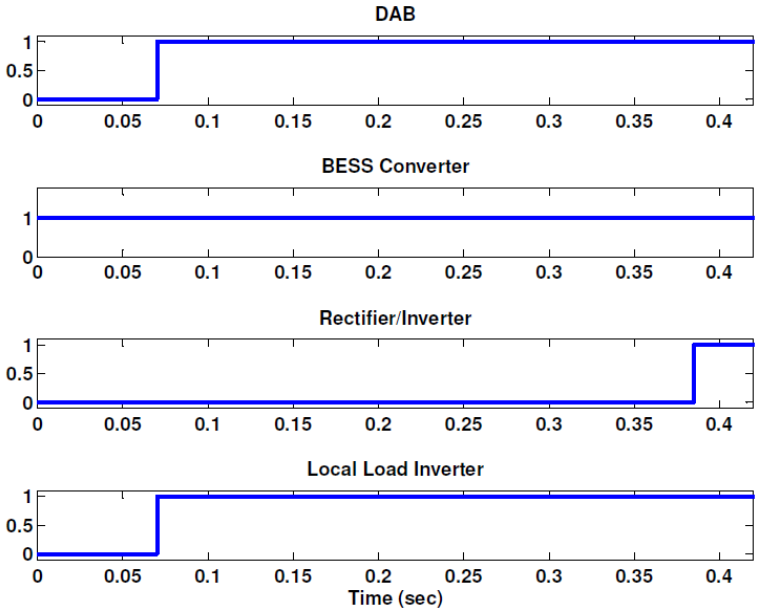

Figure 4.13: Black start logic

Figures 4.12 and 4.13 show the startup logic during the simulation activating in the proper

order. The logic was built into the Matlab simulation and is shown in the following figures.

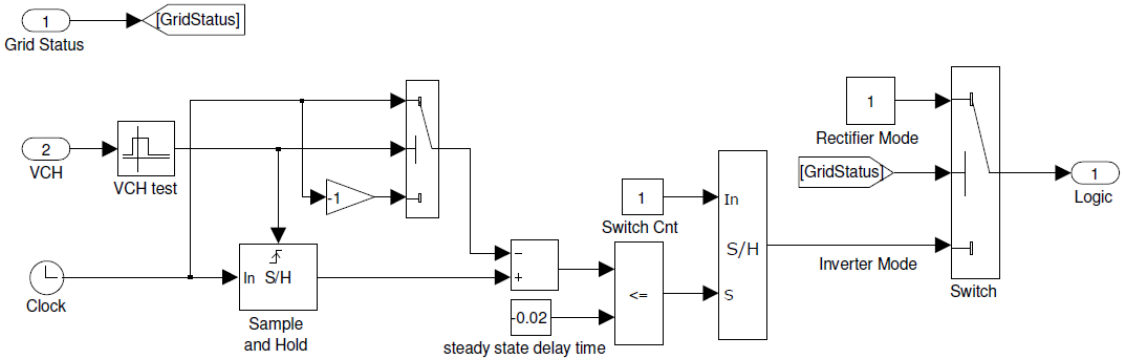

Figure 4.14: Rectifier/Inverter logic

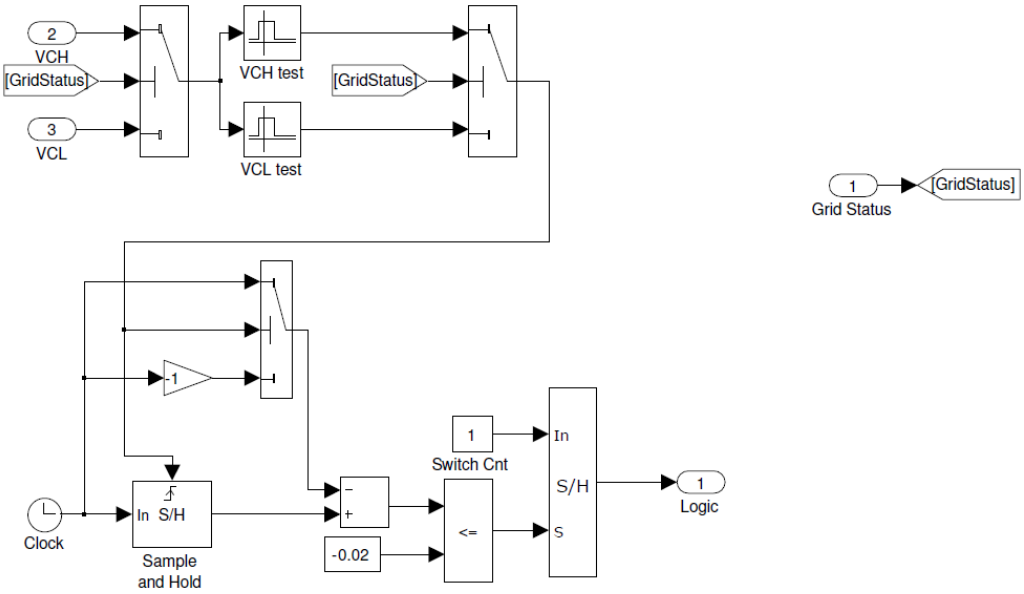

Figure 4.15: DAB logic

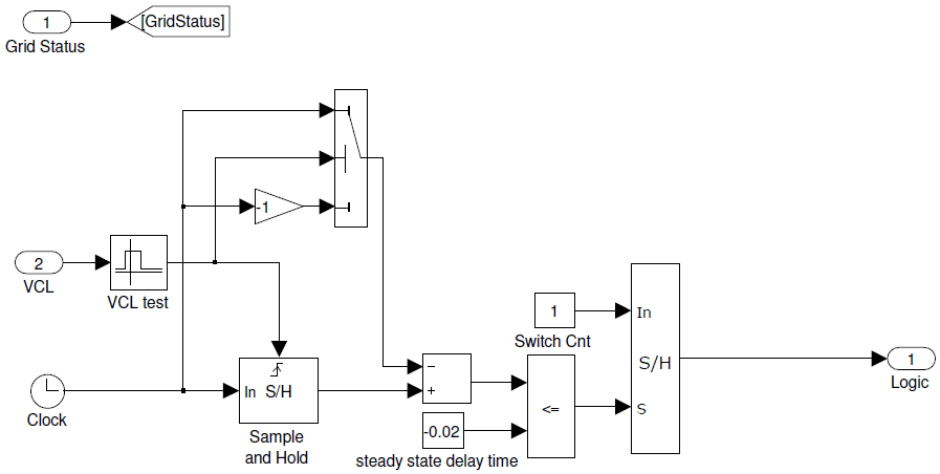

Figure 4.16: Local Load Inverter logic

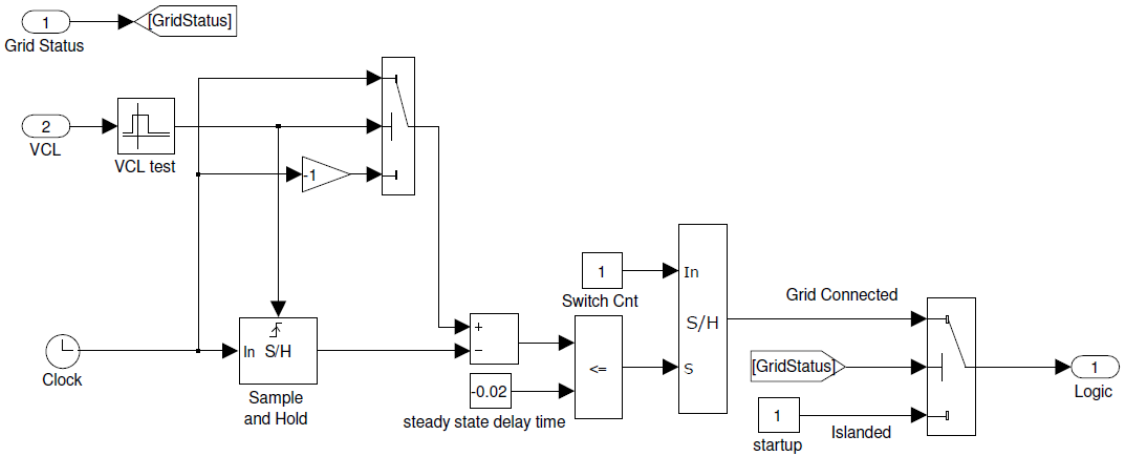

Figure 4.17: BESS Converter logic

4.1 Grid Connected Mode

In the grid connected mode the solid state transformer operates to supply its own local load from the PCC voltage. The first stage operates as a rectifier, the second stage operates as a DC/DC converter reducing the voltage, and the third stage operates as an inverter to supply the load. Figure 4.18 shows the solid state transformer in grid connected mode, for this test only one solid state transformer is tested. The grid voltage is 7.2 kV, the high voltage DC bus

is 12 kV, and the low voltage DC bus is 400 V. A 100 W local load is connected to the solid state transformer. The PV system is only used to charge the battery bank in the grid connected mode in order to simplify the simulation. However excess power generated by the PV system could be returned to the grid as previously shown in the PV/BESS system analysis, however for the actual system this will require another mode change of the second stage DAB to reverse power flow, therefore in order to simplify the simulation the battery bank will only be charged from the PV system.

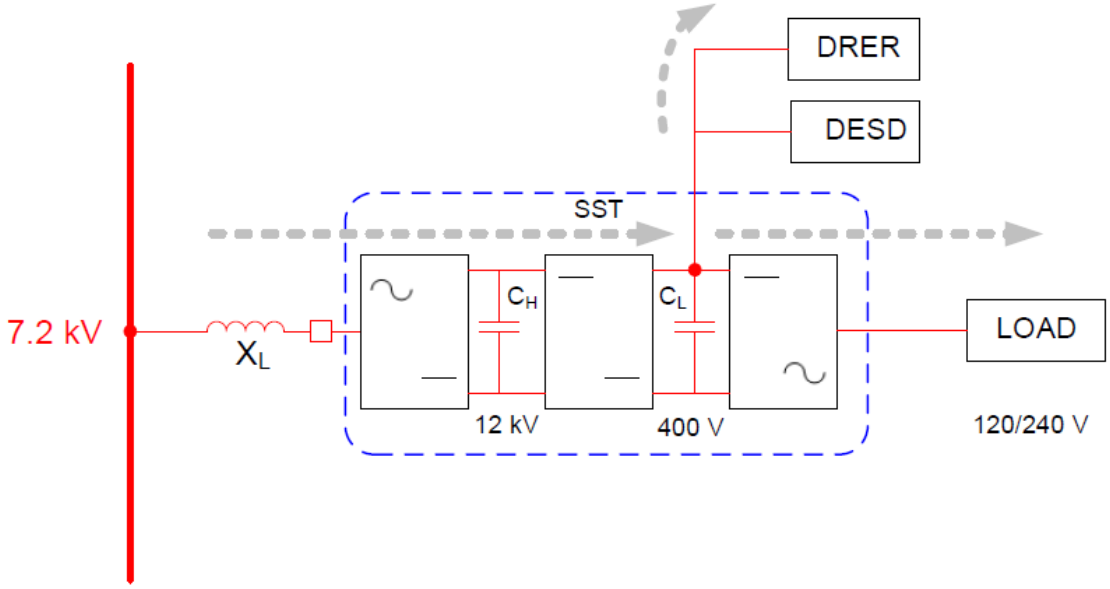

Figure 4.18: Grid connected test

The parameters used in the grid connected test are shown in table 4.1. The parameter $R_{local\ load}$ is the load for the local load inverter (120 V load for both phases) while R_{line} and L_{line} are the line impedance parameters.

Table 4.1: Grid connected mode parameters

Parameter	Value	Unit
V_g	7.2	kV
V_H	12	kV
V_L	400	V
C_H	50	μF
C_L	2	mF
$R_{local\ load}$	144	Ω
R_{line}	1.6	Ω
L_{line}	270	μH

Figure 4.19 shows the simulation results of the grid connected test. The solid state transformer begins by rectifying the input grid voltage of 7.2 kV to 12 kV across the high voltage DC bus by operating in the boost rectifier mode of operation controlled in the DQ frame. The low voltage DC bus charges to 400 V controlled by the dual active bridge shortly after the high voltage DC bus begins to charge. Once the low voltage DC bus has reached 400 V, the local load inverter begins to supply its 120/240 V load, this test only uses a 120 V load. As previously mentioned, in order to simplify the simulation for grid connected mode the battery only charges from the injected PV power, although excess PV power can go to the grid as shown previously this would require another mode change of the dual active bridge. The battery charging current remains at zero until the PV begins injecting power into the low voltage DC bus. The PV power is injected into the low voltage DC bus at approximately 0.096 seconds causing the battery to charge at a current of 30 A and stops injecting power at 0.4 seconds.

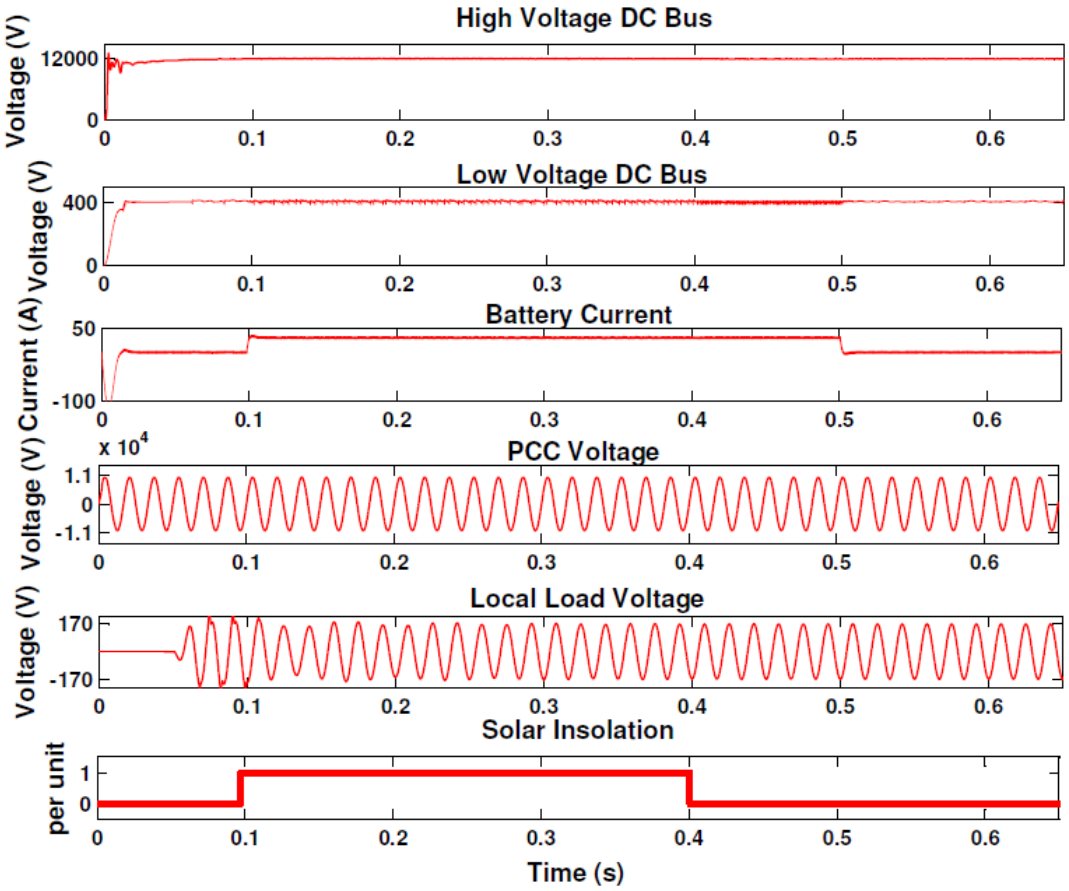

Figure 4.19: Grid connected operation

A load change test is performed on one of the local load inverter phases and the DC bus regulation is observed along with the load voltage regulation of both phases. The load change is done at 0.5 seconds at one phase from a load of 1.44 Ω (10 kW) to 144 Ω (100 W). In Figure 4.20 the phase 1 load changes from 10 kW to 100 W at 0.5 seconds as seen in detail in Figure 4.21, in Figure 4.22 the load voltage is regulated properly. The load power for both phases of the inverter are shown in Figure 4.23 and the phase 1 load power change is shown in detail in Figure 4.24 and it is shown that the average load power changes from 10 kW to 100 W at 0.5 seconds.

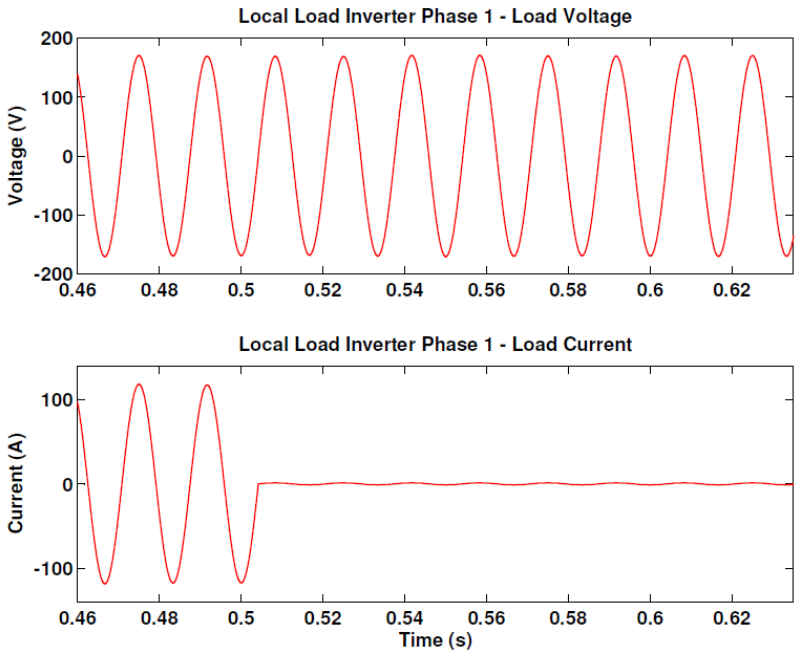

Figure 4.20: Voltage and current phase 1 local load inverter

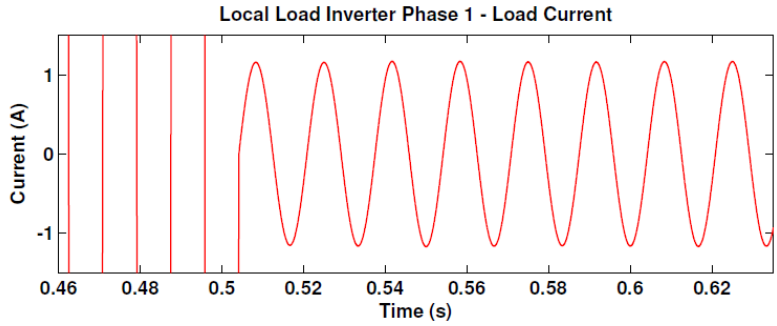

Figure 4.21: Current response to load change at 0.5 seconds

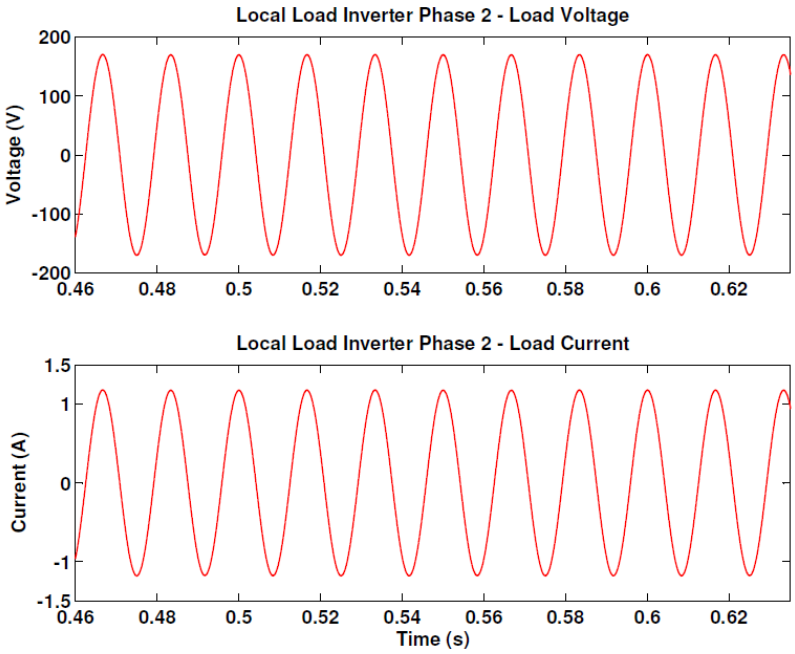

Figure 4.22: Voltage and current phase 2 local load inverter

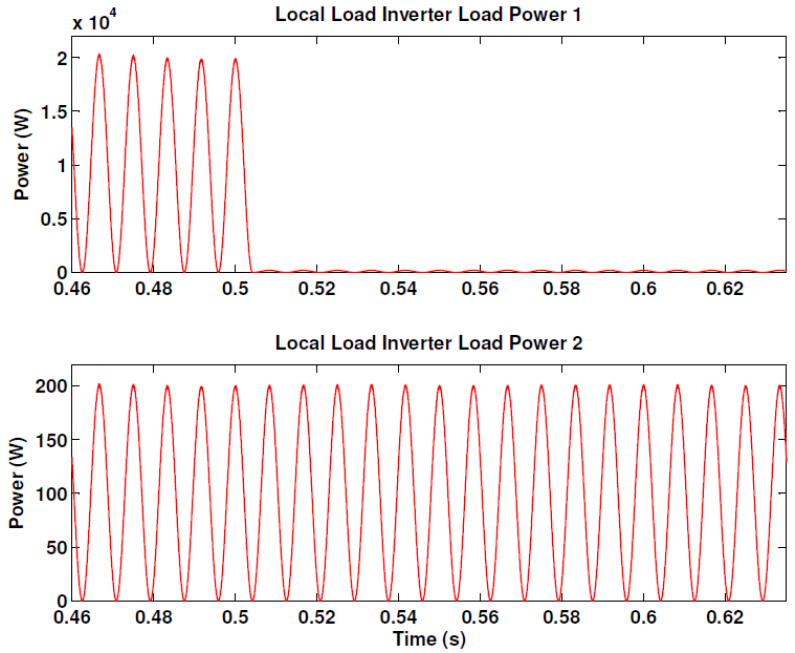

Figure 4.23: Local load inverter phase 1 and 2 power

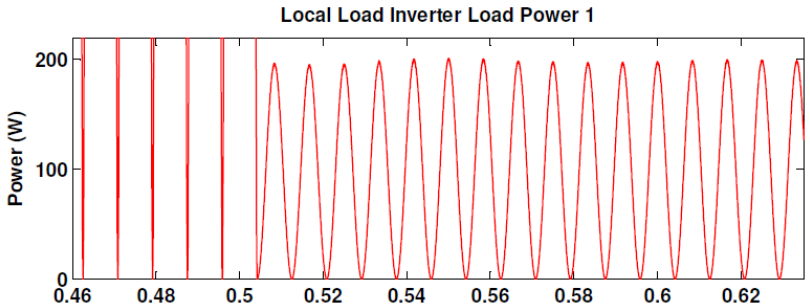

Figure 4.24: Phase 1 power response to load load change at 0.5 seconds

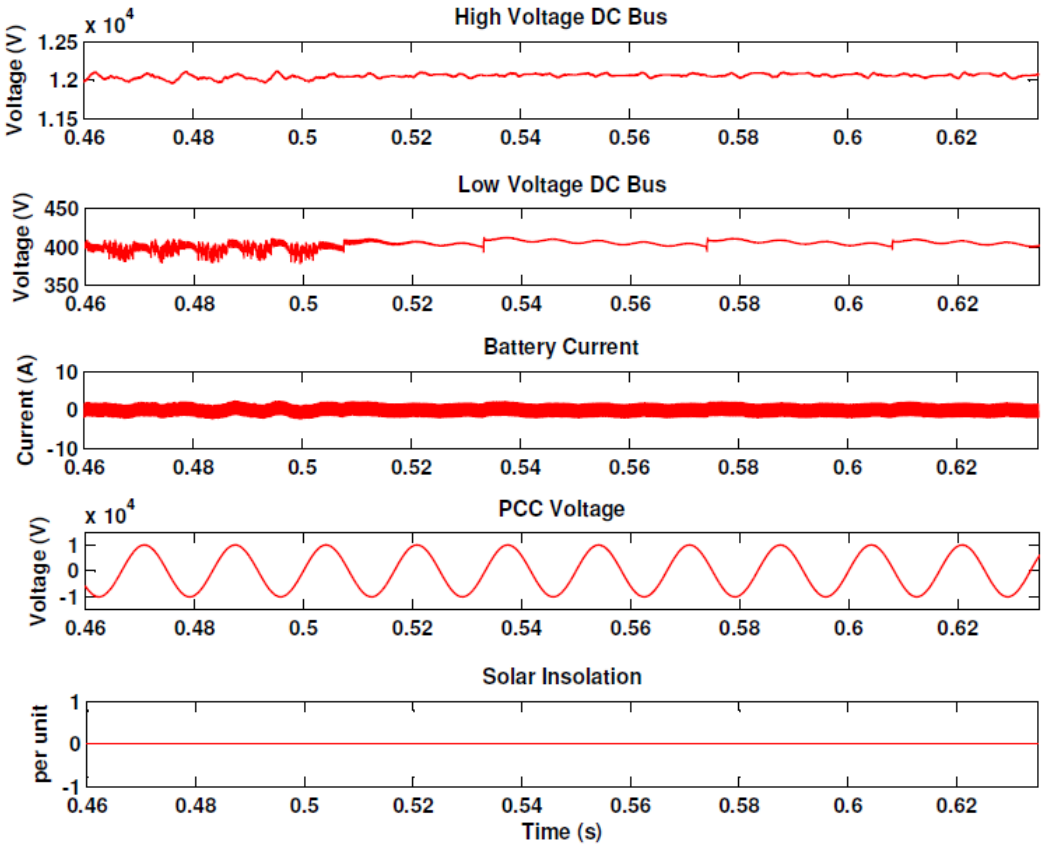

Figure 4.25: System dynamics during load change

4.2 Black Start Restoration

The black start operation of the solid state transformer is tested in two parts, in the first part the solid state transformer supplies an AC load which represents a non black start solid state transformer with its own load. A solid state transformer with its own load could be used, however to simplify the simulation an AC load is connected directly to the PCC of the black start solid state transformer. The second part consists of two black start solid state transformers supplying an AC load again representing a solid state transformer without black start capability.

4.2.1 Black Start restoration without parallel operation

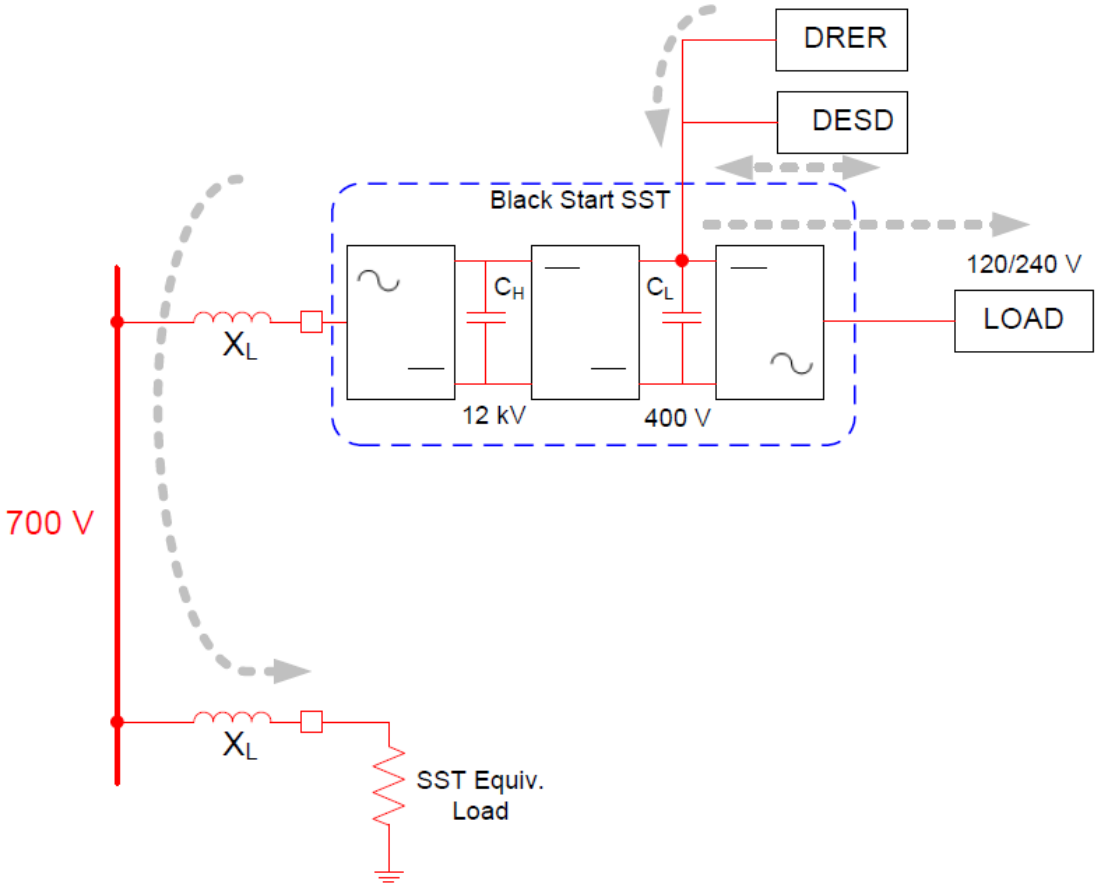

Figure 4.26: Black start test

The parameters used in the black start test are shown in table 4.2. The parameter $R_{ac\ load}$ is the equivalent AC load representing the load of the non black start solid state transformer.

Table 4.2: Black start parameters

Parameter	Value	Unit
V_{PCC}	700	V
V_H	12	kV
V_L	400	V
C_H	50	μF
C_L	2	mF
$R_{local\ load}$	144	Ω
R_{line}	1.6	Ω
L_{line}	270	μH
$R_{ac\ load}$	49	Ω

Figure 4.27 shows the simulation results of the black start test. The starting procedure begins with the BESS/PV system charging the low voltage DC bus to the nominal 400 V. The battery discharge current increases while the capacitor is being charged as seen in the third plot, once the low voltage DC bus is charged the battery current returns to 0 A. At 0.175 seconds two events happen, first the local load inverter starts and supplies the 144 Ω load (a 240 V load is not connected during the test), second the dual active bridge starts to charge the high voltage DC bus to the nominal 12 kV. During the high voltage DC bus charging the low voltage DC bus drops slightly and the battery discharge current increases until it reaches 12 kV after which there is an overshoot of the low voltage DC bus (0.47 seconds) due to the integrator of the PI controller of the battery converter. At 0.67 seconds the PV system injects its rated power as the solar insolation increases to 1 pu, the high and low voltage DC buses continue to be regulated at their nominal values and the battery charges at approximately 22 A. At 0.928 seconds the grid tied inverter starts and brings the PCC voltage level to 700 V, this causes a decrease in the battery charging current seen at 0.928 seconds. At 1.186 seconds the solar insolation is decreased to 0 pu and the solar panels inject no power to the low voltage DC bus, this loss of power requires the battery to again start discharging, the high and low voltage DC buses continue to be regulated during the procedure.

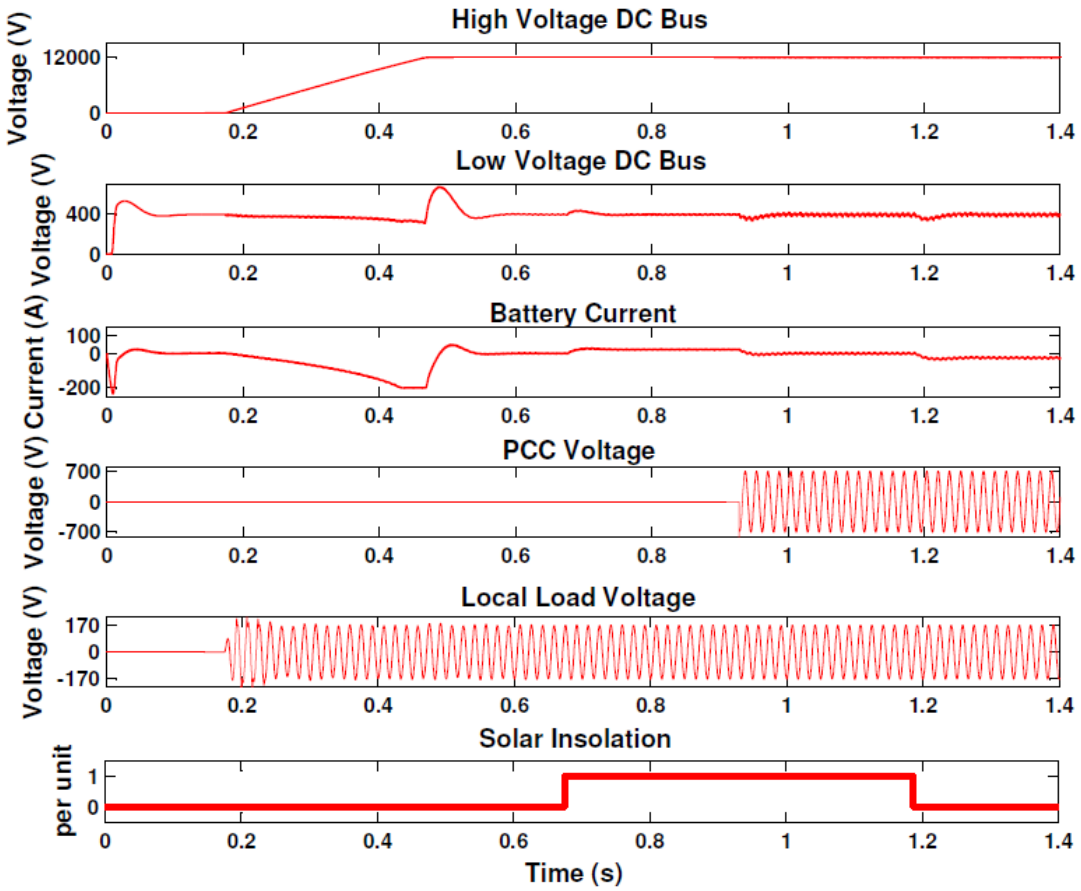

Figure 4.27: Black start operation with external ac load

4.2.2 Black Start restoration with parallel operation

The black start restoration procedure requires the solid state transformer to operate in parallel with other solid state transformers to provide the required load power. The black start solid state transformers capability of sharing load power with other black start solid state transformers is demonstrated in this simulation. Two black start solid state transformers start up to supply their local loads and operate in parallel to supply an AC load which represents a non-black start capable solid state transformer with its own local load. Figure 4.28 shows the topology of the simulation in block diagram format, Figure 4.29 shows the simulation circuit diagram.

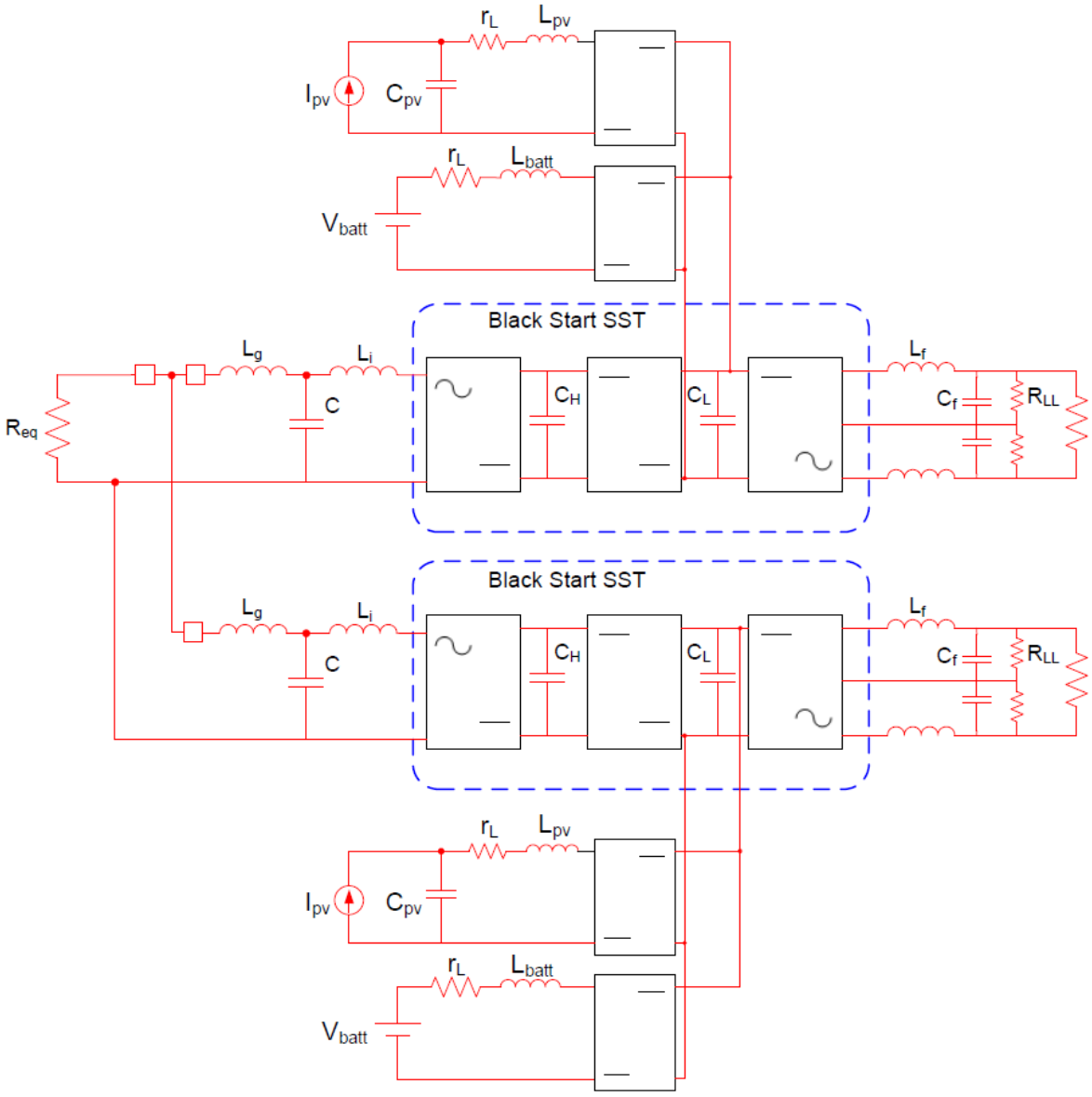

Figure 4.28: Black start operation of solid state transformer

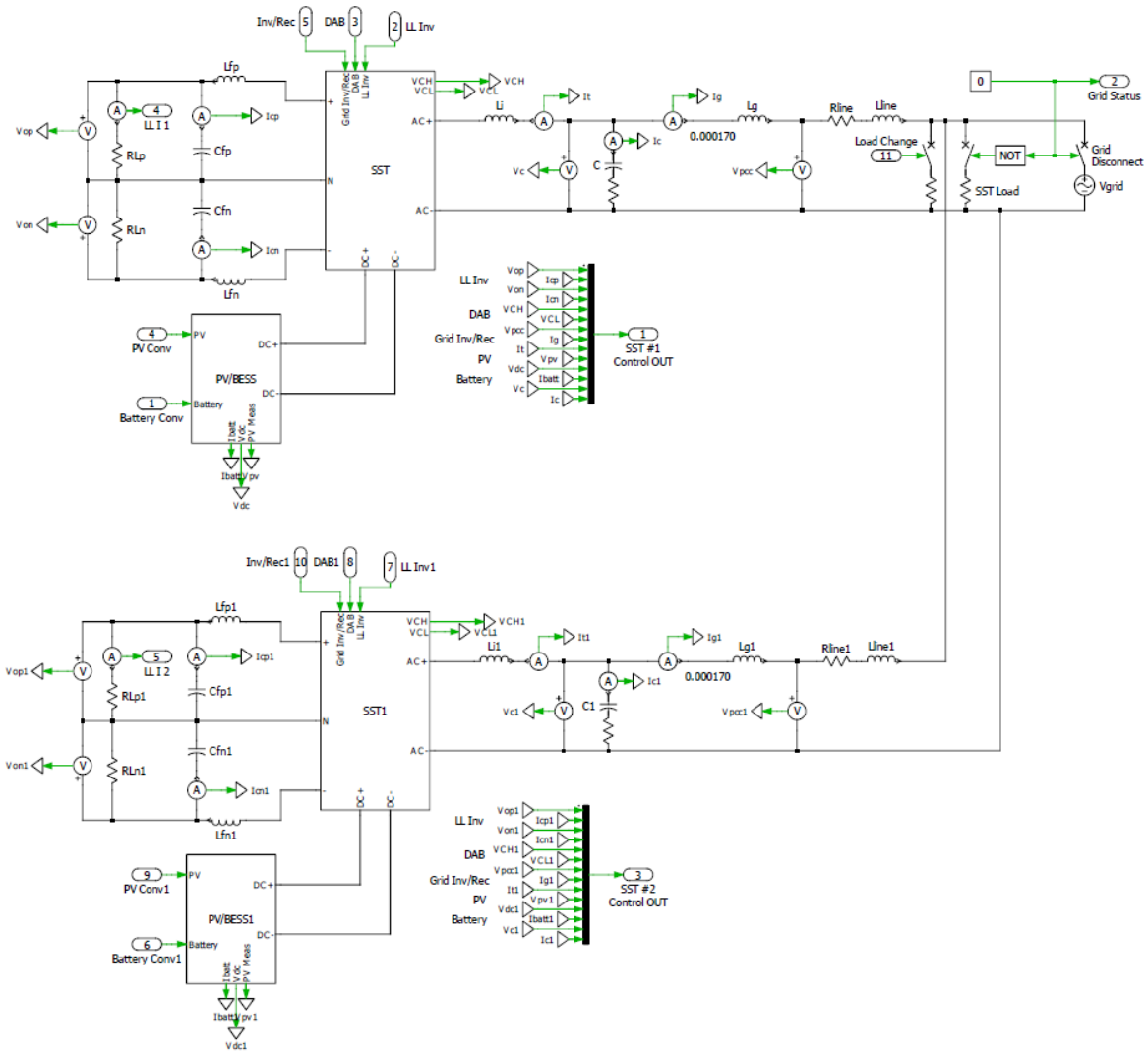

Figure 4.29: Black start operation of solid state transformer - simulation circuit

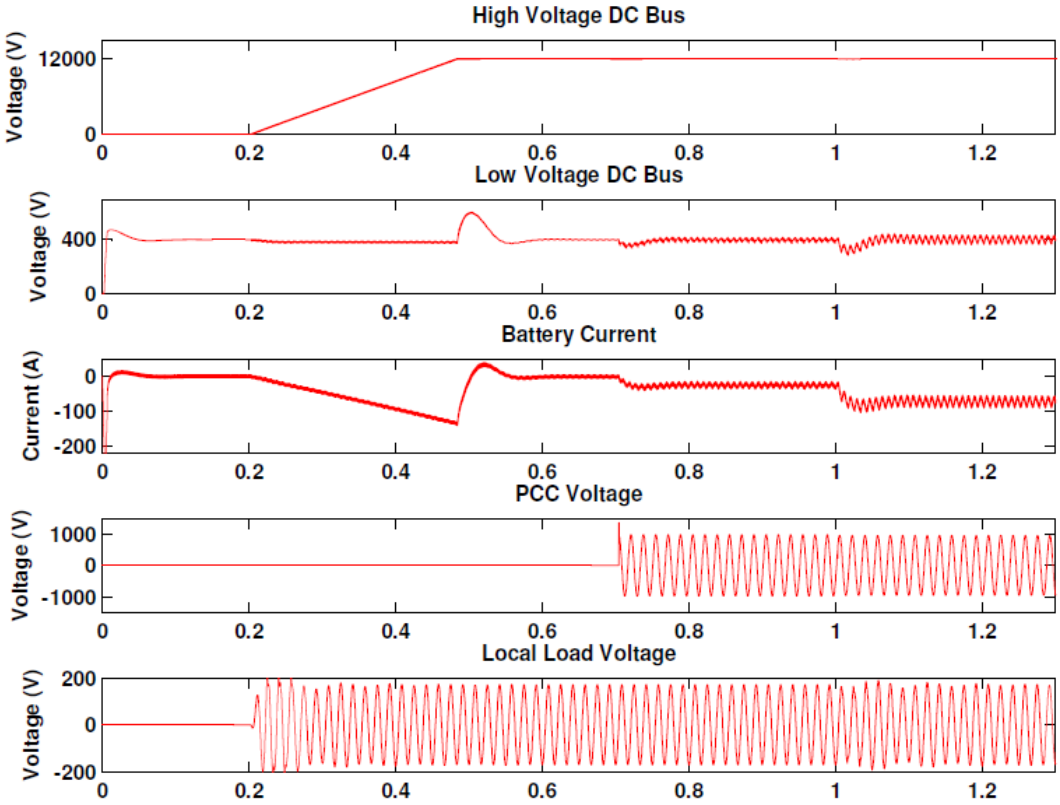

Figure 4.30: Black start solid state transformer waveforms

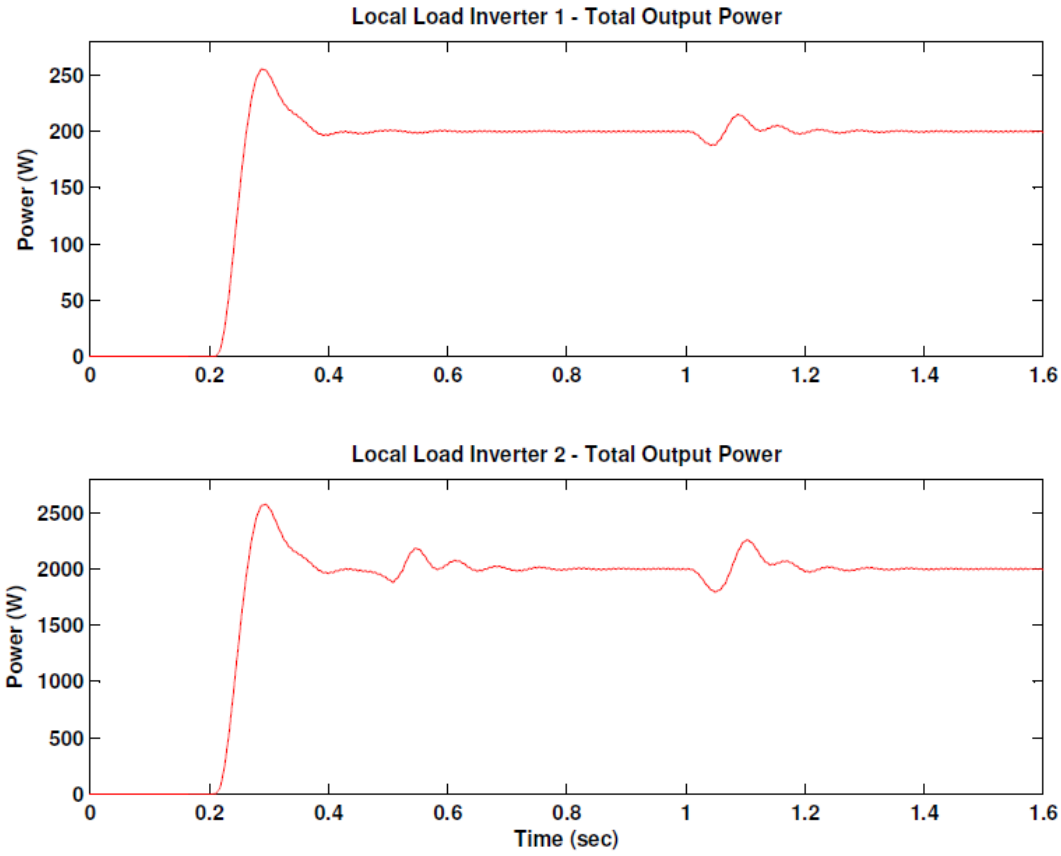

Figure 4.31: Local load inverter output power

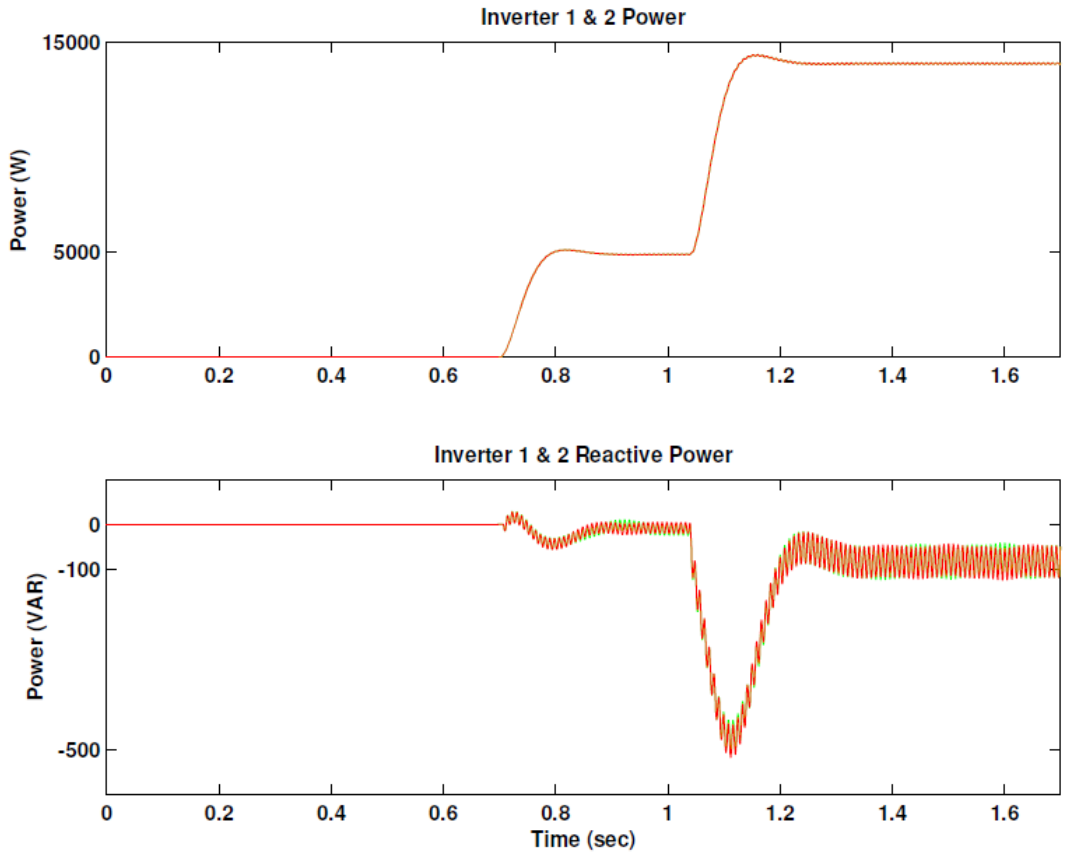

Figure 4.32: Real and reactive load power sharing of parallel solid state transformers - R Load

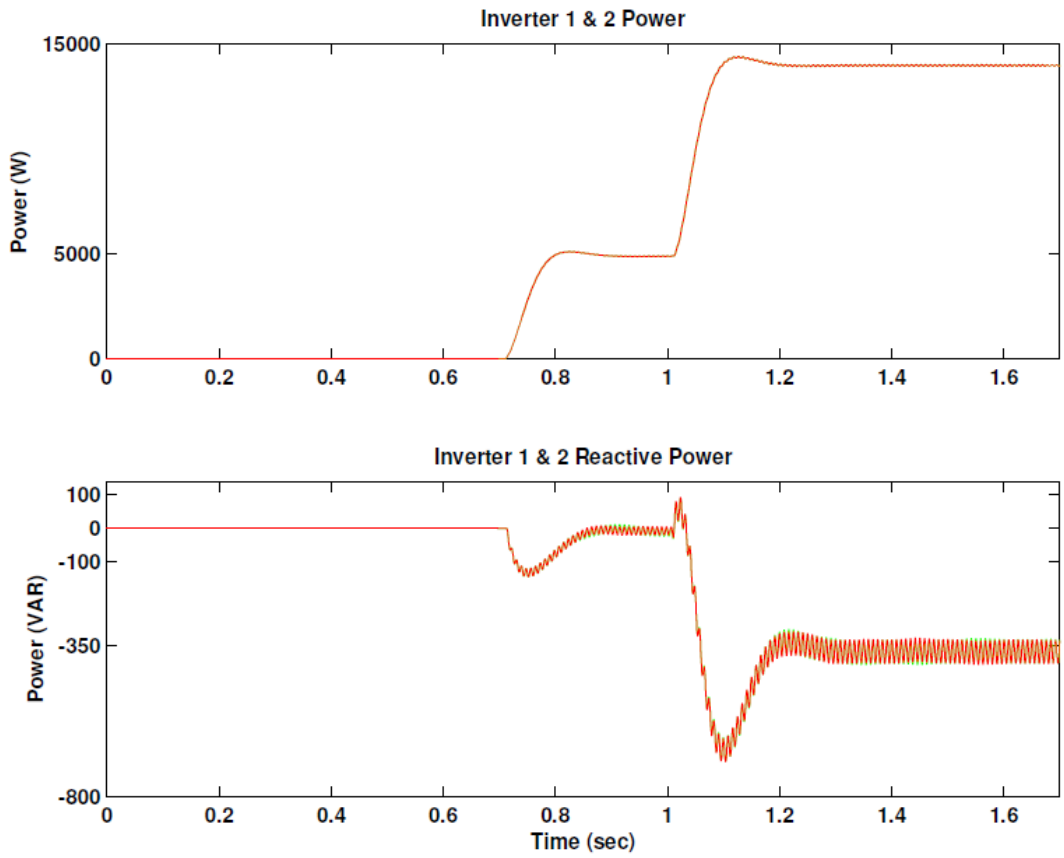

Figure 4.33: Real and reactive load power sharing of parallel solid state transformers - RL Load

Figure 4.30 shows the black start operation of the solid state transformers, the plots are the same for both solid state transformers in the system. At 0.2 seconds the local load inverter supplies the load and the dual active bridge regulates the high voltage DC bus to 12 kV at 0.5 seconds, the battery converter causes an overshoot on the DC bus because of the large current being supplied and the time required for the converter to regulate the output current to the load level of current. At 0.7 seconds the solid state transformers operate in parallel and restore the grid voltage and supply a load of 10 kW. At 1 second the load increases to 30 kW.

Figure 4.31 shows the power delivered to the local load of each solid state transformer. The two solid state transformers have different loads attached, the affect of the battery converter low voltage DC bus overshoot after the high voltage DC bus is charged appears at 0.5 seconds, additionally the load change at 1 second causes a transient on the load power.

Figure 4.32 shows the output real and reactive power of each inverter. The real power is shared very well, at 0.7 seconds the 10 kW load is connected, at 1 second the load is increased.

The reactive power is shared well between the solid state transformers, some small deviations between the outputs can be observed.

Figure 4.33 shows an RL load change, compared with the R load change we can see a much larger increase in reactive power being shared by the solid state transformers.

Reduction of DC Bus Overshoot from Battery Converter

As was previously seen, the battery converter causes an overshoot on the low voltage DC bus when the high voltage DC capacitor reaches its nominal value of 12 kV. This is caused by the large current injected into the low voltage DC bus by the battery converter to charge the high voltage DC bus. Once the high voltage DC bus is charged and the solid state transformers parallel to supply the load the battery converter starts to regulate the battery current to the load level, while the converter is still injecting this large current into the low voltage DC bus, the voltage overshoots and causes power fluctuations on the local load.

To solve the low voltage DC bus overshoot, the reference voltage of the high voltage DC bus capacitor is ramped up to the nominal 12 kV value such that the charging current from the battery to the low voltage DC bus capacitor is more constant and a smaller value. Also, the parallel inverter stages are commanded to turn on slightly before the high voltage DC bus capacitor reaches nominal value at 9 kV in order to reduce the battery current transient.

Figure 4.34 shows the high voltage DC bus capacitor charge ramping up, the inverters are paralleled to supply load at 2.3 seconds and the battery current increases, at 2.9 seconds the high voltage DC bus capacitor reaches 12 kV and the battery current is reduced slightly. The large overshoot previously seen is now eliminated.

Figure 4.35 shows the local load inverter output load power while Figure 4.36 shows the real and reactive power sharing of the parallel solid state transformers supplying load.

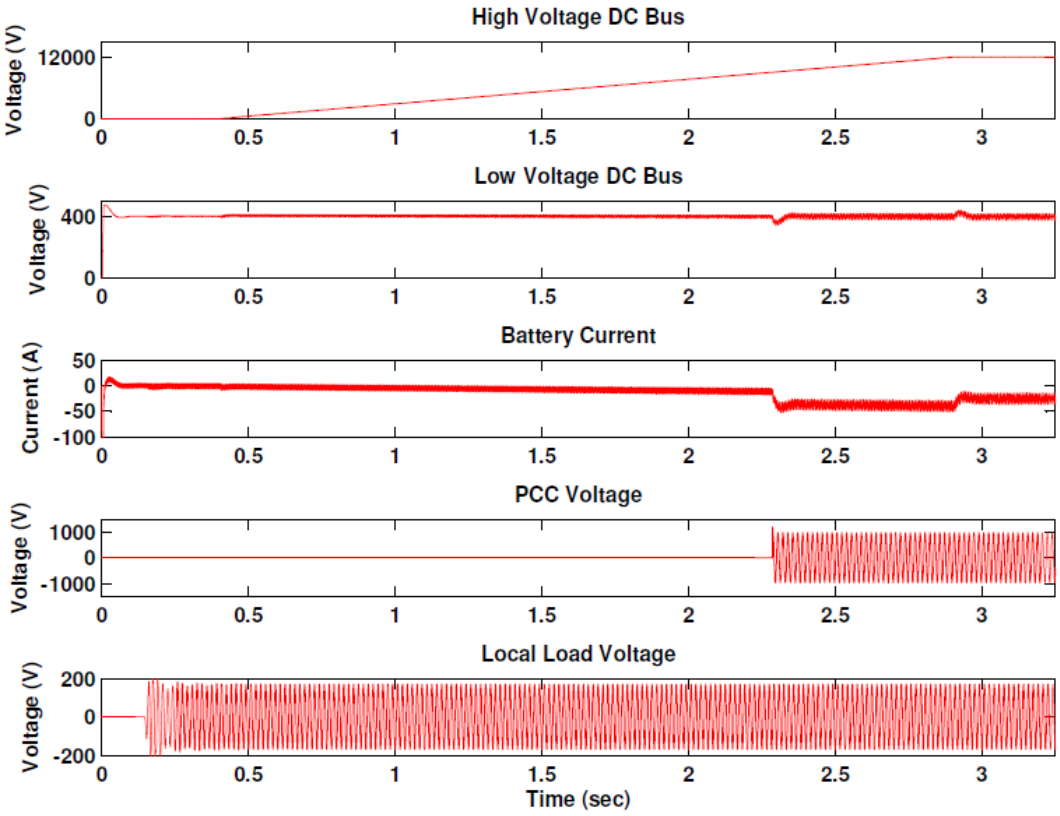

Figure 4.34: Low voltage DC bus overshoot eliminated

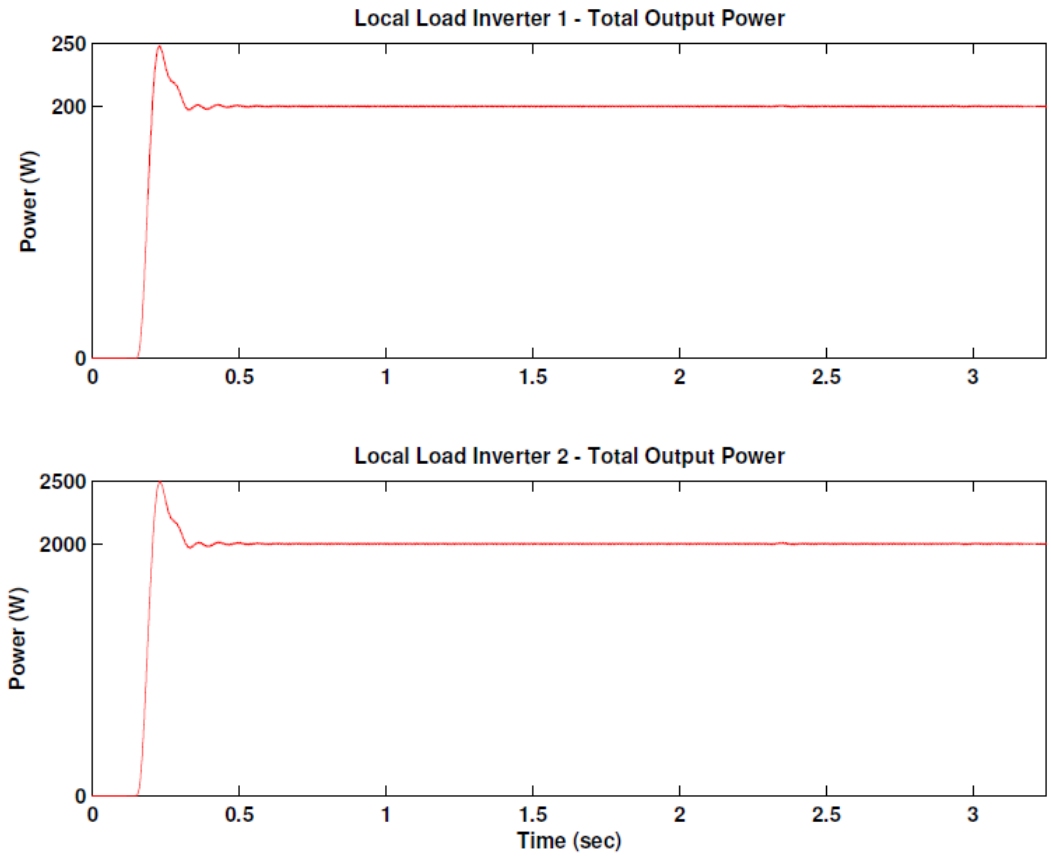

Figure 4.35: Local load inverter output power

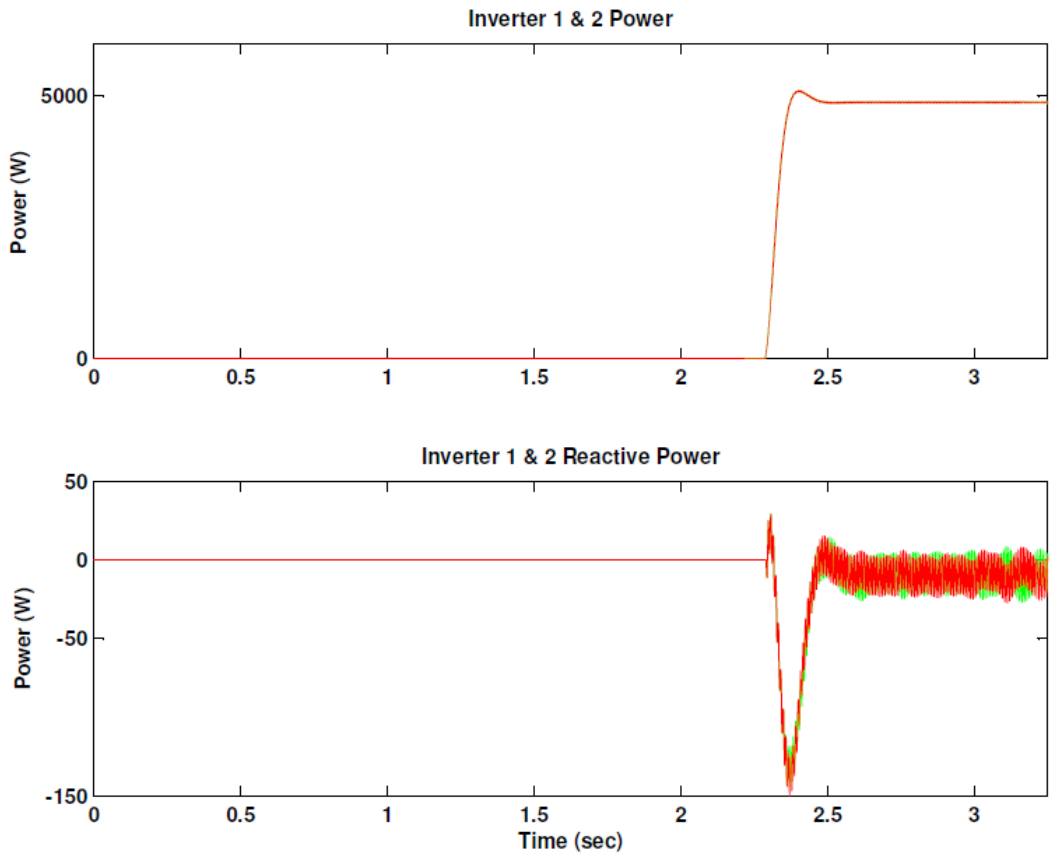

Figure 4.36: Real and reactive load power sharing

4.2.3 Reconnecting Solid State Transformer to Grid

The grid voltage will eventually return after the outage, this requires that the solid state transformer reconnect to the grid to return to normal operating conditions. The procedure designed relies on the grid intelligence and communication as shown in Figure 4.37 to determine that the grid has been restored such that the solid state transformers can take appropriate action. Upon grid restoration the solid state transformers should shut down the parallel inverter stages and dual active bridge stages, the local load inverter can continue to supply the local load. Next the grid can be reconnected through a transfer switch, with the grid voltage reference available the rectifier stages of each solid state transformer can synchronize to this grid reference and reconnect in order to control the high voltage DC bus. Next the dual active bridge can start in order to control the low voltage DC bus while the battery converter must switch to current control mode to recharge the battery bank.

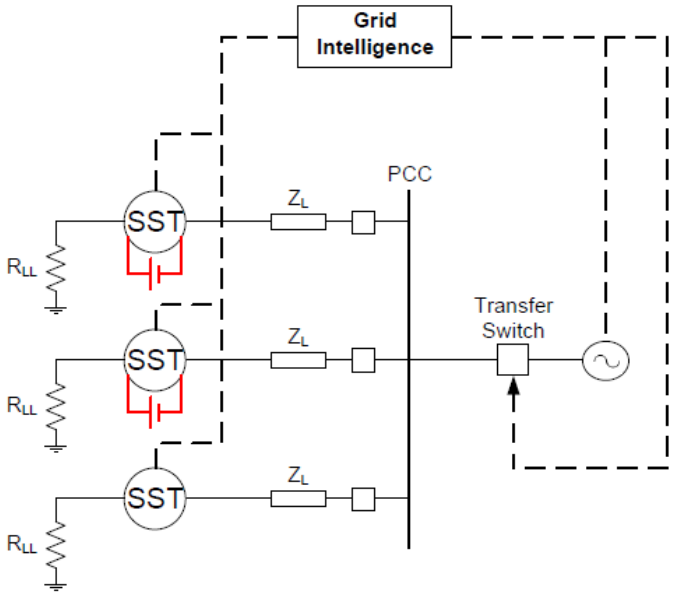

Figure 4.37: Reconnecting the grid

Figure 4.38 shows the operation of the solid state transformer during black start and reconnecting to the grid. The simulation starts in black start mode with the parallel solid state transformers supplying load, the same as the previous simulation. The high voltage bus is 12 kV, low voltage bus is 400 V and is regulated by the battery converter, the local load inverter is supplying its load as shown in Figure 4.39. At 0.5 seconds the grid is determined to be restored and the parallel inverter and dual active bridge stages shut down, there is a slight rise on the DC bus but is regulated back by the battery converter. It can be seen that the battery current decreases also at this time because the battery is now only supplying the local load. After shutting down the dual active bridges and parallel inverters, the grid voltage is restored through the transfer switch at approximately 0.58 seconds. The rectifier synchronizes with the grid voltage and reconnects after several cycles at approximately 0.67 seconds and a slight transient can be seen on the high voltage DC bus. Next, at approximately 0.95 seconds the dual active bridge starts regulating the low voltage DC bus to 400 V as the battery converter switches to current control mode and starts recharging the batteries. At this point the grid is now supplying the local load and the solid state transformer has returned to normal operation. At approximately 1.66 seconds the battery current reduces to 0 A once the batteries are fully charged. The local load is never disconnected during the reconnection procedure.

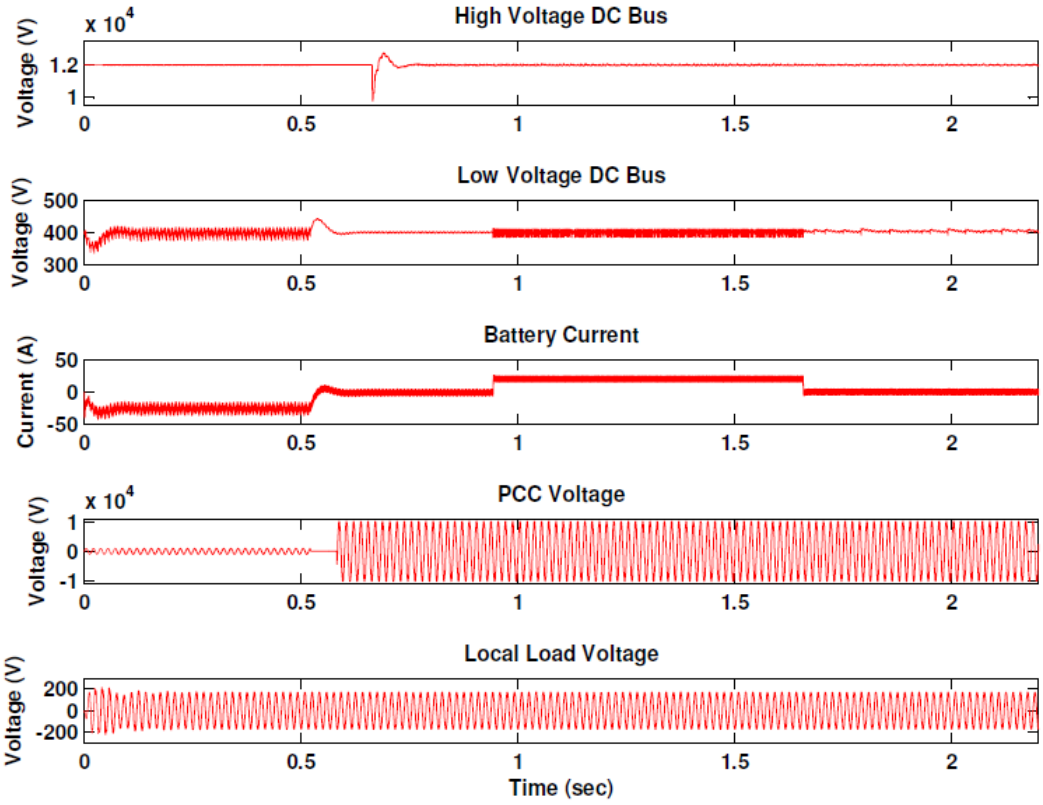

Figure 4.38: Solid state transformer reconnecting to the grid

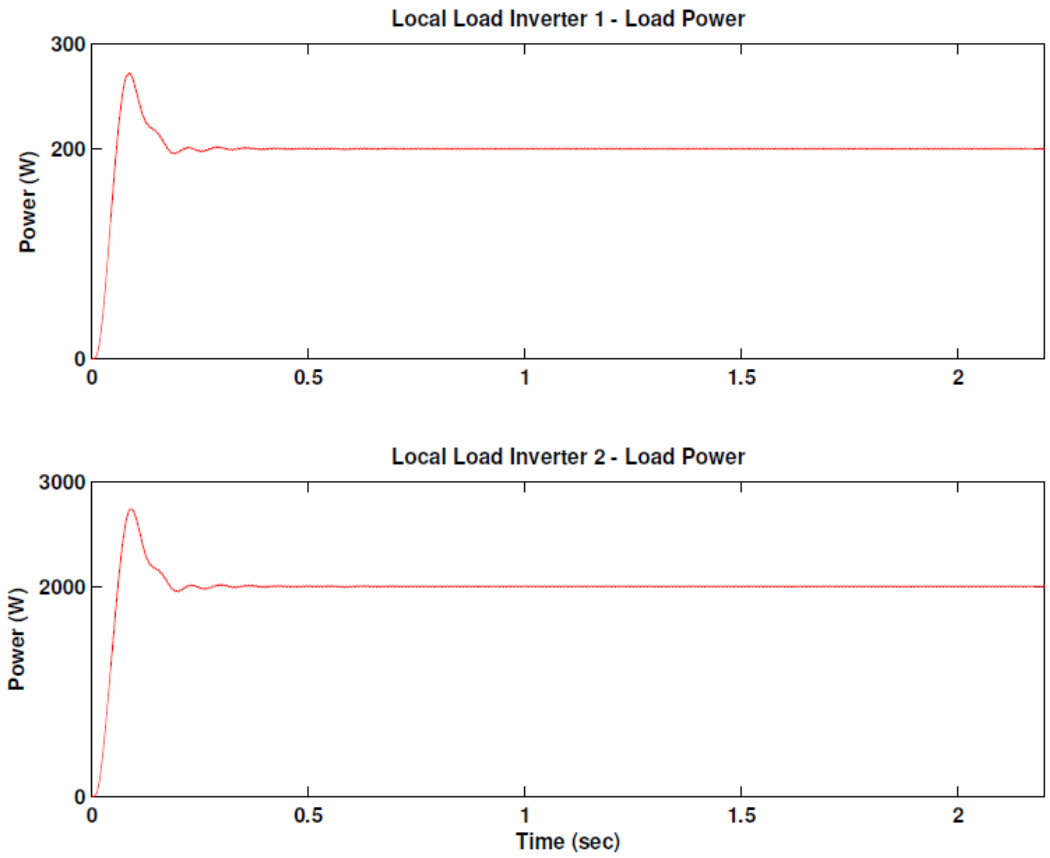

Figure 4.39: Local load inverter power during reconnection procedure

4.2.4 Solid State Transformer and Inverter Black Start Comparison

A comparison can be made between the solid state transformer black start operation and the black start operation using the traditional inverter topology. A comparison is shown in Figure 4.40, the left side shows the solid state transformer topology and the right shows a typical inverter topology. A few interesting comparisons can be made between the two.

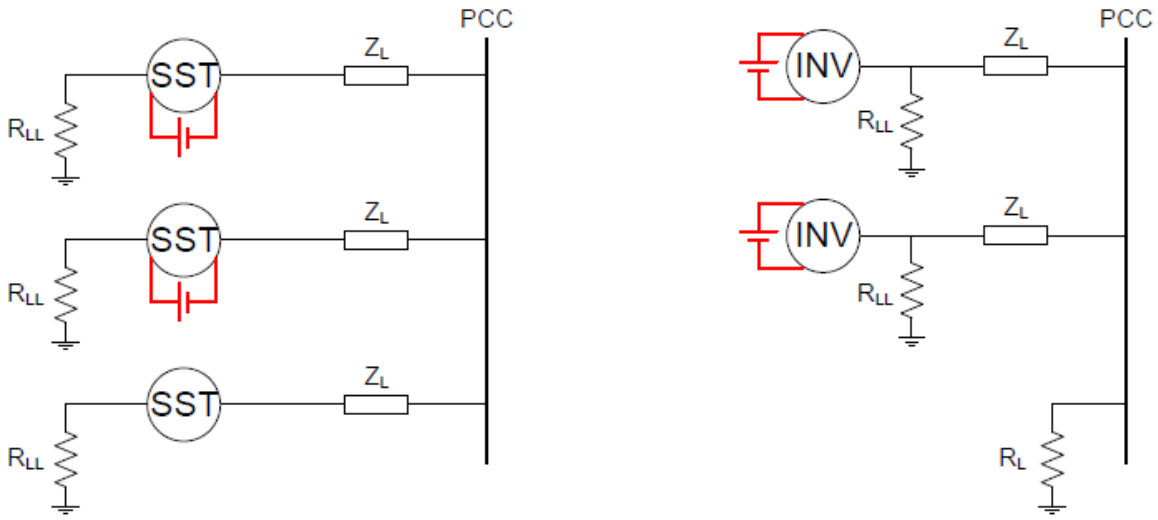

Figure 4.40: Solid state transformer black start and traditional inverter black start

Firstly the solid state transformer topology can use a simpler method of control when reconnecting to the grid after the black start operation. The inverter requires a synchronization control loop when transitioning back to grid connected mode [40], the solid state transformer can continue to supply load from the low voltage DC bus through the battery bank/PV array while the grid tied rectifier synchronizes with the grid as it is already designed to do. Once the synchronization is complete the dual active bridge can begin regulating the low voltage DC bus while the battery bank DC/DC converter changes to current control for charging the batteries.

Another benefit of using the solid state transformer is that it is less sensitive to the droop imposed on the voltage and frequency through the droop control loop (including the voltage drop created by the virtual impedance loop) which is necessary for both the solid state transformer topology and the inverter topology to accurately share the real and reactive load power requirements between each other. It can be seen that all loads are regulated by the solid state transformer local load inverter which can regulate its load to the correct voltage even with small voltage drops on the input caused by the droop control. For the inverter topology, an amplitude restoration loop [40] in the controller is used to restore the load voltage and frequency to the nominal values, this further increases the complexity of the controller.

Another benefit of the solid state transformer topology is there is no disturbance in the reactive power sharing due to the local load whereas the inverter topology's local load can create an offset causing a mismatch in the reactive power sharing and possibly causing a possible condition of operating the inverters beyond their maximum rating [39].

Chapter 5

Conclusion and Future Work

5.1 Conclusion

This thesis has proposed a novel converter topology for the solid state transformer along with the control design that can be used for normal and emergency power supply, specifically in the black start mode of operation. The solid state transformer has been shown to be a viable resource for reducing the length of costly power outages, providing greater functionality and control than the traditional iron core transformers. The solid state transformer also benefits from a more simple control system when supplying power in black start operation with a local load as compared to using only a grid connected inverter.

5.2 Future Work

The model presented can be improved upon in several different ways including:

1. Develop battery model for use in the system simulations showing state of charge (SOC) and other nominal battery quantities
2. Implement the BMS (battery management system) to regulate battery charging current in normal operation
3. Incorporate PV model with maximum power point tracking algorithm
4. Optimize PV array and battery bank sizing
5. Optimize converters to further improve steady state and transient responses during grid connected and black start operations

6. Determine load shedding procedure for the condition of excess load on the solid state transformers

Additionally, while implementing the proposed design in hardware is necessary it would be a large project to undertake, however building a scaled down hardware model would suffice which would consist of two solid state transformers and load.

REFERENCES

[1] Kristina Hamachi LaCommare and Joseph H. Eto. Understanding the cost of power interruptions to U.S. electricity consumers. *Berkeley National Laboratory*, sep. 2004.

[2] US Department of Energy. The potential benefits of distributed generation and rate-related issues that may impede their expansion. 2007.

[3] NERC standard eop-005-1 system restoration plans.

[4] J.W. Feltes and C. Grande-Moran. Black start studies for system restoration. In *Power and Energy Society General Meeting - Conversion and Delivery of Electrical Energy in the 21st Century, 2008 IEEE*, pages 1 –8, july 2008.

[5] Energy efficieny standards. http://ees.ead.lbl.gov/projects/current_projects/distribution_transformers.

[6] W. McMurray. Power converter circuits having a high-frequency link. *US Patent 3517300*, 1970.

[7] Tiefu Zhao. *Design and Control of a Cascaded H-Bridge Converter based Solid State Transformer (SST)*. PhD thesis, North Carolina State University, 2010.

[8] J. L. Brooks. Solid state transformer concept development. Naval Material Command. Port Hueneme, Civil Engineering Lab. Naval Construction Battalion Center, 1980.

[9] Proof of the principle of the solid-state transformer and the ac/ac switchmode regulator. San Jose State Univ., San Jose, CA EPRI TR-105 067, 1995.

[10] IEEE 1547 standard for interconnecting distributed resources with electric power systems. WEBSITE HERE.

[11] William P. Robbins Ned Mohan, Tore M. Undeland. *Power Electronics: Converters, Applications, and Design*. Wiley, 2002.

[12] Thomas A. Lipo D. Grahame Holmes. *Pulse Width Modulation for Power Converters: Principles and Practice*. Wiley-IEEE Press, 2003.

[13] Zhihong Ye, D. Boroyevich, Jae-Young Choi, and F.C. Lee. Control of circulating current in two parallel three-phase boost rectifiers. *Power Electronics, IEEE Transactions on*, 17(5):609 – 615, sep 2002.

[14] Kun Xing. *Modeling, Analysis and Design of Distributed Power Electronics System Based on Building Block Concept*. PhD thesis, Virginia Polytechnic Institute and State University, 1999.

[15] Reza Iravani Amirnaser Yazdani. *Voltage-Sourced Converters in Power Systems Modeling, Control, and Applications*. Wiley, 2002.

[16] Mustansir H. Kheraluwala. *High-Power High-Frequency DC-To-DC Converters.* PhD thesis, University of Wisconsin - Madison, 1991.

[17] Georgios D. Demetriades. *On Small-Signal Analysis and Control of the Single and the Dual-Active Bridge Topologies.* PhD thesis, Royal Institute of Technology, 2005.

[18] H.K. Krishnamurthy and R. Ayyanar. Building block converter module for universal (ac-dc, dc-ac, dc-dc) fully modular power conversion architecture. In *Power Electronics Specialists Conference, 2007. PESC 2007. IEEE*, pages 483 –489, june 2007.

[19] K.H. Ahmed, S.J. Finney, and B.W. Williams. Passive filter design for three-phase inverter interfacing in distributed generation. In *Compatibility in Power Electronics, 2007. CPE '07*, pages 1 –9, 29 2007-june 1 2007.

[20] M. Liserre, F. Blaabjerg, and S. Hansen. Design and control of an lcl-filter-based three-phase active rectifier. *Industry Applications, IEEE Transactions on*, 41(5):1281 – 1291, sept.-oct. 2005.

[21] Anca Julean. Active damping of lcl filter resonance in grid connected applications. Master's thesis, Aalborg University, 2009.

[22] P. Channegowda and V. John. Filter optimization for grid interactive voltage source inverters. *Industrial Electronics, IEEE Transactions on*, 57(12):4106 –4114, dec. 2010.

[23] M. Liserre, A. Dell'Aquila, and F. Blaabjerg. Genetic algorithm-based design of the active damping for an lcl-filter three-phase active rectifier. *Power Electronics, IEEE Transactions on*, 19(1):76 – 86, jan. 2004.

[24] W. Gullvik, L. Norum, and R. Nilsen. Active damping of resonance oscillations in lcl-filters based on virtual flux and virtual resistor. In *Power Electronics and Applications, 2007 European Conference on*, pages 1 –10, sept. 2007.

[25] C. Wessels, J. Dannehl, and F.W. Fuchs. Active damping of lcl-filter resonance based on virtual resistor for pwm rectifiers; stability analysis with different filter parameters. In *Power Electronics Specialists Conference, 2008. PESC 2008. IEEE*, pages 3532 –3538, june 2008.

[26] R. Zhang, M. Cardinal, P. Szczesny, and M. Dame. A grid simulator with control of single-phase power converters in d-q rotating frame. In *Power Electronics Specialists Conference, 2002. pesc 02. 2002 IEEE 33rd Annual*, volume 3, pages 1431 – 1436 vol.3, 2002.

[27] E. Twining and D.G. Holmes. Grid current regulation of a three-phase voltage source inverter with an lcl input filter. In *Power Electronics Specialists Conference, 2002. pesc 02. 2002 IEEE 33rd Annual*, volume 3, pages 1189 – 1194 vol.3, 2002.

[28] Junhong Zhang. *Bidirectional DC-DC Power Converter Design Optimization, Modeling and Control.* PhD thesis, Virginia Polytechnic Institute and State University, 2008.

[29] A. Yazdani and P.P. Dash. A control methodology and characterization of dynamics for a photovoltaic (pv) system interfaced with a distribution network. *Power Delivery, IEEE Transactions on*, 24(3):1538 –1551, july 2009.

[30] H. Karimi-Davijani and O. Ojo. Modeling and steady-state analysis of a stand-alone, photo-voltaic-three phase inverter power system. In *Applied Power Electronics Conference and Exposition (APEC), 2011 Twenty-Sixth Annual IEEE*, pages 1259 –1266, march 2011.

[31] D.N. Zmood and D.G. Holmes. Stationary frame current regulation of pwm inverters with zero steady-state error. *Power Electronics, IEEE Transactions on*, 18(3):814 – 822, may 2003.

[32] D.N. Zmood and D.G. Holmes. Improved voltage regulation for current-source inverters. *Industry Applications, IEEE Transactions on*, 37(4):1028 –1036, jul/aug 2001.

[33] J.W. Feltes and C. Grande-Moran. Black start studies for system restoration. In *Power and Energy Society General Meeting - Conversion and Delivery of Electrical Energy in the 21st Century, 2008 IEEE*, pages 1 –8, july 2008.

[34] J.A.P. Lopes, C.L. Moreira, A.G. Madureira, F.O. Resende, X. Wu, N. Jayawarna, Y. Zhang, N. Jenkins, F. Kanellos, and N. Hatziargyriou. Control strategies for microgrids emergency operation. In *Future Power Systems, 2005 International Conference on*, pages 6 pp. –6, nov. 2005.

[35] C. L. Moreira, F. O. Resende, and J. A. P. Lopes. Using low voltage microgrids for service restoration. *Power Systems, IEEE Transactions on*, 22(1):395 –403, feb. 2007.

[36] Bruce F. Wollenberg Allen J. Wood. *Power Generation Operation and Control*. Wiley-Interscience, 1996.

[37] J.C. Vasquez, J.M. Guerrero, A. Luna, P. Rodriguez, and R. Teodorescu. Adaptive droop control applied to voltage-source inverters operating in grid-connected and islanded modes. *Industrial Electronics, IEEE Transactions on*, 56(10):4088 –4096, oct. 2009.

[38] S. Golestan, M. Joorabian, H. Rastegar, A. Roshan, and J.M. Guerrero. Droop based control of parallel-connected single-phase inverters in d-q rotating frame. In *Industrial Technology, 2009. ICIT 2009. IEEE International Conference on*, pages 1 –6, feb. 2009.

[39] Yun Wei Li and Ching-Nan Kao. An accurate power control strategy for power-electronics-interfaced distributed generation units operating in a low-voltage multibus microgrid. *Power Electronics, IEEE Transactions on*, 24(12):2977 –2988, dec. 2009.

[40] J.C. Vasquez, J.M. Guerrero, M. Savaghebi, and R. Teodorescu. Modeling, analysis, and design of stationary reference frame droop controlled parallel three-phase voltage source inverters. In *Power Electronics and ECCE Asia (ICPE ECCE), 2011 IEEE 8th International Conference on*, pages 272 –279, 30 2011-june 3 2011.

[41] N. Fermia, D. Granozio, G. Petrone, and M. Vitelli. Predictive adaptive mppt perturb and observe method. *Aerospace and Electronic Systems, IEEE Transactions on*, 43(3):934 –950, july 2007.

[42] Jung-Min Kwon, Bong-Hwan Kwon, and Kwang-Hee Nam. Three-phase photovoltaic system with three-level boosting mppt control. *Power Electronics, IEEE Transactions on*, 23(5):2319 –2327, sept. 2008.

[43] Fangrui Liu, Shanxu Duan, Fei Liu, Bangyin Liu, and Yong Kang. A variable step size inc mppt method for pv systems. *Industrial Electronics, IEEE Transactions on*, 55(7):2622 –2628, july 2008.